Molecular Dynamics Simulations of Aqueous Trimethylamine *N*-oxide Solution and Room Temperature Ionic Liquids to Reveal Their Microscopic Dynamics

Max Planck Graduate Center
mit der Johannes Gutenberg-Universität

Dissertation

zur Erlangung des Grades eines
"Doktor rerum naturalium (Dr. rer. nat.)"
der Fachbereiche:
08 – Physik, Mathematik und Informatik
09 – Chemie, Pharmazie und Geowissenschaften
10 – Biologie und
Unimedizin
der Johannes Gutenberg-Universität Mainz

Kota Usui

Mainz, 24.07.2017

Tag der mündlichen Prüfung: 05.09.2017

Erstgutachter:

Zweitgutachter:

Declaration

I hereby declare that I wrote the dissertation submitted without any unauthorized external assistance and used only sources acknowledged in the work. All textual passages which are appropriated verbatim or paraphrased from published and unpublished texts as well as all information obtained from oral sources are duly indicated and listed in accordance with bibliographical rules. In carrying out this research, I complied with the rules of standard scientific practice as formulated in the statutes of Johannes Gutenberg-University Mainz to insure standard scientific practice.

Publications covered in this thesis

K. Usui, J. Hunger, M. Sulpizi, T. Ohto, M. Bonn, and Y. Nagata, "*Ab Initio* Liquid Water Dynamics in Aqueous TMAO Solution", *J. Phys. Chem. B*, **2015**, *119*, 10597–10606.

K. Usui, Y. Nagata, J. Hunger, M. Bonn, and M. Sulpizi, "A new force field including charge directionality for TMAO in aqueous solution", *J. Chem. Phys.*, **2016**, 145, 064103.

K. Usui, J. Hunger, M. Bonn, and M. Sulpizi, "Dynamical heterogeneities of Rotational Motion in Room Temperature Ionic Liquids Evidenced by Molecular Dynamics Simulations", *submitted.*

Other publications by the same author

Y. Nagata, T. Hasegawa, E. H. G. Backus, K. Usui, S. Yoshimune, T. Ohto, and M. Bonn, "The surface roughness, but not the water molecular orientation varies with temperature at the water-air interface", *Phys. Chem. Chem. Phys.*, **2015**, *17*, 23559-23564.

T. Ohto, K. Usui, T. Hasegawa, M. Bonn, and Y. Nagata, "Toward *ab initio* molecular dynamics modeling for sum-frequency generation spectra; an efficient algorithm based on surface-specific velocity-velocity correlation function", *J. Chem. Phys.*, **2015**, *143*, 124702.

Y. Nagata, K. Usui, and M. Bonn, "Molecular Mechanism of Water Evaporation", *Phys. Rev. Lett.*, **2015**, *115*, 236102

R. Randey, K. Usui, R. A. Livingstone, S. A. Fischer, J. Pfaendtner, E. H. G. Backus, and Y. Nagata, J. Fröhlich-Nowoisky, L. Schmüser, S. Mauri, J. F. Scheel, D. A. Knopf, U. Pöschl, M. Bonn, T. Weidner, "Ice-nucleating bacteria control the order and dynamics of interfacial water", *Sci. Adv.*, **2016**, *2*, e1501630.

Table of Contents

Summary

In this thesis I investigated, using molecular dynamics simulations, the structure and dynamics of complex molecular systems, where strong, specific intermolecular interactions are responsible for structural and dynamical heterogeneity. The aim of my work was twofold. On one side, it was to unravel the molecular mechanism behind experimental observations, in particular time resolved vibrational spectroscopy, and on the other side, it was to develop new, accurate force fields capable of extending the power of atomistic simulations to larger size systems and longer time scales.

I specifically investigated two systems: trimethylamine *N*-oxide (TMAO) and a series of alkylammonium nitrates, room temperature ionic liquids (RTILs).

TMAO is a biomolecule known as osmolyte and chemical chaperone. These functions are supposed to stem from the strong intermolecular interaction between TMAO and water, via the hydrophilic oxygen (O_{TMAO}) atom of TMAO. To reveal those mechanisms, the dynamics of water molecules around TMAO has been experimentally investigated, though the extent and molecular origin of the experimentally observed slowdown remained unclear. I performed *ab initio* MD (AIMD) simulations to understand the effect of TMAO on the rotational dynamics of water molecules. My simulations revealed that the water rotation is strongly slowed down near the hydrophilic O_{TMAO} atom, due to a long-lived and highly-directional hydrogen bond between TMAO and water. As a further step, I also developed a new force field for TMAO, which captures the directionality of the TMAO-water hydrogen bonds, providing a better description of water structure and dynamics and structure around the O_{TMAO} atom, which closely resembles the AIMD simulations results. The new force field will permit to investigate larger scale TMAO solutions, also including proteins, capturing the local water dynamics.

In the second part of my thesis I investigated, using molecular dynamics simulations, the dynamics of a series of RTILs (specifically a series of alkylammonium nitrates), which are promising new green solvents. I revealed that the dynamics of the constituent ions is heterogeneous in two different aspects. Specifically, the rotational dynamics of the two ends of cationic chains differ, as a result of the asymmetry of the charge distribution on the cations. Additionally, the rotational dynamics of the charged group of cations (N_{head}-H groups) has a broad distribution, which originates from the different local inter-ionic environment.

Zusammenfassung

In meiner Doktorarbeit untersuchte ich mittels Molekulardynamik Simulationen die Struktur und Dynamik von komplexen Systemen, bei denen starke spezifische intermolekulare Wechselwirkungen zu struktureller und dynamische Heterogenität führen. Das Ziel war es hierbei sowohl die molekularen Wirkungsmechanismen von experimentelle Beobachtungen, welche hauptsächlich auf zeitaufgelöster Schwingungsspektroskopie basieren, zu ergründenden als auch neue und genauere Kraftfelder zu entwickeln um große Systeme mit atomistischen Simulationen über längere Zeit zu untersuchen.

Im Speziellen untersuchte ich zwei Systeme: Trimethylamin-N-oxid (TMAO) und eine Reihe von Alkylammonium Nitraten (ionische Flüssigkeiten).

TMAO ist ein Molekül das in der Biologie sowohl als Osmolyt als auch als Begleitmolekül auftritt. Es wird vermutet, dass diese Funktionen eng mit der Fähigkeit des hydrophilen Sauerstoffs (O_{TMAO}) starke Wechselwirkungen mit Wasser einzugehen verknüpft ist. Experimentell spiegeln sich diese starken Wechselwirkungen in einer Verlangsamung der Wasserdynamik wider, wobei die molekularen Ursachen hierfür ungeklärt blieben. Um diese molekularen Ursachen zu ergründen habe ich *ab initio* Molekulardynamik Simulationen (AIMD) durchgeführt. Diese Simulationen zeigten, dass sich die Rotationsdynamik von Wasser in der Nähe des hydrophilen O_{TMAO} Atoms durch die Ausbildung sehr langlebiger und stark gerichteter Wasserstoffbrückenbindungen extrem verlangsamt. Auf Basis dieser Beobachtungen habe ich ein neues Kraftfeld für TMAO entwickelt, welches die Struktur und Dynamik von Wasser um TMAO besser beschreibt und die AIMD Ergebnisse reproduzieren kann. Dieses neue Kraftfeld ermöglicht es die (Wasser-)Dynamik komplexerer Systeme, wie zum Beispiel Proteine in wässriger TMAO Lösung zu untersuchen.

Im zweiten Teil meiner Arbeit untersuchte ich die molekulare Dynamik einer Reihe von flüssigen Salzen (Alkylammonium Nitrat ionische Flüssigkeiten), welche vielversprechende Kandidaten für alternative umweltfreundliche Lösungsmittel sind. Hierbei zeigte ich, dass die Dynamik der Ionen hinsichtlich zweierlei Gesichtspunkten heterogen ist: Die die Rotationsdynamik der zwei Enden der Kationen unterscheidet sich stark, was sich auf die asymmetrische Ladungsverteilung innerhalb der Kationen zurückführen lässt. Zusätzlich zeigt die Dynamik der geladenen Kopfgruppe eine breite Verteilung, welche auf sehr verschiedenen ionischen Umgebungen basiert.

Chapter 1
Introduction

1.1 Molecular dynamics simulations

Molecular dynamics (MD) simulations are simulation methods to obtain the temporal evolution of particles. Objects in MD simulations are sometimes termed “molecules”, even if they are atoms or ions in the context of chemistry, which is why this simulation technique is called “molecular” dynamics simulations. By solving Newton’s equations of motion for the particles, MD simulations provide the trajectories of the particles. MD simulations have been a powerful tool to obtain the microscopic or atomistic picture of systems, which is often buried by experiment or analytical calculations due to different kinds of averaging of given quantities, such as time average or average over different molecules.

The first paper using MD simulations was published in 1957 by Alder and Wainwright and described the phase transition in a hard sphere system.[1] After that, following the development of computer, the area where MD simulations can be applied has broadened.[2] One of the fields where MD simulations are powerfully employed is biochemistry. Researchers have used MD simulations to gain insight into microscopic behaviors in biological processes. For example, Karplus and co-workers performed MD simulations of proteins in 1977, to investigate the dynamics of folded proteins. Karplus was later awarded Nobel Prize in Chemistry in 2013 with Levitt and Warshel, for "the development of multiscale models for complex chemical systems". As another example, chemical reactions were also investigated using MD simulations by Hynes and co-workers in 1987, involving a S_N2 reaction in water.[3] These days a lot of research rely on MD simulations to give atomistic rationales to experimentally observed phenomena[4–7] and MD simulations are been even employed to design new drugs[8] or develop new materials,[9] which promises to make their industrial productions more efficient.

My PhD research uses MD simulations to investigate the microscopic behavior of two types of systems: aqueous trimethylamine *N*-oxide (TMAO) solution and room temperature ionic liquids (RTILs). Both systems are characterized by strong intermolecular interactions among constituent molecules. In the first case, TMAO has a hydrophilic oxygen atom, which

forms “strong” hydrogen bonds with water molecules. In the second case, RTILs consist of liquid ions, which have strong Coulombic interaction among them. Our simulated data are compared to experimental data obtained by vibrational spectroscopy, with the aim to provide a microscopic picture for the experimental data. The comparison to the experiments, on the other hand, provides further validation of the simulation setup. Therefore, my PhD research provides interdisciplinary insight into those two systems based on MD simulations and spectroscopic experiments.

1.2 *Ab initio* MD (AIMD) simulations of trimethylamine *N*-oxide (TMAO)

The first target of my PhD research is trimethylamine *N*-oxide (TMAO). TMAO is known as osmolyte, a substance that controls osmotic pressure. Osmolytes have been exploited to counter the osmotic pressure of salt water of the sea, possibly by the earliest life on earth,[10] which are believed to have emerged in the sea. Different types of osmolytes have been used by different kinds of animals, and TMAO as osmolyte has been widely used by fish to counteract the osmotic pressure of sodium chloride in sea water.[11] TMAO is also related to mammalian animals including humans. TMAO is accumulated in mammalian kidneys, and especially for humans, the high concentration of TMAO in the human cardiovascular system is related to some diseases including chronic kidney diseases and coronary artery diseases, by affecting cholesterol metabilism.[12] In the case of humans, some amount of TMAO is derived from choline, carnitine, or lecithin contained in foods, which are converted to TMAO by gut bacteria.[12] Some amount of TMAO is also obtained by eating fish or other animals.[13] Another aspect of TMAO is that TMAO is a chemical chaperone, a chemical substance that stabilizes the structure of proteins.[14] It is suggested that the stabilization effect of TMAO on proteins is mediated by in-between water molecules, as a result of thermodynamically unfavorable interaction between TMAO and proteins.[14]

These two functions of TMAO as osmolyte and chemical chaperone possibly depend on its strong interaction with the surrounding water molecules, via the hydrophilic oxygen (O_{TMAO}) atom.[14] In addition to the hydrophilic O_{TMAO} atom, TMAO also has hydrophobic methyl groups on the same molecule, which complicates its interaction with water molecules. To reveal the mechanism for those functions of TMAO, it is required to understand the structure and dynamics of water molecules around TMAO, which are basic information that provides us with deeper insight into the mechanisms.

Among water properties around TMAO, my PhD research focuses on the rotational dynamics of water molecules in aqueous TMAO solutions. Water rotational dynamics around TMAO was measured using pump-probe spectroscopy by Rezus and Bakker in 2007. To analyze their data, they assumed the presence of "immobilized" water molecules that hardly rotate within the timescale of their experiment. This idea of "immobilized" water molecules has a long history starting from Frank and Evans in 1945, who assumed the presence of "iceberg"-like water molecules near hydrophobic surfaces to give a mechanism to the hydrophobic effect based on their thermodynamic measurements. After the paper by Rezus and Bakker, Laage and co-workers performed force field MD simulations of aqueous TMAO solution in 2007, aiming at investigating the presence of "immobilized" water around TMAO molecules. However, they observed only a moderate slowdown of water reorientation around TMAO, which they attributed to the lack of hydrogen bond partners as a result of the excluded volume of TMAO. In 2012, Hunger *et al.*, performed further pump-probe spectroscopy measurements for water reorientation, and suggested that there are O-H groups with "very slow" rotational dynamics that have a red-shifted stretch frequency, which intuitively means that the O-H groups are hydrogen-bonded to the hydrophilic part of TMAO, rather than present near the hydrophobic region. To further understand the water behavior around TMAO, more accurate methods were needed, because in general, the intermolecular interaction is not guaranteed to be properly described by force field models and the dynamics of a molecule is often sensitive to its local environment.

Therefore, we performed *ab initio* MD (AIMD) simulations of aqueous TMAO solutions, aiming at accurately investigating the water rotational dynamics around TMAO. AIMD simulation employs electronic structure theory for force evaluation. One of the advantages of this method is that force fields, which are a set of equations and parameters that are used for force evaluation in conventional force field MD, are not needed. With this method, we can obtain the trajectory of a given system in a reliable way in the sense that force evaluation is governed by electronic structure theory. AIMD can be powerful when we simulate a mixture of different molecules, and especially when the interaction between different kinds of molecules is strong, because force field models are usually fit to reproduce properties of pure systems and it is not guaranteed that force field models provide accurate values for the quantities of mixture.[15]

We have investigated the rotational dynamics of water molecules (1) near the hydrophilic oxygen (O_{TMAO}) atom of TMAO, and (2) near the hydrophobic methyl groups. Our results show that the water reorientation is strongly slowed down near the hydrophilic

O_{TMAO} atom, which agrees with the finding by Hunger *et al.*, while it is only moderately slowed down near the hydrophobic methyl groups, which agrees with the simulation results by Laage *et al*., though detailed comparison can be done after defining the words "strongly slowed down" and "moderately slowed down". Thus we can conclude that there are two types of water rotational dynamics around TMAO: One is slow rotational dynamics around the hydrophilic part of TMAO, and the other is fast rotational dynamics around the hydrophobic methyl groups. This finding is reminiscent of water behavior on the protein surface, where fast and slow water molecules are found near the hydrophobic amino groups and hydrophilic groups, respectively.[16]

We further reveal that the strongly slowed-down dynamics near the hydrophilic O_{TMAO} atom originates from the hydrogen bond between O_{TMAO} and water molecules, which we find long-lived and highly-directional by AIMD simulations. Our AIMD simulations employed for analyzing water behavior around TMAO are expected to add new information for understanding macroscopic functions of TMAO as osmolyte and chemical chaperone.

1.3 Force field modification for TMAO

Next, my PhD research was directed to developing a new force field model for TMAO. A force field model is a set of equations and parameters that are used to evaluate forces acting on atoms, used in conventional force field MD simulations. In contrast to AIMD simulations, which require a full electronic structure theory, force field MD simulations have the advantage that the simulation is less expensive, enabling large-scale and/or long-time simulations. These kinds of simulations are often needed to answer questions involving macroscales, and to run reliable simulations, reliable force field models are required. However, developing a reliable force field is a tough task, reflecting the fact that force field models have a set of parameters which should reproduce several quantities, including densities, thermodynamic properties, structural and dynamical properties, and some reference data by quantum chemistry calculations such as electrostatic potentials.

For example, for describing the water molecule, a lot of force field models have been developed after the first development by Bernal and Fowler in 1933.[17] Some of the widely used force fields for water are the SPC[18] (1981) and SPC/E[19] (1987) models by Berendsen, and the TIP3P[20] (1983) and TIP4P[20] (1983) models by Jorgensen. The SPC/E model, a modified version of SPC, provides good density and diffusion constant that compare well with experiment.[19] TIP3P yields a specific heat that compares well with experiment.[21] TIP4P

has a dummy atom resulting in a better description of the electrostatic potential.[20] Water models are implemented in molecular dynamics software as a part of force field sets such as AMBER (Assisted Model Building and Energy Refinement), CHARMM (Chemistry at HARvard Molecular Mechanics), GROMOS (GROningen MOlecular Simulation), and OPLS (Optimized Potential for Liquid Simulations). These sets of force field models have been extensively used for simulations of small molecules, macromolecules, DNA, proteins, and other biomolecules,[22] where MD simulations have been a powerful tool to investigate biological phenomena such as protein folding,[23] which cannot be fully understood only with experiment.

However, despite the remarkable importance of force field MD simulations, one of their shortcomings is the lack of polarizability, which results in problems with describing directional hydrogen bonds. For example, the thermodynamic properties of proteins, which are important for the folding of proteins, tend to be inaccurately calculated[23–25] using widely-used MD force fields such as AMBER and CHARMM. One of the origins for this inaccuracy is considered to be a lack of atomic polarizability, resulting in inaccurate description of directional hydrogen bonds within proteins which are responsible for the secondary structure of proteins.[23] One direct approach to overcome this problem is taking into account the hydrogen-bond directionality via introduction of lone electron pairs[26] or via introduction of hydrogen-bond energy terms,[27–29] or adding the polarizability of protein atoms using Drude oscillators.[30,31] Studies using these approaches evidence that the inclusion of hydrogen-bond directionality or polarizability improve the thermodynamic properties of proteins, which relate to the folding of proteins.

My PhD research here aims at modifying a force field model for TMAO, including the "strong" hydrogen bonds with the surrounding water molecules. Our modification was done by including three dummy sites around the hydrophilic oxygen (O_{TMAO}) atom of TMAO, which mimic the lone electron pairs on O_{TMAO}. This kind of modification has been used to modify force field models for the water molecule (TIP5P[32]) and for small organic molecules aiming at improving[26] the thermodynamic properties of those aqueous solutions. However, it has not been investigated if this kind of modification works well for the current molecule of TMAO, which has three lone pairs on O_{TMAO} and forms "strong" hydrogen bonds with water molecules.

Our force field MD simulations using the modified force field for TMAO provide a better description of the hydrogen-bond structure between TMAO and water, and the TMAO···water hydrogen-bond dynamics, that agree better with AIMD simulation data

compared with other force field models for TMAO. Other data involving water properties around TMAO produced by the current force field show better agreement with AIMD data. These results manifest that the current way of force field modification is a good option to modify other organic molecules that have lone electron pairs, which are often important in biological processes. My PhD research here also indicates that proper choice of force field model crucially depends on what we aim to investigate.

1.4 Dynamical heterogeneities in room temperature ionic liquids (RTILs)

The next target of my PhD research is room temperature ionic liquids (RTILs). RTILs are ions that are in the liquid state at room temperature. As a result of strong Coulombic interaction between the ions, RTILs have a low vapor pressure and, due to their re-usability, RTILs have been called 'green solvents'. In addition, RTILs are expected to be used as embalming fluids that replace toxic formalin,[33] for the desulfurization of diesel fuels,[34] and as lubricants.[35] The properties of RTILs can be modified by substituting constituent cations and anions. However, the number of potentially obtainable RTILs is at least a million for binary RTILs, and 10^{18} for ternary RTILs.[36] Thus, to obtain useful RTILs, or to design RTILs, screening by simulation will be a powerful method, providing important information on the microscopic structure and dynamics.

It has been proposed that RTILs exhibit spatial heterogeneity in the sense that they form ionic domains and hydrophobic domains. This spatial heterogeneity was first observed by Wang and Voth in 2005, using molecular dynamics (MD) simulations.[37] They found that the tail carbon atoms of RTILs (1-alkyl-3-methylimidazolium nitrate) tend to aggregate, resulting in the spatial heterogeneity. After that, Lopes and Pádua found that RTILs form ionic domains and hydrophobic domains at the nanoscale, which they described as "nanoscale segregation" of RTILs. Since then, the presence of spatial heterogeneity or nanoscale segregation has been an important aspect of RTILs.

In addition to the structural properties of RTILs, their dynamical properties have been widely investigated as well, suggesting that the dynamics of RTILs also show a heterogeneous behavior. The dynamic heterogeneity in RTILs was first mentioned by Voth's group in 2004,[38] earlier than their finding of the spatial heterogeneity. In that paper,[38] they showed that the diffusions of the constituent ions are heterogeneous in the sense that there exist different timescales for the diffusion of the ions. They attributed this dynamical heterogeneity to the different local environments with long lifetime, for example, as a result of domain formation.

In 2004, Ribeiro observed that, in addition to the translational motion, the rotation of constituent ions also exhibit dynamical heterogeneity reflecting their different local environments.

In addition to the observation that the dynamics of a given aspect (translation of cations, for example) have a distribution of timescales, the different dynamics of different constituents have been also investigated. In 2010, Fruchey and Fayer dissolved polar and apolar probe molecules into RTILs and investigated the rotational dynamics of the probe molecules by measuring their fluorescence anisotropy decays.[39] They found that the rotational dynamics of the polar and apolar molecules differ, which they claimed is due to their different local environments: The polar molecules are dissolved in the ionic domains of RTILs, and as a result of the strong Coulombic interaction between them, the rotational dynamics of the polar probe molecule is slow. On the other hand, the apolar molecules are dissolved in the hydrophobic domains of RTILs, and reflecting their weak van der Waals interaction with surrounding atoms, the rotational dynamics of the apolar probe molecules exhibit fast dynamics. In 2015, Hunger and co-workers used femtosecond infrared spectroscopy to find that the thermal relaxations of the stretching vibrations differ in timescale for the two ends of cationic chains, reflecting their different environments, i.e., ionic domains and hydrophobic domains, which presumably play an important role in thermal dissipation following a chemical reaction.

To explore the molecular level details of such observations, we performed force field MD simulations of RTILs (ethylammonium nitrate, propylammonium nitrate, and butylammonium nitrate), aiming at investigating the dynamics of RTILs and providing insight into these dynamical heterogeneities. Our research reveals that there are two types of heterogeneities in the rotational dynamics. On the one hand, the two ends of the cationic alkyl chain exhibit different rotational timescales, reflecting the spatial heterogeneity. We further find that this dynamical heterogeneity is enhanced with increasing cationic alkyl chain length. Our detailed investigations of the structure and dynamics involving the inter-ionic cation···anion interaction reveal that this enhanced dynamical heterogeneity results from the increased number of anions near the N_{head}-H groups as a result of the larger volume of longer cationic chains.

On the other hand, the dynamical heterogeneity is also manifested in a broad distribution of the rotation timescales of the N_{head}-H groups. The decay of the N_{head}-H rotational correlation function can be very well described by a stretched exponential function. Our further analyses show that the distribution of the timescales reflects the different local

environment around the N_{head}-H groups, which is characterized by a different number of inter-ionic bonds between the N_{head}-H group and nitrate anion. The different local environments persist for a long time as a result of the long-lived ionic "cage" caused by strong Coulombic interaction.[38] We believe that these two types of dynamical heterogeneities are a generic feature of RTILs and thus should be considered when designing new RTILs.

1.5 Outline of this thesis

This PhD thesis is organized as follows. In Chapter 2, the general concept of molecular dynamics (MD) simulation and two types of MD methods including force field MD and *ab initio* MD are explained. In Chapter 3, I report my paper written with my co-authors about water dynamics around TMAO investigated by *ab initio* MD simulations. In Chapter 4, I present another paper about the force field development for TMAO, which was based on our findings from the AIMD simulations. In Chapter 5, I describe another paper on the dynamics of room temperature ionic liquids (RTILs), which investigates the presence of dynamical heterogeneities in RTILs. In Chapter 6, the conclusions of my thesis are presented.

Chapter 2
Methods

2.1 Molecular dynamics simulations

2.1.1 Equations of motion

Molecular dynamics (MD) simulations are methods of computer simulation for tracing the time development of the coordinates and velocities of given atoms. Here "atoms" in simulations usually represent the nuclei of real atoms. MD simulations can be subdivided into different types, and one way to categorize them is to see if the nuclei are treated by classical mechanics or quantum mechanics. Some MD methods including conventional force field MD simulations and *ab initio* MD simulations treat nuclei by classical mechanics: The time evolution of the atoms is governed by Newton's equations of motion. Some other MD methods, including path integral MD simulations (including centroid MD[40,41] and ring polymer MD), treat nuclei by quantum mechanics: quantum effects can be included by different approaches. When the quantum effect of nuclei is crucial, for example, in the case of proton transfer, such quantum mechanics-based methods should be considered. On the other hand, when quantum effects can be neglected, we can use MD methods with Newton's equations of motion for the temporal evolution of the atomic coordinates, to reduce computational time. Since the methods mentioned here treat all atoms explicitly, these methods are termed all-atom MD simulations. If we are interested in large-scale and/or long-time phenomena, we can even reduce the computational time by using coarse-grained MD simulations, where a group of atoms is approximated by a single "coarse-grained" particle.

When we are interested in "intermediate" systems in length scale and time scale, the MD methods using Newton's equations of motion for nuclei can be a good option: The atomistic behaviors are simulated, which are "averaged" with coarse-grained MD simulations, and computational time is relatively reduced by neglecting quantum effects of nuclei. Then what we have to do is to solve the Newton's equations of motion for a given system.

Consider a system of N atoms with coordinates $\boldsymbol{r}^N = (\boldsymbol{r}_1, \ldots, \boldsymbol{r}_N)$ and velocities $\boldsymbol{v}^N = (\boldsymbol{v}_1, \ldots, \boldsymbol{v}_N)$. Then the corresponding Newton's equations of motion can be written as,[2]

$$\boldsymbol{F}_i(t) = -\nabla U(\boldsymbol{r}^N) = m_i \dot{\boldsymbol{v}}_i(t), \tag{2.1}$$

$$\boldsymbol{v}_i(t) = \dot{\boldsymbol{r}}_\iota(t), \tag{2.2}$$

where $U(\boldsymbol{r}^N)$ is the potential energy function of the system, which is a function of the coordinates $\boldsymbol{r}_i$, and m_i is the mass of the system. Here, evaluation of the potential energy and consequently forces acting on atoms is the key point when performing MD simulations, which classifies two types of MD simulations: force field MD simulation and *ab initio* MD simulation. In force field MD simulations, this potential function is termed "force field model", and force evaluation is done using force field models. On the other hand, in *ab initio* MD simulations, this potential function and consequently the forces on atoms are evaluated using electronic structure theory. Details for these two MD methods are described below. Once we know how to evaluate forces, we can integrate the equations, which yields the temporal evolution of the coordinates (and velocities) of the atoms.

2.1.2 Numerical integration

Since it is usually impossible to integrate the equations of motion analytically, MD simulations are performed by numerically integrating the equations. One widely used numerical integration method is the velocity Verlet integration, which guarantees that the energy of the system is "nearly converged" (termed symplectic integration) and the time evolution satisfies time-reversibility. A modified version of the velocity Verlet integration, called leap-frog integration, is also widely used. However, note here that numerical integration methods implemented in MD software packages seem slightly different from the normal methods described above, reflecting complicated equations of motion as a result of a lot of parameters such as thermostats, barostats, constraints, and so on.

Most of the numerical integration algorithms are derived from the Taylor expansion of coordinates $\boldsymbol{r}_i$. To derive the velocity Verlet integration, we expand coordinates $\boldsymbol{r}_i$ at times $t + \Delta t$ and $t - \Delta t$, as

$$\boldsymbol{r}_i(t+\Delta t) = \boldsymbol{r}_i(t) + \dot{\boldsymbol{r}}_i(t)\Delta t + \frac{1}{2}\ddot{\boldsymbol{r}}_i(t)\Delta t^2 + \frac{1}{6!}\dddot{\boldsymbol{r}}_i(t)\Delta t^3 + O(\Delta t^4), \tag{2.3}$$

$$\boldsymbol{r}_i(t-\Delta t) = \boldsymbol{r}_i(t) - \dot{\boldsymbol{r}}_i(t)\Delta t + \frac{1}{2}\ddot{\boldsymbol{r}}_i(t)\Delta t^2 - \frac{1}{6!}\dddot{\boldsymbol{r}}_i(t)\Delta t^3 + O(\Delta t^4). \tag{2.4}$$

By adding these expansions yields

$$\boldsymbol{r}_i(t+\Delta t) + \boldsymbol{r}_i(t-\Delta t) = 2\boldsymbol{r}_i(t) + \ddot{\boldsymbol{r}}_i(t)\Delta t^2 + O(\Delta t^4)\,. \tag{2.5}$$

Using Newton's equation of motion gives

$$\boldsymbol{r}_i(t+\Delta t) = 2\boldsymbol{r}_i(t) - \boldsymbol{r}_i(t-\Delta t) + \frac{\boldsymbol{F}_i(t)}{m_i}\Delta t^2 + O(\Delta t^4)\,. \tag{2.6}$$

This integration method is called the Verlet integration. This method indicates that the coordinate at $t + \Delta t$ can be calculated by the coordinates at t and $t - \Delta t$. This equation still holds after replacing Δt with $-\Delta t$, which manifests that the Verlet integration is time-reversible. We can see that the Verlet integration method requires the coordinates $\boldsymbol{r}_i(t)$ and $\boldsymbol{r}_i(t - \Delta t)$ to calculate $\boldsymbol{r}_i(t + \Delta t)$. From Eqs. (2.3) and (2.4), the velocities $\boldsymbol{v}_i(t)$ can be calculated as,

$$\boldsymbol{v}_i(t) = \frac{\boldsymbol{r}_i(t+\Delta t) - \boldsymbol{r}_i(t-\Delta t)}{2\Delta t} + O(\Delta t^2), \tag{2.7}$$

And in the Verlet integration, the velocities $\boldsymbol{v}_i(t)$ are calculated as follows,

$$\boldsymbol{v}_i(t) = \frac{\boldsymbol{r}_i(t+\Delta t) - \boldsymbol{r}_i(t-\Delta t)}{2\Delta t}. \tag{2.8}$$

This means that the calculation of $\boldsymbol{v}_i(t)$ has "order" 1 (meaning this calculation has error for Δt^2 and higher orders), resulting in that the calculation of $\boldsymbol{r}_i(t)$ has order 2. Thus, the Verlet method is classified as "second-order method".

We see that the calculation of $\boldsymbol{v}_i(t)$ requires the coordinates $\boldsymbol{r}_i(t + \Delta t)$ and $\boldsymbol{r}_i(t - \Delta t)$. This means that the velocities at present time $\boldsymbol{v}_i(t)$ depends on the coordinates at future time $\boldsymbol{r}_i(t + \Delta t)$, which complicates the numerical calculation. Also the calculation of velocities using Eq. (2.7) can cause a numerical error because the coordinates $\boldsymbol{r}_i(t + \Delta t)$ and $\boldsymbol{r}_i(t - \Delta t)$ tend to be similar. For those reasons, a different set of equations, called the velocity Verlet method, is often used in MD simulations.

In the velocity Verlet integration, the velocities $\boldsymbol{v}_i(t)$ are calculated from the velocities at the previous step $\boldsymbol{v}_i(t - \Delta t)$, instead of being calculated by coordinates. The relation between these two velocities can be obtained by adding two equations,

$$\boldsymbol{r}_i(t + \Delta t) = 2\boldsymbol{r}_i(t) - \boldsymbol{r}_i(t - \Delta t) + \frac{\boldsymbol{F}_i(t)}{m_i}\Delta t^2 + O(\Delta t^4), \tag{2.9}$$

$$\boldsymbol{r}_i(t) = 2\boldsymbol{r}_i(t - \Delta t) - \boldsymbol{r}_i(t - 2\Delta t) + \frac{\boldsymbol{F}_i(t-\Delta t)}{m_i}\Delta t^2 + O(\Delta t^4), \tag{2.10}$$

yielding together with Eq. (2.7),

$$\boldsymbol{v}_i(t) = \boldsymbol{v}_i(t - \Delta t) + \frac{\Delta t}{m_i}\frac{\boldsymbol{F}_i(t) + \boldsymbol{F}_i(t-\Delta t)}{2}, \tag{2.11}$$

which describes the temporal evolution of the velocities. Accordingly, the temporal evolution of atomic coordinates can be calculated as follows. First, we rewrite Eq. (2.6) as,

$$\boldsymbol{r}_i(t + \Delta t) = \boldsymbol{r}_i(t) + \frac{1}{2}\boldsymbol{r}_i(t) + \frac{1}{2}\boldsymbol{r}_i(t) - \boldsymbol{r}_i(t - \Delta t) + \frac{\boldsymbol{F}_i(t)}{m_i}\Delta t^2 + O(\Delta t^4). \tag{2.12}$$

Then, substituting one of the terms (1/2) $\boldsymbol{r}_i(t)$ using (2.6) yields,

$$\boldsymbol{r}_i(t + \Delta t) = \boldsymbol{r}_i(t) + \frac{1}{2}[\boldsymbol{r}_i(t) - \boldsymbol{r}_i(t - 2\Delta t)] + \left[\frac{\boldsymbol{F}_i(t)}{m_i} + \frac{\boldsymbol{F}_i(t-2\Delta t)}{2m_i}\right]\Delta t^2 + O(\Delta t^4). \tag{2.13}$$

Using the definition (2.8) and subsequently Eq. (2.11) yields,

$$\boldsymbol{r}_i(t + \Delta t) = \boldsymbol{r}_i(t) + \Delta t \cdot \boldsymbol{v}_i(t) + \frac{\boldsymbol{F}_i(t)}{2m_i}\Delta t^2 + O(\Delta t^4), \tag{2.14}$$

which describes the temporal evolution of atomic coordinates. This velocity Verlet method is widely used for MD simulation, including CP2K,[42,43] the MD simulation package that I used for my PhD research.

2.1.3 Periodic boundary conditions

In MD simulations, a box called unit cell is prepared and periodic boundary conditions are used on the unit cell. This means that when an atom gets out of the cell, it is regarded that the atom comes back into the cell from the other side of the cell. In other words, a unit cell is surrounded by the same cells. By doing this, we can do simulation as if the simulation contains a large amount of atoms. When calculating intermolecular interaction on a given molecule from other molecules through Lennard-Jones potential, interactions only by the nearest molecules in those replicated cells are considered, which is called minimum image convention. On the other hand, Coulomb interaction is calculated using the Ewald method,[44] to take into account the long-range behavior of Coulombic potential.

2.1.4 Thermostats

Running MD simulations under conditions that correspond to those of the experiments such as at constant pressure or constant temperature is important when we are interested in those conditions. Here I would like to briefly explain the way how MD simulations are performed at constant temperature, which is used throughout my PhD research.

The most basic MD simulation method assumes the *NVE* ensemble (microcanonical ensemble), which is described by the Hamiltonian:

$$H(\boldsymbol{r}^N,\ \boldsymbol{p}^N) = \sum_i \frac{\boldsymbol{p}_i^2}{2m_i} + \sum_{i<j} U(\boldsymbol{r}_i, \boldsymbol{r}_j), \tag{2.15}$$

Where $\boldsymbol{r}^N = (\boldsymbol{r}_1, \cdots, \boldsymbol{r}_N)$ and $\boldsymbol{p}^N = (\boldsymbol{p}_1, \cdots, \boldsymbol{p}_N)$ are the set of coordinates and momenta of the molecules. From this Hamiltonian, Newton's equations of motion are yielded. To yield *NVT* ensemble (at constant temperature), Nosé introduced an extra degree of freedom *s* to take into account the effect of heat bath:[45]

$$H'(\boldsymbol{r}^N,\ \boldsymbol{p}'^N, p_s, s) = \sum_i \frac{\boldsymbol{P}_i^2}{2m_i s^2} + \sum_{i<j} U\big(\boldsymbol{r}_i, \boldsymbol{r}_j\big) + \frac{p_s^2}{2Q} + gkT\ln(s), \tag{2.16}$$

Where $\boldsymbol{p}'^N$ is the momenta of molecules in a virtual system that evolves faster than the real system: Time *t*' in the virtual system is related to time t in the real system as:

$$dt = \frac{dt'}{s}, \tag{2.17}$$

And then the momenta $\boldsymbol{p}'^N$ in the virtual system are related to the momenta $\boldsymbol{p}^N$ in the real system as:

$$\boldsymbol{p}^N = \frac{\boldsymbol{p}'^N}{s}. \tag{2.18}$$

$\boldsymbol{p}_s$ and Q are imaginary momentum and mass that are related to the heat variable s. $gkT\ln(s)$ is included to yield *NPT* ensemble when $g = 3N$. By deriving Hamilton's equations of motion for the virtual system, we obtain:

$$\dot{\boldsymbol{r}}_i = \frac{\boldsymbol{p}_i}{m}, \tag{2.19}$$

$$\dot{\boldsymbol{p}}_i = F_i - \frac{\dot{s}}{s}\boldsymbol{p}_i, \tag{2.20}$$

$$\dot{s} = s\frac{\boldsymbol{p}_s}{Q}, \tag{2.21}$$

$$\dot{\boldsymbol{p}}_s = \sum_i^N \frac{p_i^2}{m_i} - gkT., \tag{2.22}$$

By using the extra parameters s and $\boldsymbol{p}_s$, we see that the momenta $\dot{\boldsymbol{p}}_i$ is modified to yield a target temperature. Other thermostats also aim at scaling the momenta (or velocities) that yield a distribution corresponding to a target temperature. To control the system temperature more strongly, it can be considered that the system is surrounded by a larger bath (larger baths) introduced by Hoover.[46]

2.2 Force Evaluation

2.2.1 Force field MD simulations

The probably most common way of evaluating forces is to use force field models. A force field model is a set of equations and parameters that are used for force evaluation. In general, the potential energy function $U(\boldsymbol{r}^N)$, called "force field" in the context of force field MD simulations, can be divided into the intermolecular term (non-bonded term) $U_{\mathrm{NB}}(r_{ij})$ and intramolecular term (bonded term) $U_{\mathrm{NB}}(r_{ij})$,

$$U(r_{ij}) = U_{\mathrm{NB}}(r_{ij}) + U_{\mathrm{B}}(r_{ij}), \tag{2.23}$$

where r_{ij} denotes the distance between atoms i and j. Here it is assumed that the force field can be written in a pair-wise fashion (pair-wise potential).

The intermolecular term, or non-bonded term $U_{\mathrm{NB}}(r_{ij})$ usually consists of two terms: the Coulombic term and the van der Waals term written as,

$$U_{\mathrm{NB}}(r_{ij}) = \frac{q_i q_j}{4\pi\epsilon_0 r_{ij}} + 4\epsilon_{ij}\left[\left(\frac{\sigma_{ij}}{r_{ij}}\right)^{12} - \left(\frac{\sigma_{ij}}{r_{ij}}\right)^{6}\right], \tag{2.24}$$

where, in the first term (Coulombic term) q_i denotes the charge on atom i, ϵ_0 denotes the permittivity of vacuum. On the other hand, in the second term (van der Waals term), which is termed Lennard-Jones potential, ϵ_{ij} denotes the depth of the potential and σ_{ij} denotes the distance where the potential reaches its minimum.

The intramolecular term, or bonded term $U_B(r_{ij})$ describes the intramolecular degrees of freedom such as bonding, bending, and torsional motions. The bonded term can be written as

$$U_B(r_{ij}) = \sum_{\text{bonds}} \frac{k_b}{2}(b - b_0)^2 + \sum_{\text{angles}} \left[\frac{k_\theta}{2}(\theta - \theta_0)^2 + \frac{k_u}{2}(u - u_0)^2\right] + \sum_{\text{dihedrals}} k_\phi[1 + \cos(n\phi - \delta)], \quad (2.25)$$

where the first, second, and third terms describe the potentials for bonding, bending, and torsional motions, respectively. In the bonding term, k_b denotes the force constant, b denotes the bond distance, and b_0 denotes the equilibrium bond distance. In the bending term, k_θ denotes the force constant, θ denotes the bend angle, and θ_0 denotes the equilibrium bend angle. Here in the second term, the Urey-Bradley term (k_u: force constant, u: distance between the 1, 3 atoms, u_0: equilibrium distance between atoms 1 and 3) is included, which describe the 1,3 interaction (i.e., the interaction between two atoms that are separated by another atom). In the term for torsional motion, n denotes the multiplicity, k_φ denotes the torsional parameter, φ denotes the dihedral phase, and δ denotes the phase shift. These intermolecular terms are used for "flexible" force field models that allow intermolecular motions, while these terms are not used for "rigid" force field models.

2.2.2 *ab initio* MD simulations

Ab initio MD simulations[43] (AIMD) are a type of MD simulations which use electronic structure theory for forces evaluation. By virtue of the electronic structure theory, we can obtain a reliable reference that is free of parameters, which are used in force field MD simulations. Among AIMD simulations, in this thesis, I have used Born-Oppenheimer MD (BOMD) simulation. Note that BOMD can be compared to Car-Parrinello MD simulation (CPMD), which uses fictitious mass for electrons that can circumvent the time-consuming convergence process in electronic structure theory. Because I have exclusively used BOMD in this thesis I briefly explain the principles of BOMD simulation in the following.

As in the force field MD simulations, the method is based on Newton's equations of motion for time-evolution of atoms,

$$F(\boldsymbol{r}_i) = -\nabla U(\boldsymbol{r}_i) = M\dot{\boldsymbol{v}}_i(t), \quad (2.26)$$

$$\boldsymbol{v}_i(t) = \dot{\boldsymbol{r}}_i(t), \quad (2.27)$$

where, for a given system consisting of atoms with coordinates $X(t)$, velocities $V(t)$, and masses M, forces on the atoms $F(X)$ are evaluated through the potential function $U(X)$. The evaluation of these forces $F(X)$ is done using electronic structure theory in AIMD simulations. Here, Density Functional Theory (DFT) is usually employed for evaluating electronic structure, because this method provides reliable electronic structure at limited computational cost, compared to other types of electronic structure theory such as Hartree-Fock and post Hartree-Fock methods.

DFT is one of the approaches to solve the fundamental equation for atoms and electrons in nonrelativistic situations, i.e., the Schrödinger equation. Usually, DFT deals with time-independent wave functions (steady states of electrons). Therefore, the Schrödinger equation that we consider is written as:

$$\hat{H}\Psi = E\Psi, \tag{2.28}$$

where $\hat{H}$ is the Hamiltonian operator for the nuclei and electrons, Ψ is the wave function of the system, and E is the energy of the system. Note that this is an eigenvalue equation. E (or the set of the energies E) is an eigenvalue (or the set of eigenvalues) of the operator $\hat{H}$, and Ψ is the corresponding eigenvector (or the set of corresponding eigenvectors). Here Ψ is the wave function that describes the atoms and electrons. By assuming that this wave function Ψ can be written as the product of electronic component ψ_{e} and nuclear components ψ_{n} (Born-Oppenheimer approximation) as

$$\Psi = \psi_{\mathrm{e}} \times \psi_{\mathrm{n}}, \tag{2.29}$$

we can obtain an equation for the electronic wave function ψ_{e}

$$\hat{H}_{\mathrm{e}}\psi_{\mathrm{e}} = E_{\mathrm{e}}\psi_{\mathrm{e}}, \tag{2.30}$$

Where $\hat{H}_{\mathrm{e}}$ describes the Hamiltonian for electrons. By solving this equation (usually using DFT), we can obtain the forces on atoms $F(X)$ as

$$F(X) = -\frac{\partial E_{\mathrm{e}}}{\partial X} = -\langle\psi_{\mathrm{e}}|\frac{\partial \hat{H}}{\partial X}|\psi_{\mathrm{e}}\rangle, \tag{2.31}$$

where the second equality holds by the Hellmann-Feynman theorem.

2.2.3 Density functional theory

As described above, the forces that act on atoms are evaluated using Eq. (2.31) after obtaining the wave function of electrons by usually DFT. Here, I will describe the principles of DFT briefly. The main purpose of DFT is to obtain density functionals for electrons, and the orbitals of electrons are not the direct target of calculation as in molecular orbital theories such as Hartree-Fock and post Hartree-Fock methods.

The derivation of equations in DFT can be obtained from the Schrödinger equation for N electrons as the same as Eq (2.28):

$$\hat{H}\Psi = E\Psi, \tag{2.32}$$

Where $\hat{H}$ denotes the Hamiltonian for the N-electron system, E is the total energy, and Ψ is the wave function, which is a function of the coordinates of the N electrons: $\Psi(\boldsymbol{r}_1, \ldots, \boldsymbol{r}_n)$. The Hamiltonian can be written as:

$$\hat{H} = \left[\hat{T} + \hat{V} + \hat{U}\right] = \sum_i^N \left(-\frac{\hbar^2}{2m_i}\nabla_i^2\right) + \sum_i^N V(\boldsymbol{r}_i) + \sum_{i<j}^N U(\boldsymbol{r}_i, \boldsymbol{r}_j), \tag{2.33}$$

where the first term describes the total kinetic energy of the electrons, $V(\boldsymbol{r}_i)$ is the nucleus-electron interaction energy:

$$V(\boldsymbol{r}_i) = -\sum_i \frac{Z_I e^2}{|\boldsymbol{r}_i - \boldsymbol{R}_I|}, \tag{2.34}$$

as a result of N nuclei at positions of $\boldsymbol{R}_I$ with atomic numbers Z_I (hereafter, a set of units that satisfies $4\pi\varepsilon_0 = 1$ is used). $U(\boldsymbol{r}_i, \boldsymbol{r}_y)$ is the electron-electron interaction energy:

$$U(\boldsymbol{r}_i, \boldsymbol{r}_j) = \frac{e^2}{|\boldsymbol{r}_i - \boldsymbol{r}_j|}, \tag{2.35}$$

In the Hamiltonian, the effect of nuclei (the coordinates of nuclei) is found in the second term as parameter that are regarded constant while solving the Schrödinger equation.

The electron density as a function of position $\boldsymbol{r}$, which is an important quantity in DFT, can be obtained by integrating the N-electron wave function $\Psi(\boldsymbol{r}_1, \ldots, \boldsymbol{r}_n)$ with respect to $\boldsymbol{r}_2$, …, $\boldsymbol{r}_n$, to make it a function of the position of a single electron (note that electrons are not distinguishable):

$$\rho(\boldsymbol{r}) = N\int d\boldsymbol{r}_2 \cdots \int d\boldsymbol{r}_N\, \Psi^*(\boldsymbol{r}, \boldsymbol{r}_2, \ldots, \boldsymbol{r}_N)\Psi(\boldsymbol{r}, \boldsymbol{r}_2, \ldots, \boldsymbol{r}_N), \tag{2.36}$$

where the number of electrons N is multiplied so that this quantity is the electron density that yields:

$$\int \rho(\boldsymbol{r})d\boldsymbol{r} = N. \tag{2.37}$$

Assuming that we can write the total energy of the N-electron system as a functional of the electron density as $E = E[\rho]$, the electron density for the ground state can be obtained as a functional that minimizes the total energy (variational principle). This is the main concept of density functional theory. However, the expression of the total energy E (or the Hamiltonian $\hat{H}$) as a functional of the electron density ρ seems difficult, and usually electron orbitals are introduced for DFT calculations, as in molecular orbital theories (such as Hartree-Fock and post Hartree-Fock methods). The total energy calculated by the Hartree-Fock method is related to the first ionization energy by Koopman's theorem.[47]

Assume that the N-electron wave function can be written as the Slater determinant of one-electron orbitals as

$$\Psi(\boldsymbol{r}_1, \boldsymbol{r}_2, \dots, \boldsymbol{r}_N) = |\phi_1(\boldsymbol{r}_1)\ \ \phi_2(\boldsymbol{r}_2) \dots \phi_N(\boldsymbol{r}_N)|, \tag{2.38}$$

which is a simple mathematical expression that satisfies the anti-symmetry requirement (the Pauli exclusion principle) for electrons (fermionic particles). Here, $\phi_1(\boldsymbol{r}_1), \dots, \phi_N(\boldsymbol{r}_N)$ are electron orbitals for single electrons. Using Eq. (2.24), the electron density $\rho(\boldsymbol{r})$ can be expressed as:

$$\rho(\boldsymbol{r}) = \sum_i^N |\phi_i(\boldsymbol{r})|^2. \tag{2.39}$$

By substituting Eq. (2.38) into Eq. (2.33) with Eq. (2.34), we obtain the Kohn-Sham equation:

$$\left(-\frac{\hbar^2}{2\mathrm{m}}\nabla^2 + V_{\mathrm{H}}(\boldsymbol{r}) + V_{\mathrm{xc}}(\boldsymbol{r})\right)\phi_i(\boldsymbol{r}) = \epsilon_i \phi_i(\boldsymbol{r}), \tag{2.40}$$

where $V_{\mathrm{H}}(\boldsymbol{r})$ is the Hartree (or Coulomb) potential written as:

$$V_{\mathrm{H}}(\boldsymbol{r}) = \int \frac{e^2 \rho(\boldsymbol{r}')}{|\boldsymbol{r}-\boldsymbol{r}'|} d\boldsymbol{r}', \tag{2.41}$$

which originates from the Coulomb interaction between two electronic densities. This term is also found in the Hartree-Fock method and has the classical interpretation that this is a Coulomb potential at $\boldsymbol{r}$ generated by the electronic density $\rho(\boldsymbol{r})$. On the other hand, $V_{\mathrm{xc}}(\boldsymbol{r})$ is the exchange-correlation potential, which is related to the exchange-correlation functional $E_{\mathrm{xc}}[\rho]$ as:

$$V_{\mathrm{xc}}(\boldsymbol{r}) = \frac{\delta E_{xc}[\rho]}{\delta \rho}. \tag{2.42}$$

The exchange-correlation functional $E_{\mathrm{xc}}[\rho]$, which is one of the fundamental setups for calculating the electronic structure along with basis sets, consists of two contributions: the exchange functional and correlation functional. The exchange functional describes quantum mechanical interaction between electrons, which originates from the fact that electrons are indistinguishable and the wave function of electrons is represented by a Slater determinant. This exchange functional corresponds to the exchange integral involving molecular orbitals $\phi_i(\boldsymbol{r})$ and $\phi_j(\boldsymbol{r})$ in the Hartree-Fock equation. However, in DFT, the exchange functional is represented as a functional of the electronic density $\rho(\boldsymbol{r}) = \sum_i^N |\phi_i(\boldsymbol{r})|^2$. On the other hand, the correlation functional, which is the other contribution to the exchange-correlation functional, is introduced to describe the electronic correlation, which is not included in the Hartree-Fock method due to the use of a single Slater determinant for electronic wave function. This term, which is not present in the Hartree-Fock equation, yields better description of the total energy in DFT. This treatment of the electronic correlation is relatively inexpensive compared with post-Hartree Fock methods, where a linear combination of Slater

determinants is used to describe the electronic wave function, resulting in more expensive computational cost than the Hartree-Fock methods.

2.2.4 Exchange-correlation functional

As described above, the exchange-correlation functional is needed to solve the Kohn-Sham equation to obtain molecular orbitals, and consequently the electronic density and desired quantities, in our case, forces acting on atoms. There are a series of exchange functionals and correlation functionals used for DFT calculations.

The exchange functionals are developed based on the approximation for the exchange integral in the Hartree-Fock equation into a functional of the electronic density:[48]

$$E_{\mathrm{x}}^{\mathrm{LDA}}[\rho] = -\frac{3}{2}\left(\frac{3}{4\pi}\right)^{1/3} \sum_{\sigma} \int \rho_{\sigma}^{4/3} d^3\boldsymbol{r}, \tag{2.43}$$

Where σ denotes "up" or "down" for electron spin. This type of approximation is called the local density approximation (LDA), meaning that it is approximated as a local functional of ρ only. To improve the accuracy of the approximation, the effect of the gradient of the electronic density $\nabla\rho$ is often included, resulting in the generalized gradient approximation (GGA). For example, the well-known B88 exchange functional[48] is calculated by:

$$E_{\mathrm{x}}^{\mathrm{B88}}[\rho] = E_{x}^{\mathrm{LDA}}[\rho] - \sum_{\sigma} \int \rho_{\sigma}^{4/3} \{\frac{\zeta x_{\sigma}^2}{1+6\zeta x_{\sigma} \sinh^{-1} x_{\sigma}}\} d^3\boldsymbol{r}, \tag{2.44}$$

where

$$x_{\sigma} = \frac{|\nabla\rho_{\sigma}|}{\rho_{\sigma}^{4/3}}, \tag{2.45}$$

describes the effect of the gradient of ρ in GGA appoximations. ζ is a parameter, and it is calculated as ζ = 0.042 to fit exchange energies for a series of atoms by Hartree-Fock methods.[48] GGA functionals are widely used for calculating electronic structure. There are other types of exchange functionals with different function forms and parameters, such as PBE and revPBE functionals,[49,50] which I have also used in my PhD research. Those functionals contains the derivative of are called GGA functionals

On the other hand, the correlation functionals have rather complicated form to account for the electronic correlation, the effect that is not properly included in the Hartree-Fock method. For example, the widely-used LYP correlation functional has the form:[51]

$$E_{\mathrm{c}}^{\mathrm{LYP}}[\rho] = -a \int \frac{1}{1+d\rho^{-\frac{1}{3}}} \{\rho + b\rho^{-\frac{2}{3}} \left[\frac{3}{10}(3\pi^2)^{\frac{2}{3}} \rho - 2t_W + \left(\frac{1}{9}t_W + \frac{1}{18}\nabla^2\rho\right)\right] \mathrm{e}^{-c\rho^{-\frac{1}{3}}})\} \, d^3\boldsymbol{r}, \tag{2.46}$$

Where

$$t_W = \frac{1}{8}\left(\frac{|\nabla\rho|^2}{\rho} - \nabla^2\rho\right), \quad (2.47)$$

and these equations contain a set of parameters:[51] a = 0.04918, b = 0.132, c = 0.2533.

After assuming specific functional forms for the exchange-correlation functional in the Kohn-Sham equation, by solving the equation, we can obtain the molecular orbitals. To computationally solve the equation, the molecular orbitals are expanded by basis sets, the other important factor in DFT calculations.

2.2.5 Basis set

A widely used basis set consists of atomic orbitals such as s, p, d,… orbitals of atoms. Molecular orbitals are described as a linear combination of these atomic orbitals. Those atomic orbitals, in turn, are written using Gaussian orbitals: $\exp(-\alpha r^2)$. For example, s orbitals are represented as a linear combination of Gaussian orbitals, p orbitals are represented as a linear combinations of the funtions $x\cdot\exp(-\alpha r^2)$, $y\cdot\exp(-\alpha r^2)$, and $z\cdot\exp(-\alpha r^2)$, and so on. Importantly, by using Gaussian orbitals as basis sets, the integrals in the Kohn-Sham equation can be performed analytically, and the Kohn-Sham equations becomes a matrix equation for orbital coefficients, resembling the Roothaan equations in the Hatree-Fock method:[52]

$$\mathbf{FC} = \mathbf{SC}\boldsymbol{\epsilon}, \quad (2.48)$$

Where **F** is the Fock matrix, **C** is the matrix of coefficients, **S** is the overlap matrix of the basis functions, and $\boldsymbol{\epsilon}$ is the matrix of orbital energies. A similar matrix equation is obtained for the Kohn-Sham equation with **F** being replaced by a matrix for $-\frac{\hbar^2}{2\mathrm{m}}\nabla^2 + V_{\mathrm{H}}(\boldsymbol{r}) + V_{\mathrm{xc}}(\boldsymbol{r})$ using relevant basis set. Therefore, the Kohn-Sham equation can be solved through the matrix equation of the coefficient matrix. This equation can be solved iteratively (self-consistent field): Using the initial coefficient matrix **C**, the matrix **F** is calculated, and the equation is solved by diagonalizing the matrix **F** and resulting coefficient matrix **C** is compared with the original matrix **C**, the process of which will be repeated until we obtain a converged values for the matrix **C.** Finally, using the coefficient matrix **C**, we obtain molecular orbitals $\{\phi_i(\boldsymbol{r})\}$ and the electronic density $\rho(t)$, and consequently the forces on atoms by Eq. (2.32). In the CP2K package, Gaussian basis sets and plane wave basis sets are used simultaneously.[53]

Chapter 3

Ab Initio Liquid Water Dynamics in Aqueous TMAO Solution

We employed *ab initio* molecular dynamics simulations of trimethylamine *N*-oxide(TMAO)-D_2O solution to investigate the effect of TMAO on the dynamics of surrounding D_2O molecules. By decomposing surrounding D_2O molecules into three groups, namely those near the hydrophilic oxygen (O_{TMAO}) atom of TMAO (G1), those near the hydrophobic methyl groups of TMAO (G2), and the rest (G3), we find that the rotational dynamics of D_2O molecules near the hydrophilic O_{TMAO} atom are significantly slow. This slow dynamics are the result of the strong $O_{TMAO}\cdots D_{D2O}$-O_{D2O} hydrogen bond. We find that this rotational motion is governed by the two mechanisms: (1) rotation after breaking the $O_{TMAO}\cdots D_{D2O}$-O_{D2O} hydrogen bond, and (2) rotation with the hydrogen bond intact. By checking the spatial distribution of the hydrogen bond using angle-resolved radial distribution function and hydrogen bond formation correlation function, we reveal that the $O_{TMAO}\cdots D_{D2O}$-O_{D2O} hydrogen bond is highly directional and long lived. These properties of the hydrogen bond are not observed by molecular dynamics simulations with a conventional force field. This study manifests that careful choice of simulation methods or force fields is crucial to see the dynamics of water molecules near negatively-charged atoms, like O_{TMAO}.

3.1 Introduction

Trimethylamine *N*-oxide (TMAO) is a molecule that consists of hydrophilic oxygen (O_{TMAO}) atom and three hydrophobic methyl groups. This type of molecule is called amphiphile and widely found in nature including soaps, detergents, and lipids. When dissolved in water, the hydrophilic O_{TMAO} atom forms strong hydrogen bonds with water molecules, while the hydrophobic methyl groups prevent surrounding water molecules from making hydrogen bonds with themselves.[54] TMAO is found in the cell of fish, and used as chemical chaperone[14,55] (substance that stabilizes proteins[56]) and osmolyte (substance that controls osmotic pressure). TMAO stabilizes the structure of proteins[14,55,57] and RNAs,[58] and

counteracts the destabilization of proteins by urea.[11,59] In the muscle tissues of deep-sea animals, the concentration of TMAO is elevated, which ameliorates the detrimental effects of hydrostatic and osmotic pressure on enzyme function.[60–62] It has been proposed that TMAO molecules are expelled from protein surfaces, and TMAO stabilized the structure of proteins via in-between water molecules, rather than direct interaction between TMAO and proteins.[63–68] This shows that the mechanism of how TMAO stabilizes protein structure is complicated[14,59,63,69–76] and molecular level understanding of the TMAO-water interaction is needed to clarify the role of TMAO in biologically relevant processes. Furthermore, the understanding of TMAO-water interaction will be useful to understand the interaction between water and other amphiphilic molecules, for example, zwitterionic lipids.[77]

Intermolecular interactions between TMAO and water molecules have been intensely investigated by theoretical methods[14,59,63,72,74,78–90] and experimental approaches, including linear infrared (IR),[72,88,91,92] mid-IR pump-probe,[93–95] two-dimensional IR,[96] Raman,[97,98] NMR,[89,99] and dielectric relaxation[91,100] spectroscopies. By using pump-probe spectroscopy of the O-D groups in isotopically diluted water, Rezus and Bakker have shown that the reorientational dynamics of water molecules in aqueous TMAO solutions slows down with increasing the concentration of TMAO.[93] They investigated the reorientational dynamics of water molecules around various types of hydrophobic solutes, and they concluded that the slowed-down dynamics of water rotation are caused by the hydrophobic part of the solutes, and water molecules are “immobilized” near the hydrophobic parts. This strongly slowed-down dynamics have been challenged by NMR experiment,[99] force field MD simulations of aqueous TMAO solution,[82] and AIMD simulations of aqueous methanol solutions, which have reported that the slow-down of reorientational dynamics of water molecules near the hydrophobic parts is not “immobilized”, rather limited.[101] A further time-resolved IR study has shown[95] that the slowdown of water rotational dynamics is less pronounced near the hydrophobic regions, and instead, water rotational dynamics is more pronounced near the hydrophilic parts. Especially in the case of aqueous TMAO solutions, the interaction between water molecules and the hydrophilic oxygen (O_{TMAO}) atom of TMAO is suggested dominant for the slow-down mechanism of water dynamics.[95,102] In their research, the strong hydrogen-bond interaction is found between water molecules and the negatively charged O_{TMAO} atom, which has been concluded by the significant red-shift (over 100 cm^{-1}) of the O-D stretch vibration in the IR absorption spectra with respect to the peak frequency of pure D_2O.[72] In the time-resolved IR study, they have excited the red-shifted O-D stretching mode at a frequency of 2440 cm^{-1} using pump pulse, and they have probed the same mode, yielding selectively the

rotational dynamics of water molecules that are considered hydrogen-bonded to the O_{TMAO} atom. By their experiment at high concentration of TMAO, they have revealed that the rotational dynamics of the O-D group with the red-shifted stretching mode are significantly slowed down, and because this red-shift is caused by the strong hydrogen-bond interaction between O_{TMAO} and water molecules, they concluded that water rotational dynamics are largely slowed down near the hydrophilic O_{TMAO} atom. In this sense, "immobilized" water are found near the hydrophilic part of the molecule. This observation agrees with dielectric relaxation experiment, which suggests that TMAO strongly binds to 2-3 water molecules at all concentrations.

Molecular dynamics (MD) simulations have revealed that the rotational or reorientational motion of water molecules is governed by large angular jumps (molecular jump mechanism).[103,104] The reorientation of water molecules is achieved by breaking their existing hydrogen bonds, followed by forming new hydrogen bonds. Thus new hydrogen-bond partners need present near the reorienting water molecules, which brings about short-lived bifurcated hydrogen bonds. Laage and co-workers have intensely performed force field MD simulations of aqueous TMAO solutions to investigate the slowdown of water reorientation in this solution.[81,82,103–109] In their simulations, they used the SPC/E water model[19] and the TMAO force field model.[110] They have found that the reorientational motion of water molecules is only moderately slowed down by the presence of TMAO molecules in aqueous TMAO solutions.[82] The moderate slowdown near TMAO molecules has been explained by the excluded volume caused by the TMAO molecules.[82] Due to the presence of TMAO molecules, water molecules near the solutes lack their hydrogen-bond partners that are needed by the molecular jump mechanism, which suppresses the chance of water rotation. Furthermore, they have indicated that the slowed-down dynamics of water molecules in aqueous TMAO solution, which has been measured by pump-probe experiment,[93] is not the consequence of the "iceberg" structure of water molecules near the hydrophobic parts. They also addressed that the hydrophilic part of TMAO should contribute to the slowdown of water dynamics in aqueous TMAO solutions. This study agrees with the NMR study that no "iceberg" structure around the hydrophobic part of TMAO has been observed.[99]

Force field MD simulations depend on parameters such as point charges and van der Waals interactions for description of intermolecular interactions. In the case of simulations of aqueous TMAO solutions, the intermolecular interactions between water molecules and TMAO are described by these parameters. When we would like to investigate the interaction between TMAO and water, especially the strong interaction between the hydrophilic O_{TMAO}

atom and water, which is characterized by the red-shift of the O-D stretch mode, It is important to check the accuracy of the description of the intermolecular interactions. The force field MD simulation has reported a red-shift of ~30 cm^{-1}, but this red-shift seems underestimated compared with experimental data (more than 100 cm^{-1},[72] ~55 cm^{-1},[95] and 290 cm^{-1} red-shifts[91]). Density functional theory (DFT) calculations of the system consisting of one TMAO molecule and three water molecules report that the atomic charge on the O_{TMAO} atom reduced by ~10 % upon the formation of the hydrogen bonds between TMAO and water.[111] This reduction of charge is usually difficult to take into account. Thus, these studies suggest that *ab initio* modeling is required to precisely investigate the effect of the intermolecular interactions between TMAO and water molecules on the rotational dynamics of water molecules.

In this chapter, we perform *ab initio* MD (AIMD) simulations and force field MD simulations of the mixture of deuterated TMAO and D_2O, and pure D_2O, to investigate the reorientational dynamics of water molecules near the TMAO molecule. AIMD has been a power tool to investigate the dynamics of liquids, where intermolecular interactions play important roles. For example, AIMD simulations of bulk water have revealed cooperative hydrogen-bond dynamics, which has been missing in force field MD simulations.[112,113] In our research here, we selectively study the O-D groups that are near the hydrophilic O_{TMAO} atom, and that are near the hydrophobic methyl groups. By doing this, we reveal the different contributions of these O-D groups to their vibrational density of states and their rotational dynamics. Our AIMD simulations show that the O-D groups that are interacting with O_{TMAO} atom contribute to vibrational density of states at a frequency of 2300 cm^{-1}, which is strongly red-shifted from the O-D stretch frequency in pure D_2O and agrees with experimental findings.[72,92,95] We find that the lifetime of TMAO-D_2O hydrogen bond is very long, and this hydrogen bond strongly slows down the rotational dynamics of D_2O molecules hydrogen-bonding to TMAO. The mechanism of this slow-down by the O-D$\cdots O_{TMAO}$ hydrogen bond can be explained as follows. While the O-D$\cdots O_{TMAO}$ hydrogen bond is formed, the O-D group has to rotate with the large TMAO molecule, which strongly slows down the rotational dynamics. Alternatively, one the strong hydrogen bond is broken, the O-D group can moves away from the TMAO molecule, then can rotate more freely as in pure water.

We compare our AIMD results with the results obtained by force field MD simulations and find that the slow dynamics of water rotation near the hydrophilic O_{TMAO} atom is underestimated with the force field MD simulations. We attribute this difference between the dynamics by AIMD and force field MD to the description of charge on O_{TMAO}. In the force

field MD simulations, a point charge is put on the O_{TMAO} atom, which makes it difficult to reproduce highly-directional hydrogen bond between O_{TMAO} and water, which we find by AIMD simulations. Finally, we briefly discuss the effect of DFT functionals and basis sets on the water dynamics in aqueous TMAO solutions.

This paper is organized as follows. In section 3.2, we report protocols used for our AIMD and force field MD simulations. In section 3.3, we discuss the simulated vibrational density of states, rotational dynamics, hydrogen-bond dynamics, and angle-resolved radial distribution functions (RDFs) obtained with AIMD and force field MD simulations. In this section, the effect of DFT functionals and basis sets on the water dynamics is also discussed. Finally, section 3.4 is devoted to our conclusions.

3.2 Method

3.2.1 Simulation protocols

We performed AIMD and force field MD simulations of deuterated TMAO (d-TMAO)-D_2O solutions and pure D_2O. The simulation cell size was set to 14.62 Å × 14.62 Å × 14.62 Å. The cell contained 1 d-TMAO molecules and 100 D_2O molecules, yielding a density of 1.109 g/cm^3. The cell size was evaluated to reproduce the density of corresponding TMAO-H_2O solution.[95,114] Here we assumed that the structure is not affected upon the isotope exchange. On the other hand, for simulation of pure D_2O, the cell size was set to 12.429 Å × 12.429 Å × 12.429 Å, yielding a density of 1.108 g/cm^3. In both cases, periodic boundary conditions were used. The simulations were carried out in the NVT ensemble, using the thermostat of canonical sampling through velocity rescaling.[115] A temperature of 320 K was used for both the AIMD simulations and force field MD simulations. The time step for integration of equations of motion was set to 0.5 fs. Our Simulations were performed using the CP2K package.[42]

3.2.2 AIMD simulations

We performed Born-Oppenheimer AIMD simulations of dTMAO-D_2O solution using different kinds of functionals and basis sets. As exchange and correlation functionals, we used the Becke-Lee-Yang-Parr (BLYP)[48,116] and revised Perdew-Burke-Ernzerhof (revPBE)[49,50] functionals, plus the van der Waals correction of Grimme's D3 method.[117] Adding the van der Waals correction terms have been recognized crucial to reproduce correct density and dynamics of pure water.[118–120] We used the Goedecker-Teter-Hutter pseudopotentials[121] and the hybrid Gaussian and plane wave method implemented in QUICKSTEP.[53] As basis sets, we

used DZVP and TZV2P for the Gaussian wave functions and a density cutoff of 400 Ry was used for the plane waves.[122] We performed combinations of BLYP/DZVP, BLYP/TZV2P, and revPBE/TZV2P levels of theory to study the effect of functionals and basis sets on the structure and dynamics of water molecules.

For simulation of dTMAO-D_2O solution, two sets of initial configurations were prepared for each combination of functional and basis sets by using force field MD simulations, and from these configurations we performed MD simulations in a parallel manner. First, for equilibration, we ran 15 ps (BLYP/DZVP and BLYP/TZV2P) and 20 ps of NVT simulations. After this equilibration, we obtained production runs used for analysis. The total lengths of these production runs were 477 ps (BLYP/DZVP), 643 ps (BLYP/TZV2P), and 320 ps (revPBE/TZV2P). On the other hand, for simulation of pure D_2O, one initial configuration was generated using force field MD simulation. From this initial configuration, we ran equilibration runs for 35 ps (BLYP/DZVP), 50 ps (BLYP/TZV2P), and 320 ps (revPBE/TZV2P). After these equilibrations, we obtained production runs with lengths of 266 ps (BLYP/DZVP), 457 ps (BLYP/TZV2P), and 374 ps (revPBE/TZV2P).

3.2.3 Force field MD simulations

In addition AIMD simulations, we performed force field MD simulations of dTMAO-D_2O solution and pure D_2O. For D_2O, we used a flexible model of SPC/Fw.[123] For dTMAO, we used a flexible force field that is parametrized based on quantum chemistry calculation.[110] After 100 ps of equilibration, we obtained 1.4 ns of production run for dTMAO-D_2O solution, and 0.4 ns production run for pure D_2O, respectively.

3.2.4 Categorization of O-D groups

Because we aim at investigating the effect of different parts of TMAO on the rotational dynamics of water molecules, namely the hydrophilic part and hydrophobic part of TMAO, we categorized the total 200 O-D groups of D_2O molecules into three subensembles, G1, G2, and G3. Ensemble G1 consist of the O-D groups that are hydrogen-bonded the O_{TMAO} atom: Here, an O-D group is defined hydrogen-bonded to the O_{TMAO} atom, if the intermolecular distance of $O_{TMAO}…D_{D2O}$ is less than 2.7 Å.[124,125] For discussion on the mechanism of the rotation of D_2O molecules, which will be discussed later, we defined ensemble G1' out of ensemble G1, for the O-D groups that remain hydrogen-bonded to O_{TMAO} during the simulation time. Next, ensemble G2 consists of the O-D groups that are near one of the methyl groups of TMAO: An O-D groups is grouped into G2 if the O-D group is not

categorized into G1 and, in addition to that, the intramolecular distance of $C_{TMAO}…D_{D2O}$ less than 5.0 Å (C_{TMAO} is one of the carbon atoms of TMAO). This cutoff value of 5.0 Å was taken from a study on aqueous tetramethylurea solutions using Car-Parrinello MD simulations.[126,127] Note that the reason why the cutoff radius of 5.0 Å for G2 is much larger than the cutoff radius of 2.27 Å for G1 is because the G2 cutoff radius is defined not from the hydrogen atoms that expose to surrounding water molecules, but from the buried carbon atoms. Finally, ensemble G3 consists of the rest of the O-D groups which are not categorized into either G1 or G2. Note that G1, G2, and G3 are mutually exclusive.

Our AIMD simulations yielded that, on average, G1 contains 2.9 O-D groups, which is comparable with the numbers of 2 (dielectric relaxation measurement,[100] nuclear Overhauser effect measurement,[128] and thermodynamics analysis[76]) and 2-3 (dielectric measurement[95]). The average numbers of O-D groups categorized into G1, G2, and G3 are shown in Table 1.

Table 3.1. Average number of O-D groups contained in sub-ensembles G1, G2, and G3 by AIMD and force field MD simulations.

	BLYP/DZVP	BLYP/TZV2P	revPBE/TZV2P	Force field
G1	2.9	2.9	2.9	2.5
G2	46.5	47.1	46.8	47.0
G3	150.6	150.0	150.3	150.5

3.3 Results

3.3.1 Vibrational density of states

First, we investigated a peak in vibrational spectra of aqueous TMAO solution which seem to correspond to the O-D groups that are hydrogen-bonded to the O_{TMAO} atom. To this end, we calculated the vibrational density of states (VDOS) of the O-D stretch mode. The VDOS, which we denote $R(\omega)$, can be calculated by Fourier transform of the velocity autocorrelation function involving the O-D stretch mode as

$$R(\omega) = \int_0^{\tau_{\mathrm{cut}}} \langle \boldsymbol{v}_{\mathrm{OD}}(t) \cdot \boldsymbol{v}_{\mathrm{OD}}(0) \rangle e^{-i\omega t} dt \ , \qquad (3.1)$$

Where $\boldsymbol{v}_{\mathrm{OD}}(t)$ denotes the relative velocity of the D atom of D_2O, with respect to the O atom on the same D_2O at time t. The time correlation was cut out at time τ_{cut} for numerical reason, which was set to 1 ps in this study. ‹…› denotes the thermal average. The calculated real parts of VDOSs for subensembles G1 (near the hydrophilic O_{TMAO} atom) and G2 (near the

hydrophobic methyl groups) are shown in Figure 3.1 as well as the real part of the VDOS for pure D_2O.

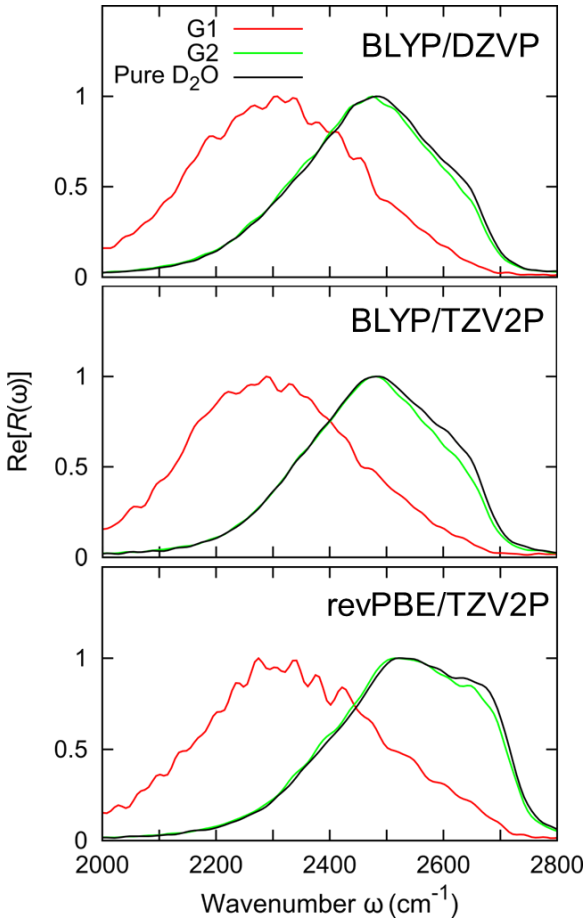

Figure 3.1. Real parts of the calculated VDOS, $R(\omega)$, for the G1 and G2 O-D groups in the TMAO-D_2O solution. The VDOS of the pure D_2O is also plotted.

The VDOS spectra of the G1 O-D groups have a peak centered on 2300 cm^{-1}, which indicates that the strongly red-shifted peak which was observed experimentally,[72] arises from the G1 O-D groups (O-D groups that are hydrogen-bonded to the O_{TMAO} atom). On the other hand, the VDOS spectra for the G2 O-D groups resemble the VDOS spectra for pure D_2O, which indicates that hydrogen-bonds in G2 are not so different from hydrogen-bonds in pure D_2O. Note that the strong red-shift is not observed in the VDOS spectra by classical force field MD simulations. This means that AIMD simulations yield substantially stronger hydrogen-bonds between TMAO and water molecules, than the classical force field MD simulations do.

Here, note that the peak width of the G1 VDOS spectra is broad, although the G1 O-D groups are strongly hydrogen-bonded and consequently the distribution of the hydrogen-bond strength is narrower. This seemingly contradictory relation originates from the fact that the sensitivity of the hydrogen-bond frequency on the hydrogen-bond strength is pronounced in the red-shifted region of frequency.[129]

3.3.2 Rotational Dynamics

Now we focus on the rotational dynamics of D_2O molecules around the TMAO molecule. The rotational dynamics of D_2O molecules can be investigated via the anisotropy decay of the O-D group, which can be experimentally measured using time-resolved IR spectroscopy.[130] The anisotropy of the O-D group is defined

$$C_2(t) = \frac{2}{5}\langle P_2\left(\frac{\boldsymbol{r}_{\mathrm{OD}}(t)\cdot\boldsymbol{r}_{\mathrm{OD}}(0)}{|\boldsymbol{r}_{\mathrm{OD}}(t)||\boldsymbol{r}_{\mathrm{OD}}(0)|}\right)\rangle \qquad (3.2)$$

where $\boldsymbol{r}_{\mathrm{OD}}(t)$ denotes the O-D vector on D_2O molecule at time t, and $P_2(x)=(1/2)(3x^2\text{-}1)$ is the second Legendre polynomial. This equation is used for calculating the O-D anisotropy decay in the pure D_2O system. On the other hand, for calculating the O-D anisotropy decays in dTMAO-D_2O solution, we used this equation for G1, G2, and G3 subensembles,

$$C_{\mathrm{G}i}(t) = \frac{2}{5}\langle P_2\left(\frac{\boldsymbol{r}_{\mathrm{OD}}(t)\cdot\boldsymbol{r}_{\mathrm{OD}}(0)}{|\boldsymbol{r}_{\mathrm{OD}}(t)||\boldsymbol{r}_{\mathrm{OD}}(0)|}\right)\theta_{\mathrm{G}i}(0)\rangle, \qquad (3.3)$$

where $\theta_{\mathrm{G}i}(t)$ is a step function whose value is 1 when the relevant D atom is in subensemble G_i at time t, and otherwise 0.

The calculated anisotropy functions $C_{\mathrm{G1}}(t)$, $C_{\mathrm{G2}}(t)$, and $C_{\mathrm{G3}}(t)$ are shown in Figure 3.2. First, we can see that the decay for subensemble G3 resembles the decay for pure D_2O, which means that the rotational dynamics of O-D groups away from the TMAO molecule (in the second hydration shell and beyond) are similar to the dynamics in pure D_2O. This agrees with an earlier Car-Parrinello MD study on the effect of an amphiphile (tetramethylurea, TMU) on the dynamics of water.[126,127] The G2 O-D groups show slower decays than the O-D groups in G3 or pure D_2O, meaning that O-D groups near the hydrophobic methyl groups of TMAO rotate more slowly than in pure D_2O, or away from TMAO molecules. This slowdown has been observed by previous force field MD simulations as well.[82,126] Here we note that the magnitude of the slowdown depends on the cutoff radius for defining G2: If we take a cutoff value of 3.0 Å for G2 instead of 5.0 Å, resulting in ~5 O-D groups included in G2, we have more slowed-down dynamics in G2 (See Figure 3.2, dashed green lines). From single exponential fits to the anisotropy decays, we evaluated time constants for the decays, and the magnitudes of slowdown in G2 compared to G3 were calculated ~1.1-1.3 Å (5 Å cutoff) and

~1.2-1.4 Å (3 Å cutoff). Our data show that the slowdown of water reorientation around the hydrophobic methyl groups of TMAO is not pronounced (a time constant of 10 ps as proposed previously[93]), but rather moderate. The moderate slowdown of water reorientation is in broad accordance with recent studies including force field MD simulations (slowdown ratio of 1.3-1.5),[82] NMR relaxometry (slowdown ratio of 1.6),[99] and a combined measurement of dielectric relaxation and fs-IR measurement (slowdown ratio of 2.8),[95] which are obtained for low concentrations of aqueous TMAO solutions. If we see subensemble G1, namely O-D groups near the hydrophilic O_{TMAO} atom, we see that the AIMD simulations yield very slow decays for G1 O-D groups. Note that this kind of slow decay is not provided by the classical force field MD simulation. This difference between the AIMD data and the force field MD data will be discussed later. Overall, for all of the O-D anisotropy decays, we see initial sharp drops of decay. These initial drops are due to the librational motion of the O-D groups, followed by slower decays which arise from the rotational motion of the O-D groups.

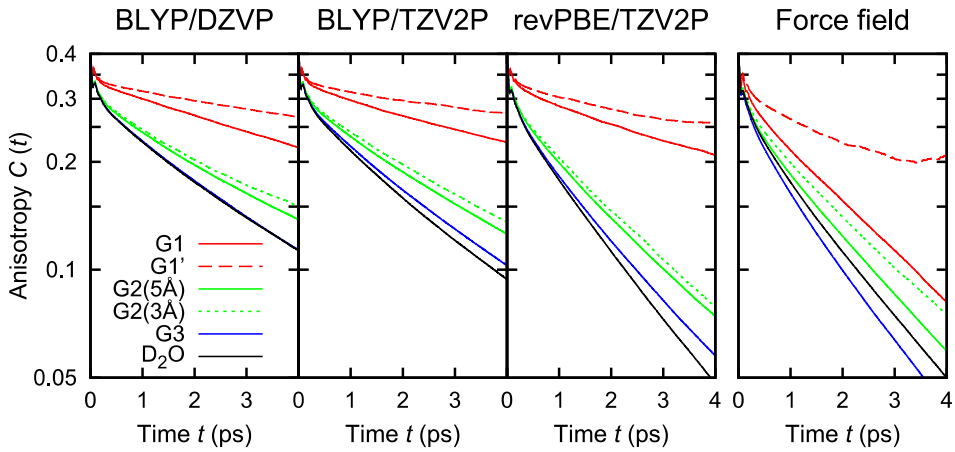

Figure 3.2. Semi-log plots of simulated anisotropy decays of the G1, G2, and G3 O-D groups in the aqueous TMAO solutions, together with the decays of the O-D groups in pure D_2O.

Then, what is the origin of the significantly slow dynamics of O-D groups in G1, namely near the hydrophilic O_{TMAO} atom? To answer this question, now we consider two mechanisms for water rotation, which are shown in Figure 3.3: (i) The O-D group rotates by keeping the O-D…O_{TMAO} hydrogen-bond intact, or (ii) the hydrogen-bond breaks the hydrogen-bond within $t < 4$ ps, gets apart from the O_{TMAO} atom, and thus rotates as freely as in pure D_2O. To see the amounts of these contributions, we calculated the anisotropy decays for the G1 O-D groups that keep the O-D…O_{TMAO} hydrogen-bond intact (G1', thus G1' is a subset of G1), via the equation

$$C_{G1'}(t) = \frac{2}{5}\langle P_2\left(\frac{\boldsymbol{r}_{OD}(t)\cdot\boldsymbol{r}_{OD}(0)}{|\boldsymbol{r}_{OD}(t)||\boldsymbol{r}_{OD}(0)|}\right)\prod_{t_i=0}^{t}\theta_{G1}(t_i)\rangle. \quad (3.4)$$

The anisotropy decays for the G1' O-D groups are shown in Figure 3.2 as well. The figure show that the G1' decays are even slower than the G1 decays. Since the difference between the G1 decay and the G1' decay originates from the O-D groups that break their hydrogen-bonds to the O_{TMAO} atom, we can say that the contribution of the break of the O-D…O_{TMAO} hydrogen-bond is significant on the rotational dynamics of D_2O near the hydrophilic O_{TMAO} atom.

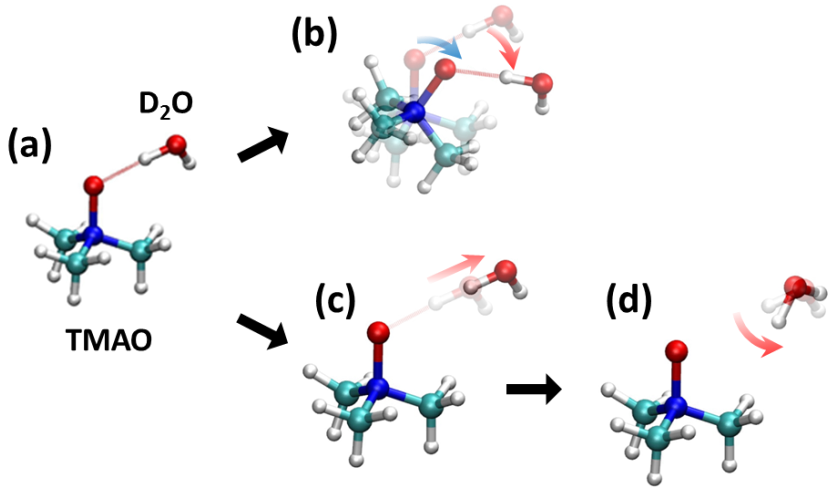

Figure 3. The two mechanisms for the G1 O-D groups to lose the orientational information. The upper route ((a) to (b)) shows that the O-D group keeps O-D...O_{TMAO} hydrogen bond intact and rotates as the TMAO + D_2O complex (denoted as sub-ensemble G1'), while the lower pathway ((a), (c), to (d)) shows the mechanism by which reorientation occurs by breaking of the hydrogen bond and subsequent rotation of the O-D group.

After eliminating the contribution of the O-D groups that have broken their hydrogen-bond to the O_{TMAO} atom, on the rotational dynamics of O-D groups in G1, as shown as G1' decays, we still see that the anisotropy functions decay even at a very slow rate. To find out the origin for this very slow decay, thus very slow reorientational motion, we calculated the anisotropy decays of the O-N group of TMAO molecules, to compare the rotational motion of TMAO with the rotational motion of D_2O. To calculate the anisotropy decays of the O-N groups using the same samples as in the calculation of G1' anisotropy decays, we projected the O-N vector in subensemble G1' onto the O-N vector of the TMAO molecule. By doing this, we considered the rotational dynamics of TMAO that are not affected by hydrogen-bond

dissociation between D_2O and TMAO. The anisotropy of the G1' O-D vector projected onto the O-N vector is given by

$$C_{\mathrm{TMAO}}(t) = \frac{2}{5}\langle P_2\left(\frac{\boldsymbol{r}_{\mathrm{OD(p)}}(t)\cdot\boldsymbol{r}_{\mathrm{OD(p)}}(0)}{|\boldsymbol{r}_{\mathrm{OD(p)}}(t)||\boldsymbol{r}_{\mathrm{OD(p)}}(0)|}\right)\prod_{t_i=0}^{t}\theta_{\mathrm{G1}}(t_i)\rangle, \qquad (3.5)$$

$$\boldsymbol{r}_{\mathrm{OD(p)}}(t) = \left(\boldsymbol{r}_{\mathrm{ON}}(t)\cdot\boldsymbol{r}_{\mathrm{OD}}(t)\right)\boldsymbol{r}_{\mathrm{ON}}(t), \qquad (3.6)$$

where $\boldsymbol{r}_{\mathrm{OD(p)}}(t)$ denotes the projected G1' O-D group at time t. By definition, the vector $\boldsymbol{r}_{\mathrm{OD(p)}}(t)$ is parallel to the O-N group of TMAO, and thus the anisotropy decay calculated by eq 3.6 represents the rotation of TMAO.

The projected G1' O-D anisotropy decays are shown in Figure 3.4, along with the G1 and G1' anisotropy decays (see Table 3.2 as well). The decay behaviors of the G1' anisotropy and the projected G1' anisotropy resemble each other, which indicates that the two reorientations of the O-D groups and the O-N group of TMAO are on a similar timescale. From this result, we can infer that the O-D group that are hydrogen-bonded to the O_{TMAO} atom can mainly rotate by following the rotation of the TMAO molecule. In other word, the TMAO molecule and the O-D group rotate as the whole complex.

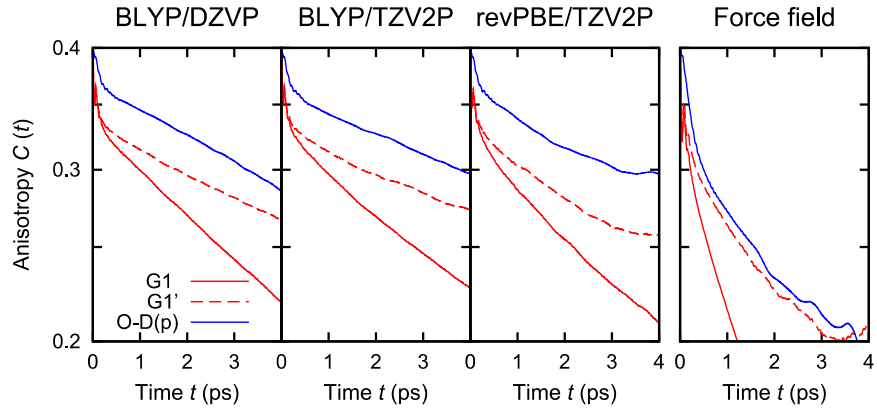

Figure 3.4. Semi-log plots of simulated anisotropy decays of the TMAO molecules with long-lived hydrogen bonds (with O-D groups in the G1' sub-ensemble). For comparison, the G1 and G1' anisotropy decays are also plotted in red.

Table 3.2. Time constants τ (ps) of the anisotropy decays. The decays were fit with the stretched exponential decay $C(t) = A\exp(-t/\tau)$ for 0.5-3.0 ps.

	BLYP/DZVP	BLYP/TZV2P	revPBE/TZV2P	Force field
G1	9.3	10	8.5	3.0
G1'	17	19	13	7.3
G2(5Å)	4.8	4.4	2.8	2.5

G2(3Å)	5.3	4.8	2.9	2.8
G3	3.9	3.6	2.3	2.0
O-D(p)	16	21	16	7.3
Pure D_2O	3.9	3.3	2.1	2.2

As we have seen, significantly slow dynamics of the O-D groups in G1' are yielded by the AIMD simulations. This very slow dynamics qualitatively agree with experimental data.[95] In their time-resolved pump-probe IR experiments, they used pump and probe pulses at around 2450 cm^{-1} which are in a red-shifted region than ordinary O-D stretching mode. Because these red-shifted pulses are considered to interact with O-D groups that are hydrogen-bonded to the O_{TMAO} atom, by using these pulses, they selectively measured the reorientational motion of the O-D groups that are hydrogen-bonded to the O_{TMAO} atom. The contribution of these hydrogen-bonded O-D groups on the spectra will be small then the TMAO concentration is low, but the contribution will be increased as the TMAO concentration is increased. If we see their data of anisotropy decays, at high concentrations of TMAO, the experimentally measured anisotropy decays show significantly slower decays as the TMAO concentration is increased. These very slow decays agree with the slow decays provided with the AIMD simulations. Note here, however, that the pulses at around 2450 cm^{-1} which are intended to interact with the O-D groups that are hydrogen-bonded to O_{TMAO}, also interact with other O-D groups that have this red-shifted frequency even found in pure D_2O. Thus the comparison between the AIMD anisotropy decays and the experimental anisotropy decays can be done only qualitatively, but we assume that this experimental study supports the presence of the very slow rotational dynamics of the O-D groups that are hydrogen-bonded to O_{TMAO}. The presence of this very slow rotational dynamics has been also supported by other experiments, including nuclear Overhauser effect measurement,[128] analyses including density and spectroscopy,[76] and dielectric relaxation data.[95,100] To directly compare simulation and experiment on the anisotropy decay, or rotational dynamics, nonequilibrium AIMD simulations will be a good option.

3.3.3 Hydrogen-bond dynamics

As discussed above, the difference between the G1 and G1' anisotropy decays originates from the contribution from the rotation involving the hydrogen-bond breaking (lower pathway in Figure 3.3). The contribution from this hydrogen breaking to the G1 decay is larger in the force field MD simulations than in the AIMD simulations: By eliminating the

contribution from the hydrogen-bond breaking (from G1 decay to G1' decay), the G1' decay by the force field MD show significantly slower dynamics than the G1 decay. Thus the lifetime of the O_{TMAO}…D hydrogen bond seems crucial when discussing the rotational dynamics of the O-D groups near the O_{TMAO} atom. To see the hydrogen-bond lifetimes, we calculated the hydrogen-bond correlation function[131]

$$p_{\mathrm{HB}}(t) = \frac{\langle h(0)h(t)\rangle}{\langle h(0)\rangle} \qquad (3.7)$$

where the hydrogen-bond formation function, $h(t)$, is 1 when 1.59 Å < $r_{O...D}$ < 2.27 Å, and 0 otherwise.[124,125] $r_{O...D}$ denotes the intermolecular O_{TMAO}…D_{D2O} distance for TMAO-D_2O solutions and the inter molecular O_{D2O}…D_{D2O} distance for pure D_2O. The calculated hydrogen-bond correlation functions are shown in Figure 3.5. We can see that the decays of the functions by AIMD simulations are remarkably slower than the decays by the force field MD simulation, which indicates that the lifetime of the hydrogen bond is much longer by the AIMD simulations. On the other hand, if we see the hydrogen-bond dynamics for pure D_2O, we do not see a pronounced difference between the AIMD data and the classical force field data. These observations indicate that the description of the O_{TMAO}…D hydrogen bond is not properly done by the classical force field MD simulations, though the description of the D_{D2O}…O_{D2O} is fine with the force field MD simulations. Hydrogen-bond lifetimes obtained by fitting with single exponential functions are shown in Table 3.3.

Table 3.3. The hydrogen-bond lifetimes τ of AIMD and force field MD trajectories calculated by fitting the exponential function of $A\exp(-t/\tau)$ to the data in the range of 0.5 ps < t < 20 ps. The unit is in ps.

	BLYP/DZVP	BLYP/TZV2P	revPBE/TZV2P	Force field
O-D…O_{TMAO}	35	45	33	7.6
Pure D_2O	7.8	6.5	4.3	4.3

Lifetimes of 30 – 50 ps for the O-D…O_{TMAO} hydrogen-bond are yielded by the AIMD simulations at 320 K agree with a dielectric spectroscopy study where they showed that at least two of the three hydrogen bonds between O_{TMAO} and D_2O stay intact, yielding a lifetime of at least 50 ps at a temperature of ~300 K.[95,100] Note that the difference of the temperatures, 20 K, changes the dynamics of O-D groups around TMAO due to the at most 20% change of the apparent activation energy for rotation. This 20% of difference can be considered to be

within the differences involving the hydrogen-bond lifetimes caused by different functionals/basis sets. If we focus on the difference of the functionals, it has been known that AIMD simulations using the BLYP functional give rise to slightly overstructured water configurations ever with the van der Waals corrections. AIMD simulations using BLYP have been done at elevated temperature by 15 – 30 K when they want to compare the AIMD simulations with force field MD simulations or with experiments, in order to ameliorate the overstructure by elevating temperature.[132,133] At the elevated temperature, the reorientational motion of water molecules will speed up by ~10% compared to 300 K,[83,134,135] and the discrepancy found here between the hydrogen-bond dynamics by the BLYP-AIMD simulation and force field MD simulation will be slightly overestimated due to the overstructure of water by the BLYP functional. However, even after considering these details, still it is reasonable to say that there is a substantial difference between the hydrogen bond dynamics provided by AIMD simulations and force field MD simulations, and this discrepancy originates from the description of the O_{TMAO}…D_{D2O} hydrogen bond.

3.3.4. Angle-resolved RDFs

Now we will see the origin of the difference between the O_{TMAO}…D_{D2O} hydrogen bonds in AIMD simulations and force field MD simulations. To do this, we can check if there is a difference between the hydration structures. To check the structural difference, we calculated angle-resolved radial distribution functions (RDFs) using our MD trajectories. The angle-resolved RDFs of the D atom of D_2O molecule with respect to the O_{TMAO} atom can be calculated as

$$f(r,\theta) = \frac{1}{2\pi r \cdot \Delta\cos\theta \cdot \Delta r}\frac{V}{N}\langle \Delta N(r,\cos\theta)\rangle, \qquad (3.8)$$

where, for the TMAO-D_2O solutions, r denotes the intermolecular O_{TMAO}…D_{D2O} distance, and θ ($0° \leq \theta \leq 180°$) denotes the angle between the N-O vector on the TMAO molecule and the O_{TMAO}…D_{D2O} vector. On the other hand, we also calculated angle-resolved RDFs for pure D_2O, using the same equation 3.8, where r denotes the intermolecular O…D distance, and θ denotes the angle intramolecular O-D vector and the inter molecular O…D vector for the same O atom. $\Delta N(r, \cos\theta)$ denotes the number of D atoms of D_2O molecules that are in the volume element centered on (r, $\cos\theta$). The calculated RDFs are shown in Figure 3.6.

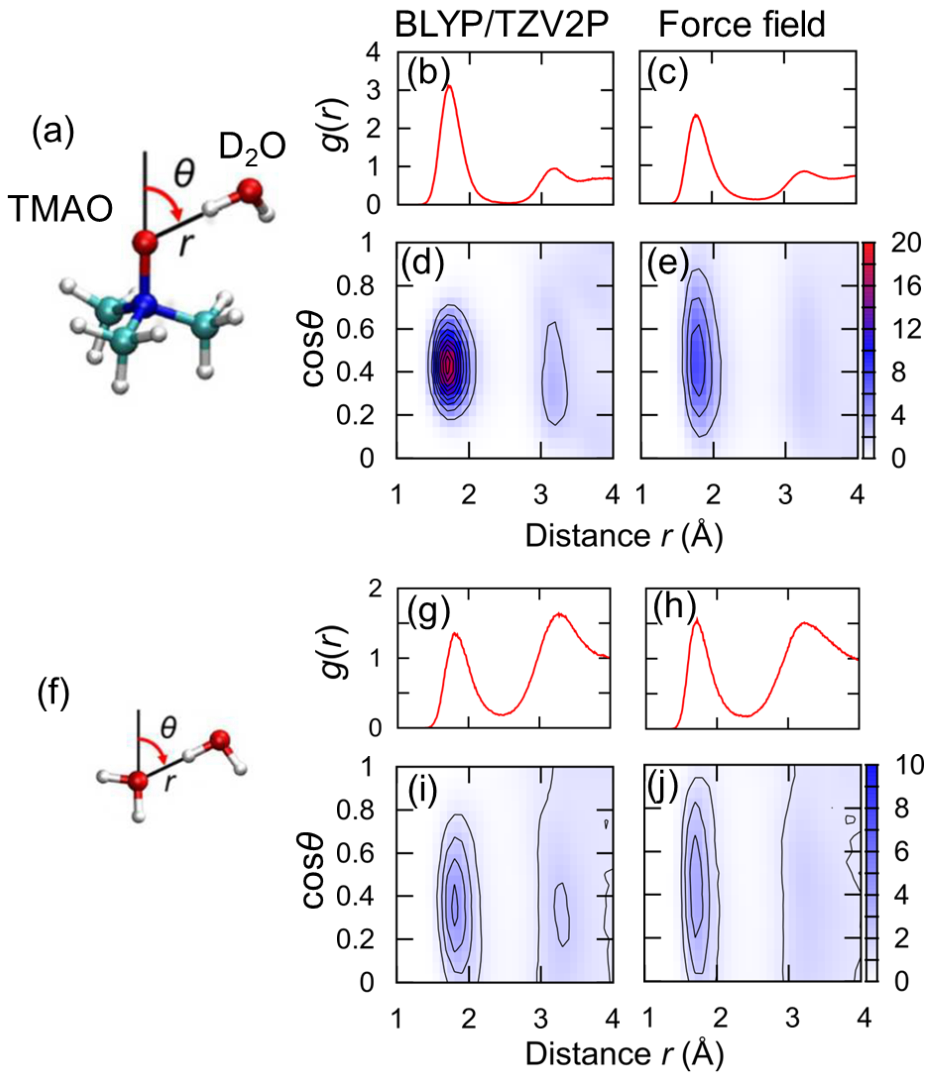

Figure 3.6. RDFs and Angle-resolved RDFs for the D_{D2O} atoms (a-e) in the TMAO-D_2O solution and (f-i) in the pure D_2O calculated with the AIMD simulations at BLYP/TZV2P and the force field MD simulations. (a, f) Schematic pictures for the distance and angle, (b, c, g, h) RDFs, and (d, e, i, j) angle-resolved RDFs. The peak heights of the first hydration shells in the angle-resolved RDF are 19.5 for the AIMD (d) and 7.8 for the force field MD (e) for the TMAO solution, whereas for the pure D_2O the peak heights are 4.4 for the AIMD (i) and 3.7 for the force field MD (j).

The calculated angle-resolved RDFs show that there is a sharp peak in the figure (d) for TMAO-D_2O solution by AIMD simulations at BLYP/TZV2P, which indicates that in this AIMD simulation, the hydrogen-bonded D atom is in a confined angle range (around $\theta \approx 63°$). On the other hand, the force field simulation yields a broader distribution of the angle, meaning that the hydrogen bond is not confined in a certain direction. In other words, the AIMD simulation yields a highly directional hydrogen-bond around O_{TMAO}. As inferred by

the angle of $\theta \approx 63°$, which seems to involve the tetrahedral structure, the high directionality can be considered to arise from the sp^3 atomic orbital of the O_{TMAO} atom. The directionality of the O_{TMAO}…D hydrogen bond is not yielded as seen in Figure 3.6, and this lack of directionality presumably originate from the spherical electrostatic field generated by the single point charge on O_{TMAO}. If we see the angle-resolved RDFs for pure D_2O, there is no big difference between the AIMD data and the force field MD data, supporting that the force field can reproduce the water behavior even without the explicit description of the electrons. The reason why AIMD and force field MD yield different hydration structures for TMAO-D2O solution, but not for pure D2O, presumably originate from the number of lone pairs of electrons: The O_{TMAO} atom has three lone pairs of electrons, while the O_{D2O} atom has two lone pairs of electrons. Note that the weak O_{TMAO}…D_{D2O} hydrogen bond yielded by the Kast model has been pointed out from osmotic activity data.[68,90] There have been proposed other force fields for TMAO[90,136], and it should be checked if these force fields that have single point charges on O_{TMAO}, thus generating spherical electrostatic fields, can yield the long-lived and highly-directional hydrogen bond between O_{TMAO} and D_2O. One way to reproduce the directionality of the O-D…O_{TMAO} hydrogen-bond will be to include virtual sites around O_{TMAO}, as used in TIP4P[20,137] and TIP5P[138] water models. We assume that the AIMD data can be used as reference to develop a force field for TMAO that includes the charge directionality around the O_{TMAO} atom.

3.3.5. Functional/basis set dependence of rotational dynamics in aqueous TMAO solution.

Finally we will address the dependence of water dynamics around TMAO on different functionals and basis sets. Note here that the influence of DFT functionals and basis sets has on the structure and dynamics of pure water molecules has been investigated,[139–142] but less investigation has been done on the effect in aqueous solutions. If we see the rotational dynamics of D_2O around TMAO (Figure 3.2), the main focus of this chapter, the revPBE functional yields faster dynamics than the BLYP for all the cases, namely, G1, G2, G3, and pure D_2O. The result that the revPBE functional provides a shorter time constant for the anisotropy decay of pure D_2O agrees with previous research.[118] Besides, our data show that this trend that revPBE functional provides a faster rotational dynamics of D_2O is also valid for the rotational dynamics in aqueous TMAO solution. If we see the effect of basis sets on the rotational dynamics of D_2O, we do not see a qualitative difference between the basis sets,

indicating that the DZVP basis set is enough to reproduce the dynamics of water molecules around TMAO.

3.4 Conclusion

We performed AIMD simulations of dTMAO-D_2O solution to investigate the rotational dynamics of water molecules around the amphiphile TMAO. Our AIMD simulations provided a red-shift of 160 cm^{-1} for the O-D stretch mode in VDOS spectra for the O-D groups near the hydrophilic O_{TMAO} atom, which agrees with experimental data.[72] This strong red-shift was not yielded with force field MD simulations using a widely-used force field for TMAO.[110] This difference between the AIMD spectra and force field MD spectra originates from the difference in description of the O_{TMAO}…D_2O hydrogen bond. If we see the rotational dynamics of D_2O molecules around TMAO, our AIMD anisotropy decays show that the O-D groups that are near the hydrophilic O_{TMAO} atom rotate considerably slowly due to the hydrogen between O_{TMAO} and D_2O. We revealed that the rotation of the O-D groups near O_{TMAO} is governed by the two mechanisms: (1) The O-D groups rotates with the O_{TMAO}…D_2O hydrogen bond intact, and (2) the O-D groups rotates after breaking the O_{TMAO}…D_2O hydrogen bond.

We also discussed the origin of the different time scales for the O-D rotational dynamics around O_{TMAO} provided by AIMD simulations and force field MD simulations: The O-D rotational dynamics near the hydrophilic O_{TMAO} atom are very slow by AIMD simulations, but not so slow by force field MD simulations. Note that there is no big difference between AIMD and force field MD data (rotational dynamics and hydrogen-bond dynamics) for pure D_2O. By our investigation on the hydrogen-bond directionality around O_{TMAO}, the different timescales of rotational dynamics of O-D groups near O_{TMAO} by AIMD simulations and force field MD simulations presumably involve the directionality of the O_{TMAO}…D_2O hydrogen bond. In the AIMD simulations, highly directional hydrogen bonds around O_{TMAO} are yielded due to the sp3 atomic orbital of O_{TMAO}, while in the force field MD simulations, the directionality of the hydrogen bonds is not pronounced as a result of spherical electrostatic field generated by the single point charge on O_{TMAO}.

Our simulations show that the strongly slowed-down rotational dynamics of water molecules around O_{TMAO} arises from the long-lived and highly-directional hydrogen bond between O_{TMAO} and water. This strong interaction of TMAO with water molecules is presumably essential for its function as chemical chaperone (chemical that stabilizes protein

structure) and as osmolyte (chemical that controls osmotic pressure) as have been proposed widely.[56,143]

Chapter 4

A New Force Field Including Charge Directionality for TMAO in Aqueous Solution

We propose a new force field for trimethylamine *N*-oxide (TMAO) that is designed to reproduce the long-lived and highly-directional hydrogen bonds between the oxygen atom (O_{TMAO}) of TMAO and surrounding water molecules. Based on data obtained *ab initio* molecular dynamics simulations, we introduce three dummy sited around the O_{TMAO} atom to mimic the lone electron pairs on O_{TMAO}. Here we move the negative charge of O_{TMAO} onto the dummy sites. The force field developed here improves both structural and dynamical properties of aqueous TMAO solutions. Furthermore, the force field provided better description of experimentally observed dependence of viscosity upon increasing TMAO concentration. This simple procedure of constructing a new force field makes it easy to implement in molecular dynamics simulations packages and makes it compatible with existing biomolecular force fields. This research will pave the path for further investigations of protein-TMAO interactions in aqueous TMAO solutions.

4.1 Introduction

Trimethylamine *N*-oxide (TMAO) is an amphiphilic molecule that is known as osmolyte found in the cells of deep-sea animals.[60–62] Futhermore, TMAO stabilizes the structure of biomolecules such as proteins[14,55,57] and RNA,[58] and counteracts the protein-destabilizing effect of urea.[59,62–64] It is suggested that TMAO molecules are repelled from the surface region of proteins, thus their protein-stabilizing effect as chemical chaperone is mediated by in-between water molecules.[14,55,57,63–66] For that reason, both structural and dynamical properties of aqueous TMAO solutions have gained a lot of interest.

TMAO consists of its hydrophilic oxygen (O_{TMAO}) atom and hydrophobic methyl groups, which classifies TMAO as amphiphilic molecule. The hydrophilic O_{TMAO} atom forms hydrogen bonds with surrounding water molecules, in other words strongly interacts with water molecules. At the same time, the hydrophobic methyl groups of TMAO prevents

surrounding water molecules from forming hydrogen bonds among themselves. The effect of TMAO on the dynamics of water molecules has been investigated by experiments[93,95,144] and simulations.[81,82] These studies have shown that the rotational dynamics of water molecules around TMAO are to some extent slowed down. The similar finding of slowed-down water dynamics has been done near protein surfaces.[145] We have found, using *ab initio* molecular dynamics simulations (AIMD), that the hydrophilic O_{TMAO} atom forms long-lived and highly-directional hydrogen bonds with water molecules, which significantly slows down the rotational dynamics of water.[146] This kind of strong directionality for hydrogen bonds between TMAO and water molecules agrees with Ref [147].

AIMD simulations have been a powerful tool to investigate intermolecular interactions in virtue of electronic structure theory. However, its high computational cost often makes it difficult to run long-time and large-scale simulations. For this reason, reliable force fields are needed to run force field MD simulations which allow us to run long-time and large-scale simulations. For running reliable MD simulations of aqueous TMAO solutions, a reliable force field for TMAO is required. However, it is challenging to construct a reliable force field model for TMAO, because TMAO forms intermolecular hydrogen bonds with surrounding water molecules.

So far, a number of force field models for TMAO have been proposed: the Kast model,[110] the Netz model,[90] and the Shea model,[136] as well as other models by Canchi *et al.*[68] and by Hölzl *et al.*[148] The Kast model has been developed in 2003 based on *ab initio* quantum chemistry calculations at the MP2 level of theory.[110] The atomic charges were obtained using the electrostatic potential fit technique, and the non-bonded parameters were optimized to reproduce the structure and energetics of hydrated TMAO molecules by *ab initio* calculations. This Kast model, which has been optimized to reproduce crystallographic data, has been widely used to investigate the structure and dynamics in aqueous TMAO solutions,[68,72,74,79,82,84,85,87,89,149,150] though the model has some limitation, for example, in reproducing the density of aqueous TMAO solutions.

In 2013, Netz and co-workers developed another force field for TMAO (the Netz model), aiming at reproducing experimentally-observed thermodynamic properties involving aqueous TMAO solutions.[90] The main difference between the Netz model and the Kast model is the charges on O_{TMAO} atom and the nitrogen atom of TMAO (N_{TMAO}), as well as the radii of the Lennard-Jones parameters of the carbon atoms of the hydrophobic methyl groups. In this year of 2013, another force field model for TMAO was developed by Shea and co-workers

after modifying the Lennard-Jones parameters, aiming at reproducing experimental densities for aqueous TMAO solutions.[136]

Though these force field models reproduce experimentally accessible macroscopic observables, it is worth doing to compare their data with the corresponding data by AIMD simulations, assuming that AIMD yields reliable data that are comparable with experimental data. As shown below (Figures 4.2 and 4.4), these models give rise to either the structure or dynamics of TMAO-water hydrogen bond that differs from the structure or dynamics by AIMD simulations. The Netz model provides larger coordination number of hydrogen atoms of water compared with AIMD, while the Shea model yields shorter lifetime for the TMAO-water hydrogen bond. The discrepancy between each simulation with the TMAO model and AIMD simulations would originates from the description of the negative charge on the hydrophilic oxygen (O_{TMAO}) atom of TMAO. In each of those TMAO force fields, a point charge is assigned to the O_{TMAO} atom which generates spherical electrostatic potential around O_{TMAO}. This spherical potential would not be enough to reproduce high-directional hydrogen bond between O_{TMAO} and water, which we have found by AIMD simulations.[146] This means that a force field for TMAO that takes into account the directionality of the hydrogen bonds would yield structure and dynamics that compares with the data by AIMD simulations.

In this paper, we present a new force field for TMAO that includes the directionality of hydrogen bonds between TMAO and water molecules. We modify the Kast model by putting dummy sites around the O_{TMAO} atom and distribute the negative change of O_{TMAO} onto these dummy sites, aiming at reproducing the highly-directional hydrogen bond. Our modified force field model yields highly-directional hydrogen bond as provided by AIMD simulations, and it provides better description of structure and dynamics involving hydrogen bonds, in the sense that they resemble the data by AIMD simulations. In addition, using the current force field, we investigate the dependence of the viscosity of aqueous TMAO solutions on their concentrations. We see that the current force field provides increasing behavior of the viscosity with increasing the concentration.

This chapter is organized as follows. In section 4.2, we report the details of our force field modification for TMAO and the protocols of our MD simulations. In section 4.3, data by the current force field are presented and discussed. In particular, we check structural properties (RDFs, angle-resolved RDFs) and dynamical properties (hydrogen-bond dynamics and rotational dynamics). Here we also report the viscosity of aqueous TMAO solutions as a function of their concentrations and temperatures. Finally section 4.4 is devoted to our conclusions.

4.2 Method

4.2.1 Force field

We developed a new force field by modifying the TMAO force field developed by Kast *et al.*[110] We added three dummy sites (M) around the oxygen atom (O_{TMAO}) of TMAO and assigned a charge of (-0.65 / 3) *e* on each of the dummy sites. Note that the sum of these charges on the three dummy sites amounts -0.65 *e*, the charge on O_{TMAO} in the original Kast model. We used the same formulation for force field as the Kast model

$$U = \sum_{\text{bonds}} \frac{k_b}{2}(b - b_0)^2 + \sum_{\text{angles}} \left[\frac{k_\theta}{2}(\theta - \theta_0)^2 + \frac{k_u}{2}(u - u_0)^2\right] + \sum_{\text{dihedrals}} k_\phi[1 + \cos(n\phi - \delta)] + \sum_{i<j} U_{NB}(r_{ij}). \quad (4.1)$$

The first term describes bond stretching (k_b: force constant, b: bond distance, b_0: equilibrium bond distance), the second term describes angle bending (k_θ: force constant, θ: bend angle, θ_0: equilibrium bend angle) plus the Urey-Bradley term (k_u: force constant, u: distance between the 1, 3 atoms, u_0: equilibrium distance between the 1, 3 atoms), and the third term describes bond torsion (n: multiplicity, k_φ: torsional parameter, φ: dihedral phase, δ: phase shift). The last term describes non-bonded interaction

$$U_{NB}(r_{ij}) = \frac{q_i q_j}{4\pi\epsilon_0 r_{ij}} + 4\varepsilon_{ij}\left[\left(\frac{\sigma_{ij}}{r_{ij}}\right)^{12} - \left(\frac{\sigma_{ij}}{r_{ij}}\right)^{6}\right], \quad (4.2)$$

where the first term describes the Coulomb interaction (q_i: charge, ϵ_0: permittivity of vacuum) between pairs of atoms (i, j) which are separated by r_{ij}, and the second term describes the Lennard-Jones potential (ε_{ij}: well depth, σ_{ij}: contact distance). The Lorentz-Berthelot rule was used to yield the interaction parameters between two different kinds of atoms i and j: $\varepsilon_{ij} = (\varepsilon_i\varepsilon_j)^{1/2}$ and $\sigma_{ij}=(\sigma_i+\sigma_j)/2$. The Lennard-Jones parameters and charges on the atoms of TMAO are identical to the values of the Kast model, expect the values mentioned, as shown in Table 4.1. The bond, angle, and dihedral parameters are shown in Table 4.2. This table includes the equilibrium distance between O_{TMAO} and M, and the N-O-M and M-O-M equilibrium angles, which are set 0.52 Å and 117°, respectively. The equilibrium angle of 117° was taken from the peak position in the O_{TMAO}…D_{D2O} angle-resolved RDF calculated by AIMD simulations using the BLYP/TZV2P level of theory (Ref. [146] and Figure 4.3). The equilibrium distance of 0.52 Å was chosen after optimization with respect to the height of the first peak in the RDF (Figure 4.2) and the hydrogen bond dynamics (Figure 4.4), in reference to the AIMD data, in the range of 0.50-0.60 Å. The dihedral parameters of the force constant, phase, and multiplicity of C-N-O-M were chosen as the same as the parameters of O-N-C-H and of C-N-C-H. As mentioned above, the angles involving dummy site M were taken from

the hydrogen-bond structure around the O_{TMAO} atom that was obtained from AIMD simulations.[146] The mass of the dummy site was set to 400 a.u. (0.2194 u), so that the dummy sites which represent electrons can move faster than the atoms, or nuclei. This value of 400 a.u. has been used as a fictitious mass for electrons in Car-Parrinello MD simulations, for example, of liquid water.[151]

Table 4.1. Lennard-Jones parameters and charges for the current TMAO model. The values followed by * are modified or added in the current force field, while the rest are the same as in the Kast model.[110]

Atom	σ (Å)	ε (kJ/mol)	q (e)
C	3.041	0.2826	-0.26
H	1.775	0.0773	0.11
O	3.266	0.6380	0.00*
N	2.926	0.8362	0.44
M	0.000*	0.0000*	(-0.65)/3*

Table 4.2. Bond, angle, and dihedral parameters for the current TMAO model. The bond (O-M) and angle (M-O-M and N-O-M) parameters are taken large enough that the bond and bend are fixed. The C-N-O-M dihedral parameter is the same as the other dihedral parameters. The values with † are optimized in this study, while those with ‡ are estimated, others are the same as in the Kast model.[110]

Bond parameters

Bond type	Force constant k_b (Å^{-2}·kJ/mol)	Equilibrium length b_0 (Å)
O-N	1431.98	1.407
C-N	1070.79	1.506
C-H	2470.21	1.082
O-M	10000	0.52†

Angle parameters

Angle type	Force constant k_θ (rad^{-2}·kJ/mol)	Equilibrium Angle θ_0 (deg)
O-N-C	254.7	109.99
N-C-H	208.7	108.07
H-C-H	229.5	108.25
C-N-C	576.1	108.16
N-O-M	2500	117†
M-O-M	2500	101†

Dihedral parameters

Dihedral type	Force constant k_ϕ (kJ/mol)	Phase δ (deg)	Multiplicity n
O-N-C-H	1.129	0	3
C-N-C-H	1.129	0	3
C-N-O-M	1.129‡	0‡	3‡

4.2.2 Force field MD

We performed force field molecular dynamics (MD) simulations of aqueous TMAO solution with the current force field model for TMAO. The solution consists of deuterated TMAO (dTMAO) and D_2O. The cell contains 1 dTMAO and 64 D_2O molecules, which yields a TMAO concentration of 0.532 mol/L and a density of 1.109 g/cm^3.[95,114] Periodic boundary conditions are employed. The simulations were performed at temperatures of 300 K and 320 K, using the thermostat of canonical sampling through velocity rescaling,[115] with the CP2K package.[42] After performing 1 ns of equilibration, we ran simulation for 10 ns under each condition, and the trajectories are used for analysis. The time step for integration of the equations of motion was set to 0.1 fs, and the trajectories were recorded every 2.5 fs (25 time steps).

To investigate the dependence of viscosity on TMAO concentration, we performed MD simulations at different concentrations, with the same setup as described above. We investigate TMAO concentrations of 1.025 mol/L (2 dTMAO + 100 D_2O in a (14.797 Å)^3 cell), 1.913 molL (4 dTMAO + 100 D_2O in a (15.143 Å)^3 cell), and 2.690 mol/L (6 dTMAO + 100 D_2O in a (15.474 Å)^3 cell). For calculation of viscosity, five initial configurations were prepared and from each configuration, after 0.5 ns of equilibration, we obtained 2.0 ns of production run (totally 10.0 ns long) used for analysis. The pressure tensors were recorded every 1 fs for calculation of viscosity. Other than the concentrations, we used the same setup as described in the previous paragraph.

4.2.3 Density calculation

As one of the properties for evaluating the validity of a force field, density is a fundamental property. Thus here we investigate the density of TMAO-H_2O solution as a function of TMAO concentration at 298.15 K, which can be compared with experimental data.[110] To this end, we performed molecular dynamics (MD) simulations of TMAO-H_2O systems consisting of 2TMAO-200H_2O, 4TMAO-200H_2O, 8TMAO-200H_2O, and 12TMAO-200H_2O, in the NPT ensemble at 1.01325×10^5 Pa (1 atm) and at 298.15 K. Note that for this analysis of density, we doubled the system size with respect to the simulations used for

calculation of dynamical properties, to make sure that our simulations are free of simulation size effect. The simulated densities are shown in Figure 1. Here for describing water molecules, we used a flexible model (SPC/Fw) and a rigid model (SPC/E[19]). For simplicity, we used the flexible force field models for TMAO for both the cases (SPC/Fw and SPC/E). As a general trend, the SPC/Fw water model yields higher density than experiment, while the SPC/E water model yields density that compares with experimental density.[152] Note that the calculated densities here agree with previous calculations.[152] If we look at the data with the SPC/Fw model, we see that the Shea model yields densities that compare with experimental densities, while the rest of the models provide higher densities than experiment. To see their difference here, we can consider the fact that the Shea model was obtained after modifying the Lennard-Jones parameters of the Kast model. Since density is sensitive to the Lennard-Jones parameters if the charge distributions are similar, it is assumed that the tuning of the Lennard-Jones parameters improve the densities. We assume that the current force field also be improved by tuning their Lennard-Jones parameters,[153] but this is outside of the scope of the current research.

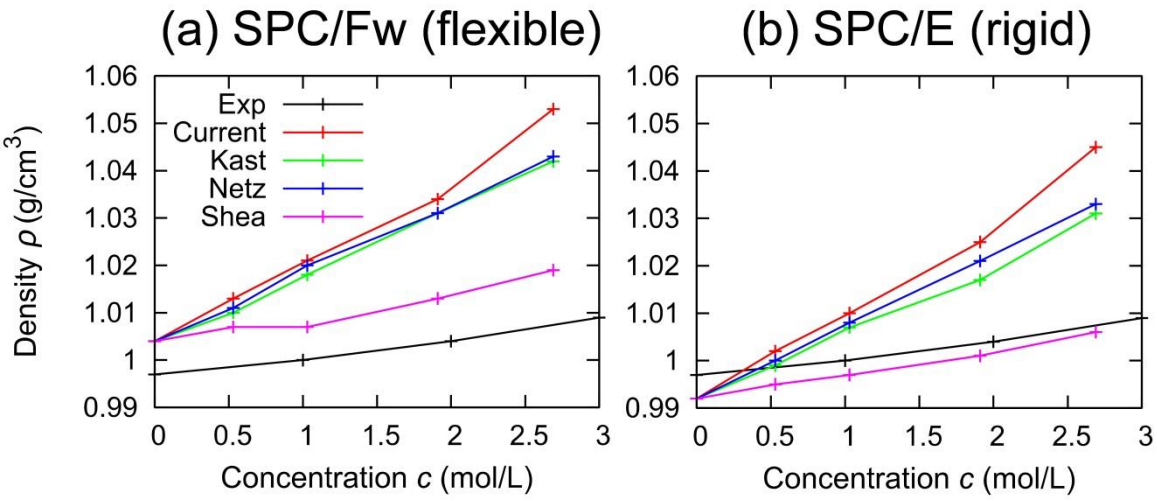

Figure 4.1. Densities of aqueous TMAO solutions as a function of TMAO concentration at a temperature of 298.15 K, using (a) SPC/Fw water model and (b) SPC/E water model. The experimental densities of aqueous TMAO solutions were taken from Ref [110], while the experimental density of pure H_2O was taken from Ref [152].

4.3 Results

4.3.1 Structural properties: RDF and angle-resolved RDF

To check the reliability of the current force field model, we start our discussion with the two structural properties of aqueous TMAO solutions: radial distribution functions (RDFs) and angle-resolved radial distribution functions involving the hydrogen bonds around the hydrophilic O_{TMAO} atom. The RDF of the D atom (D_{D2O}) of D_2O around the O_{TMAO} atom is calculated as

$$g(r) = \frac{1}{4\pi r^2 \Delta r}\frac{V}{N}\langle \Delta N(r) \rangle, \tag{4.3}$$

Where r is the intermolecular distance between O_{TMAO} and D_{D2O}, and $\Delta N(r)$ is the number of D_{D2O} atoms found in the region between r and $r + \Delta r$, that is, in the volume element of the thickness Δr. The calculated RDFs with the current model, the Kast model, the Shea model, and the Netz model are shown in Figure 4.2, together with the RDFs by AIMD simulations from our previous paper.[146] If we compare the first peak heights by the force field MD and by the AIMD simulations, we see that the current force fields provides a peak height that compares with that by BLYP/TZV2P, while the Shea model yields a peak height that compares with that by revPBE/TZV2P.

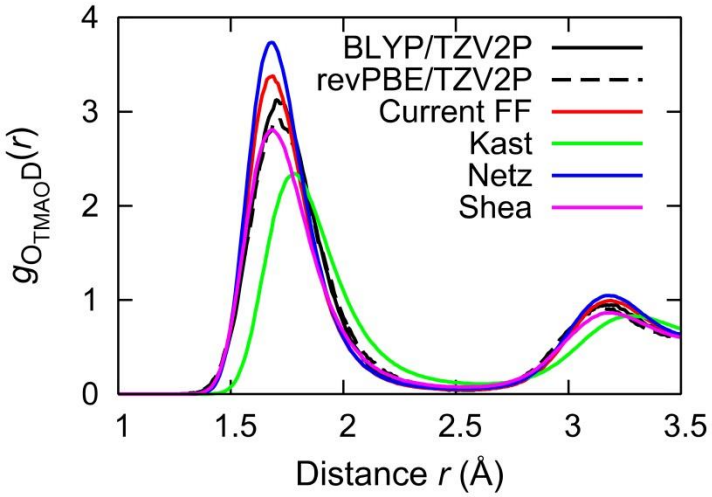

Figure 4.2. RDFs for the 1dTMAO-100D_2O system at 320 K calculated with force field MD (Kast, Netz, and Shea models as well as the current force field model) and AIMD[146] (BLYP/TZV2P and revPBE/TZV2P with Grimm's D3 method for van der Waals corrections[117]). The details of the AIMD simulations are reported Ref. [146].

In addition, we calculated the angle-resolved RDF for each TMAO force field model to investigate the orientational structure of D_{D2O} atoms around O_{TMAO}. The angle-resolved RDF of D_{D2O} around O_{TMAO} can be calculated from

$$g(r,\theta) = \frac{1}{2\pi r \cdot \Delta\cos\theta \cdot \Delta r}\frac{V}{N}\langle \Delta N(r,\cos\theta)\rangle, \tag{4.4}$$

where r is the intermolecular distance between $O_{TMAO}\cdots D_{D2O}$ and θ is the angle formed by the N_{TMAO}-O_{TMAO} group and the $O_{TMAO}\cdots D_{D2O}$ hydrogen bond. $\Delta N(r, \cos\theta)$ is the number of D_{D2O} atoms that are in the volume element of the thickness Δr, around the point (r, $\cos\theta$). Note that the RDF is obtained by integrating $g(r, \theta)$ with respect to θ,

$$g(r) = \int_0^{\pi} g(r,\theta)d\theta. \tag{4.5}$$

The calculated RDFs and angle-resolved RDFs are shown in Figure 3. The figure shows that the height of the first peak obtained by the current force field compares with that by the AIMD simulations, which indicates that the description of the first solvation shell is improved with the current force field compared with the original Kast model. Here we note that the Netz model provides an similarly good description of the angle-resolved RDFs as the current force field, while the Shea model provides the peak height of the angle-resolved RDF that is relatively slightly higher than that by the original Kast model. These figures show that the inclusion of charge directionality involving the $O_{TMAO}\cdots D_{D2O}$ hydrogen bonds in the current force field model leads to the improved structure of the hydrogen bonds.

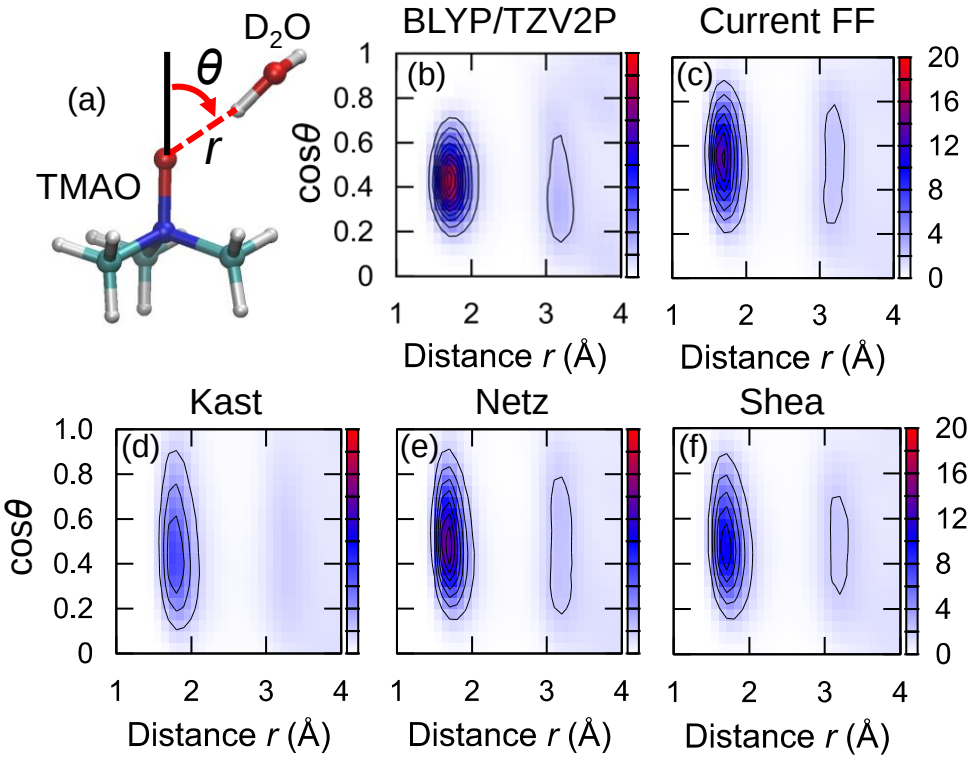

Figure 4.3. (a) A schematic picture for the distance d and angle θ, used for calculation of angle-resolved RDFs, and angle-resolved RDFs for the 1dTMAO-100D_2O system at 320 K

(color code: oxygen=red, nitrogen=blue, carbon=light blue, hydrogen=white) (b) with AIMD using BLYP/TZV2P calculated in our previous paper,[146] (c) with the current force field, (d) with the Kast model, (e) with the Netz model, and (f) with the Shea model.

4.3.2 Dynamical properties: Hydrogen bond dynamics

Next, to test the performance of the current force field in the description of the dynamical aspects of aqueous TMAO solution, we calculated the hydrogen bond dynamics for the hydrogen bond between O_{TMAO} and D_{D2O}. The hydrogen bond dynamics can be quantified through the hydrogen bond formation correlation function[131]

$$p_{HB}(t) = \frac{\langle h(0)h(t)\rangle}{\langle h(0)\rangle} \tag{4.6}$$

where the hydrogen bond formation function, $h(t)$, is 1 then 1.59 Å < $r_{O\cdots D}$ < 2.27 Å,[124,125,154] and otherwise 0. Here $r_{O\cdots D}$ denotes the intermolecular distance between $O_{TMAO}\cdots D_{D2O}$. The calculated time traces for $p_{HB}(t)$ are shown in Figure 4. Among the force field models investigated here, the current force field yields the slowest dynamics for the hydrogen bond which compares with the dynamics by AIMD simulations (BLYP/TZV2P and revPBE/TZV2P). Here it is worth mentioning that this slowed-down dynamics was yielded by the inclusion of the charge directionality in the current force field, which is characterized by the O-M distance and the N-O-M angle. The longer lifetime of the $O_{TMAO}\cdots D_{D2O}$ hydrogen bond may also contribute to the slowdown of the rotational dynamics of the water molecules around O_{TMAO}, which has been suggested in a study on aqueous solutions of tetramethylurea (TMU) and urea.[155]

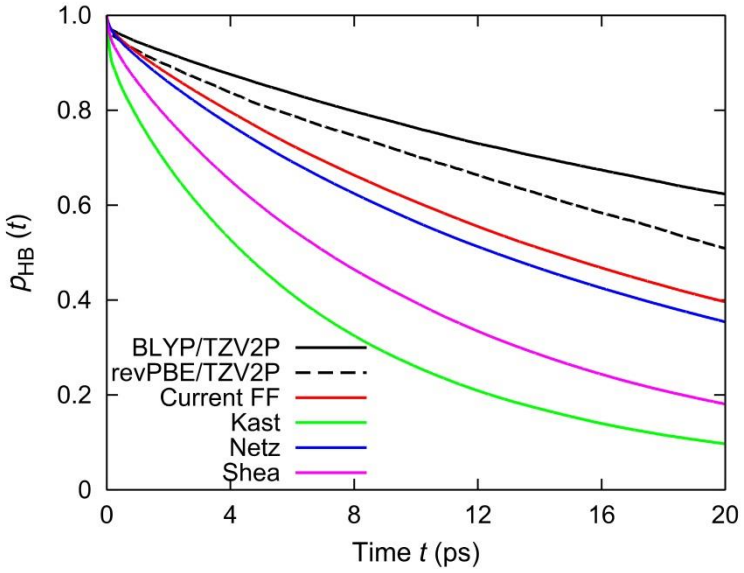

Figure 4.4. The O-D...O_{TMAO} hydrogen bond correlation functions in the aqueous TMAO solution for the 1dTMAO-100D_2O system at 320 K calculated by AIMD (BLYP/TZV2P and revPBE/TZV2P) and force field MD (Kast, Netz, and Shea force field models as well as the currently developed force field model).

4.3.3 Rotational dynamics around TMAO

As another dynamical aspect of aqueous TMAO solution, we also investigated the performance of the current force field in the rotational dynamics of water molecules around O_{TMAO}. Here we compare the data by force field MD with the data by AIMD.[146] The rotational dynamics can be measured by the rotational correlation function, which is experimentally accessible as anisotropy decay. The anisotropy decay of the O-D group can be calculated[130]

$$C_2(t) = \langle P_2 \left(\frac{\boldsymbol{r}_{OD}(t) \cdot \boldsymbol{r}_{OD}(0)}{|\boldsymbol{r}_{OD}(t)||\boldsymbol{r}_{OD}(0)|} \right) \rangle, \quad (4.7)$$

where $\boldsymbol{r}_{OD}(t)$ denotes the O-D vector of the D_2O molecule at time t, $P_2(x) = (1/2)(3x^2 - 1)$ is the second Legendre polynomial, and the brackets ‹···› denote the thermal average. As in our previous work,[146] we consider three sub-ensembles of G1, G2, and G3: G1 consists of O-D groups near the hydrophilic O_{TMAO} atom, G2 consists of O-D groups near the hydrophobic methyl groups, and G3 consists of the rest of the O-D groups. The details of this categorization can be found in Ref [146]. Using the definition of G1, G2, and G3, we can calculate the anisotropy decays for these sub-ensembles with the equation

$$C_{Gi}(t) = \langle P_2 \left(\frac{\boldsymbol{r}_{OD}(t) \cdot \boldsymbol{r}_{OD}(0)}{|\boldsymbol{r}_{OD}(t)||\boldsymbol{r}_{OD}(0)|} \right) \theta_{Gi}(0) \rangle, \quad (4.8)$$

where $\theta_{Gi}(t)$ is a step function with value 1 when the D atom of a given O-D group belongs to G_i at time t, and otherwise 0. $C_{G1}(t)$, $C_{G2}(t)$, and $C_{G3}(t)$ calculated with the force field models are shown in Figure 5, together with the data by the AIMD simulations.[146] Here we provide time constants for the anisotropy decays for G1 and G2, assuming that the decays can be well fit with single exponential decay (Table 4.3). The figure show that the current force field model yields a large difference between the G1 and G2 decays (τ_{G1}/τ_{G2} = 2.3), which compares with the difference by the AIMD simulations (τ_{G1}/τ_{G2} = 2.3 for BLYP/TZV2P and τ_{G1}/τ_{G2} = 3.0 for revPBE/TZV2P), which is not yielded by the original Kast model (τ_{G1}/τ_{G2} = 1.4). Here we note that the Netz model also reproduces a ratio between the time constants for G1 and G2 (τ_{G1}/τ_{G2} = 2.2) that compares with the AIMD value, while the Shea model yields a value of τ_{G1}/τ_{G2} = 1.6 which is close to the value by the Kast model.

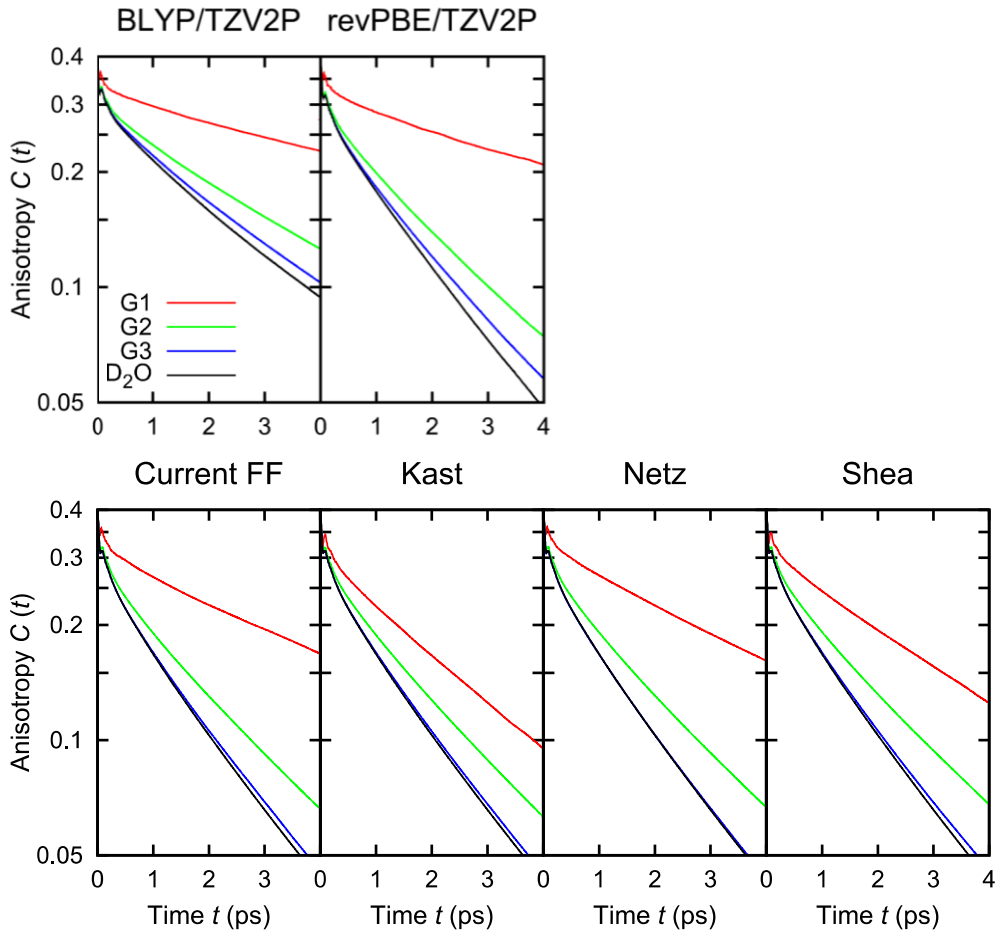

Figure 4.5. Calculated anisotropy decays of the G1 (red), G2 (green), and G3 (blue) O-D groups in the aqueous TMAO solutions for the 1dTMAO-100D_2O system at 320 K. Data are shown calculated with AIMD using BLYP/TZV2P and revPBE/TZV2P with Grimme's D3 method for van der Waals corrections[117] (Data are taken from Ref. [146] Further details can be found there), as well as with force field MD using the model developed in the current study, the Kast model, the Netz model, and the Shea model.

Table 4.3. Time constants τ (ps) of the anisotropy decays for sub-ensembles G1 and G2. The decays were fit with the exponential decay $C(t) = A\exp(-t/\tau)$ for 0.5-3.0 ps.

	BLYP/TZV2P	revPBE/TZV2P	Current FF	Kast	Netz	Shea
τ_{G1}	10	8.5	6.1	3.4	5.7	4.3
τ_{G2}	4.4	2.8	2.6	2.5	2.6	2.7
τ_{G1}/τ_{G2}	2.3	3.0	2.3	1.4	2.2	1.6

4.3.4 Viscosity

Finally, using the current force field model, we calculated the dependence of the viscosity of aqueous TMAO solutions on its concentration. This aims at checking the reliability of the current force field model for investigating aqueous TMAO solutions at high concentration, by comparing the data with experimental viscosity.[69] The $\mu\nu$ component of shear viscosity $\eta_{\mu\nu}$ (μ, ν stand for x, y, or z) can be calculated from equilibrium MD simulations by the Green-Kubo equation[153]

$$\eta_{\mu\nu} = \frac{V}{kT}\int_0^\tau \langle P_{\mu\nu}(t)P_{\mu\nu}(0)\rangle dt, \tag{4.9}$$

where $P_{\mu\nu}(t)$ is the $\mu\nu$ component of the pressure tensor at time t, V is the volume of the system, k is the Boltzmann constant, T is the temperature of the system, and τ is the cutoff time. Using the values $\eta_{\mu\nu}$, the isotropy viscosity can be obtained by averaging the off-diagonal terms, η_{xy}, η_{yz}, and η_{zx}, which is the viscosity which we compare with experimental viscosity. In our calculation, integration was done up to τ = 20 ps. The calculated isotropic shear viscosity is reported as a function of TMAO concentration in Figure 4.6. First, note that the viscosity of 0.765 mPa·s for pure H_2O at 300 K agrees with the value of 0.75 mPa·s reported for SPC/Fw water.[123] The figure shows that the current force field model provides larger viscosity than the Kast model at all the concentrations. By comparing the viscosities by the current force field model, by the Kast model, and by experiment,[95] we can see that the introduction of local partial charges on OTMAO results is a better description of the viscosity of aqueous TMAO solutions at any concentrations. Note that the viscosities calculated by the Netz model and the Shea model also provide this increased viscosity at higher concentrations as a result of their modifications.

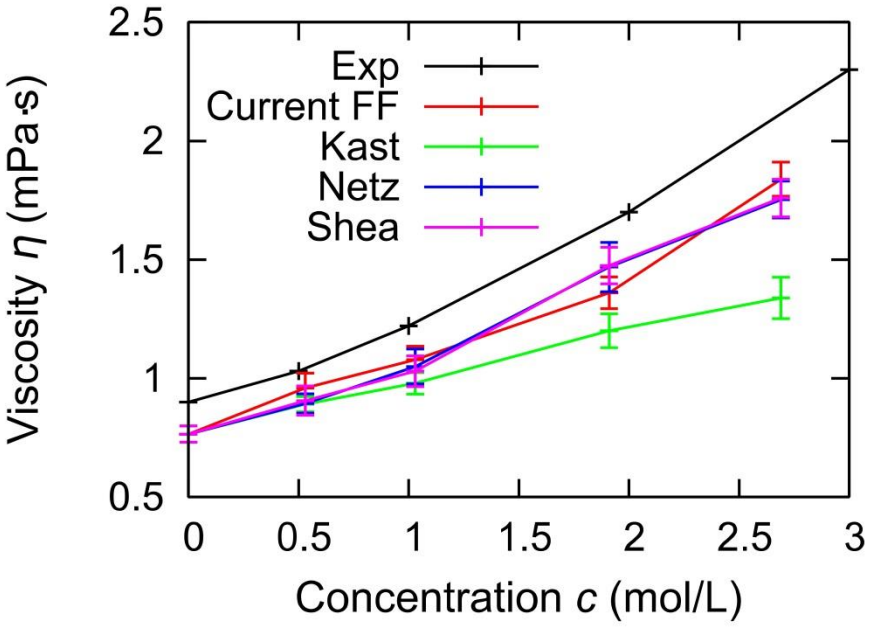

Figure 4.6. Viscosities of TMAO-H_2O solutions at 300 K at concentrations ranging from c = 0.53 mol/L to 2.69 mol/L (red) with the current model, (green) with the Kast model, (blue) with the Netz model, and (pink) with the Shea model. (black) Experimental data for TMAO-H_2O solutions at 296.15 K are taken from Ref [69]. Note that the temperature in the experiment (296.15 K) is ~4 K lower than the temperature in the simulation (300 K).

4.3.5 Comparison of the force field models

In this short section, we would like to summarize the performances of the different force field models for TMAO, which will illustrate their strengths and weaknesses. The Shea model yields density of TMAO-H_2O solutions that best agrees with experiment. Regarding the hydration structure around TMAO, the current model provides a RDF that compares with the data by AIMD using BLYP/TZV2P, while the Shea model provides a RDF that compares with the data by AIMD using revPBE/TZV2P. Calculated angle-resolved RDFs show that the current model and the Netz model provide the highly-directional $O_{TMAO}\cdots D_{D2O}$ hydrogen bonds that are observed by AIMD simulations, though the Netz model employs a point charge on O_{TMAO}. The Netz model results in a coordination number > 3, which however has been improved in the latest development reported in Ref [148]. Here we would like to note that the density provided with the model of Ref [148] is improved with respect to the original Netz model. Regarding the dynamics of $O_{TMAO}\cdots D_{D2O}$ hydrogen bond, the current force field model shows the closest agreement with the AIMD data with slowed dynamics of the first solvation shell around O_{TMAO}. The Netz model also shows slow hydrogen bond dynamics that compare with the AIMD data. Regarding the rotational dynamics of water molecules near O_{TMAO}, the

current model and the Netz model yield slowed-down dynamics compared with the water dynamics near the hydrophobic methyl groups. Finally, the current model, the Netz model, and the Shea model yield better description of viscosity at high TMAO concentration.

4.4 Conclusions

We have developed a new force field for TMAO that provides better description of the hydrogen bond between the O_{TMAO} atom and water molecules. Starting from the model by Kast *et al.*[110] (the Kast model), we introduced three dummy sites around the O_{TMAO} atom to mimic the lone electron pairs on O_{TMAO}, and distributed the original charge of O_{TMAO} onto these dummy sites. This modification aimed at reproducing the highly-directional hydrogen bonds between O_{TMAO} and water molecules which have been found by AIMD simulations.[146] By comparing structural properties involving the hydrogen bonds through RDFs and angle-resolved RDFs, we found that the current force field provides better description of the structural properties that compare with the data by AIMD simulations. Regarding dynamical properties involving the hydrogen bonds by checking the hydrogen bond dynamics and the rotational dynamics of water molecules near the O_{TMAO} atom, the current force field was found to yields better description that are comparable with the AIMD data. In addition, it is found that the current force field provides an increasing behavior of viscosity at high TMAO concentrations, which compare well with experiment. These improved structure, dynamics, and viscosity were gained after the simple modification of the original Kast model through the introduction of dummy sites around the O_{TMAO} atom. These results suggest that the inclusion of the hydrogen bond directionality has a major impact on the structure and dynamics of water molecules involving the hydrogen bonds. This simple procedure of modifying a force field can be used in any MD packages and is compatible with other force field models for biomolecules, paving the way to further investigating the interactions between TMAO and proteins. In particular, accurate description of the N-O group of TMAO can be important for investigating the protein conformational properties, since it has been proposed that the creation of cavity in water hydrogen-bond network as a result of the presence of TMAO affect the process of protein folding.[156]

Chapter 5

Dynamical heterogeneities of Rotational Motion in Room Temperature Ionic Liquids Evidenced by Molecular Dynamics Simulation

Room temperature ionic liquids (RTILs) have been shown to exhibit spatial heterogeneity, or structural heterogeneity in the sense that they form hydrophobic and ionic domains. Yet studies of the relationship between this structural heterogeneity and the ~picosecond motion of the molecular constituents remain limited. In order to obtain insight into the time scales relevant to this structural heterogeneity, we perform molecular dynamics simulations of a series of RTILs. To investigate the relationship between the structures, i.e. the presence of hydrophobic and ionic domains, and the dynamics, we gradually increase the size of the hydrophobic part of the cation from ethylammonium nitrate (EAN), via propylammonium nitrate (PAN), to butylammonium nitrate (BAN). The two ends of the organic cation, namely the charged N_{head}-H group and the hydrophobic C_{tail}-H group, exhibit rotational dynamics on different timescales, evidencing dynamical heterogeneity. The dynamics of N_{head}-H group is slower because of the strong Coulombic interaction with the nitrate counter-ionic anions, while the dynamics of C_{tail}-H group is faster, because of the weaker van der Waals interaction with the surrounding atoms. In particular, the rotation of N_{head}-H group slows down with increasing the cationic chain length, while the rotation of C_{tail}-H group shows little dependence on the cationic chain length, manifesting that the dynamical heterogeneity is enhanced with longer cationic chain. The slowdown of the N_{head}-H group with increasing the cationic chain length is associated to a lower number of nitrate anions near the N_{head}-H group, which presumably results in the increase of the energy barrier for the rotation. The sensitivity of the N_{head}-H rotation to the number of surrounding nitrate anions, in conjunction with the varying number of nitrate anions, gives rise to a broad distribution of N_{head}-H reorientation times. Our results suggest that the asymmetry of the cations and the larger excluded volume for longer cationic chain are important for both the structural heterogeneity and the dynamical heterogeneities. The observed dynamical heterogeneities may affect the rates of chemical

reactions depending on where the reactants are solvated in ionic liquids, and provide an additional guideline for the design of RTILs as solvents.

5.1 Introduction

Despite the great chemical variety for anions and cations that form room temperature ionic liquids (RTILs)[38,157–177] – salts that are liquid at room temperature –, ionic liquids appear to share a common structural motif: On the molecular level scale, ionic liquids are spatially segregated into hydrophobic domains and ionic domains. In 2005, Wang and Voth[37,178,179] have shown by molecular dynamics (MD) simulations that the hydrophobic tail carbon atoms (C_{tail}) of RTILs (1-alkyl-3-methyl-imidazolium nitrate) aggregate with other C_{tail} atoms. This aggregation was observed by their visual observation and higher peak heights for the $C_{tail}\cdots C_{tail}$ radial distribution functions (RDFs). In 2006, Lopes and Pádua also observed the aggregation of tail atoms, and revealed the presence of ionic and hydrophobic domains and long-range nanoscale segregation in RTILs.[180] The formation of ionic and hydrophobic domains has been confirmed by X-ray diffraction[181] and is now regarded an important aspect of RTILs.[173,182–185] For example, it has been suggested that the hydrophobic aggregation affect the chemical reactivity of solutes when RTILs are used as solvents.[172]

There are several studies, which also suggest that the structural heterogeneity also leads to dynamical heterogeneity.[39] Dynamical heterogeneity has been discussed in different contexts and is often assessed by studying – amongst other properties – the translational and rotational motion of RTILs. Differences have been evidenced in the dynamical behavior between cations and anions, between ionic domains and hydrophobic domains, and between given sub-ensemble within RTILs, where, e.g. the dynamics depends on the local environment. The latter type of dynamical heterogeneity is closely related to the behavior of super-cooled liquids.[186–189] The dynamical heterogeneity for RTILs was first mentioned by Voth's group in 2004, prior to their finding of the spatial heterogeneity.[38] In that paper, the authors have calculated the van Hove correlation function of RTILs, showing that the translational (or diffusive) dynamics of each of the constituent ions are heterogeneous (the self-part of the van Hove correlation functions[190] show a non-Gaussian behavior), namely their life time depends on the local environment. In 2004, Ribeiro and coworkers have performed molecular dynamics simulations of RTILs to reveal that the rotational dynamics of each constituent ion are also heterogeneous due to their different microscopic environments. In 2010, Fruchey and Fayer measured the fluorescence anisotropy decay of a probe molecule solvated in different domains (the ionic domains and hydrophobic domains of RTILs), and

found that the rotational dynamics of the probe strongly depends on its location.[39] In 2015, some of the authors of this current paper used femtosecond infrared spectroscopy to find that the thermal relaxations of the stretching vibrations differ for the two ends of cationic chains of alkylammonium nitrates.[191] In 2016, Verma *et al.* have performed multi-dimensional spectroscopy measurement and revealed that there is also a heterogeneity of dynamics involving solvation response.[192] These studies and other studies on the dynamics of RTILs[193–198] suggest that taking the heterogeneity of dynamics into account is needed to yield accurate description of dynamics in RTILs.

This paper aims at investigating two types of dynamical heterogeneities in RTILs. The first dynamical heterogeneity is the difference between the rotational dynamics of the two ends of cationic chains, which form ionic domains and hydrophobic domains, and the second heterogeneity is the difference in the time scales of the rotational dynamics of the charged N_{head}-H groups, which we reveal is a consequence of different surrounding environments as a result of very slow relaxation of the structure of RTILs. To this end, we perform force field molecular dynamics simulations of a series of alkylammonium nitrates: ethylammonium nitrate (EAN), propylammonium nitrate (PAN), and butylammonium nitrate (BAN). The alkylammonium nitrates are simple RTILs and have been investigated[199–202] since the early stage of RTIL research, after they have been reported by P. Walden as early as in 1914.[203] Here, we investigate the structure and dynamics of the two ends of the alkylammonium cations: the N_{head}-H groups and the C_{tail}-H groups. We study the rotational dynamics of these two groups, which are – at least in principle – experimentally accessible by mid-infrared pump-probe spectroscopy.[95,130] To reveal the origin of the two types of dynamical heterogeneities, we perform further analyses of radial distribution functions (RDFs) involving interaction around the two ends of the alkyl chains. Anticipating our results, we find that the rotational dynamics of the two ends of cationic chains occur on different timescales, exhibiting a dynamical heterogeneity, which is enhanced for longer cationic chains, as it also happens for the spatial heterogeneity. To reveal the mechanism behind our observation, we investigate the number of inter-ionic bonds and its relationship with the rotational dynamics of the charged N_{head}-H groups. Additionally, we find that the rotational dynamics of the N_{head}-H groups differ depending on their long-lived, heterogeneous environments.

This paper is organized as follows. In section II, we describe the details of our MD simulations. In section III, we report the dynamics of the two ends of alkylammonium cations by means of rotational correlation functions. Further analyses include the rotational correlation functions of the second-end bonds of cations, the radial distribution functions

(RDFs) involving the two cationic ends, the spatial distribution functions. Finally, in Section IV, we provide our conclusions.

5.2 Methods

5.2.1. MD simulations

We carried out force field molecular dynamics (MD) simulations of ethylammonium nitrate (EAN),[204] propylammonium nitrate (PAN),[185] and butylammonium nitrate (BAN)[185] using the force field developed by Umebayashi and co-workers.[185,204] These force fields were developed starting from *ab initio* calculations at the MP2/cc-pVTZ(-f)/ and HF/6-31G(d) level of theory and their accuracy in describing the structural properties was checked against experimental X-ray diffraction data.[185] We used charges, Lennard-Jones parameters and intramolecular parameters as in ref. [185]. In particular the intramolecular flexibility was taken into account using AMBER force fields[22] for the stretching, bending, and torsional parameters of the series of RTILs, and parameters by Jayaraman *et al.* to describe the stretching and bonding parameters of the nitrate anion. For each system (EAN, PAN, BAN) we considered 48 pairs of ions in each simulation cell. The simulation cells were set to 19.234 Å × 19.234 Å × 19.234 Å (EAN), 20.309 Å × 20.309 Å × 20.309 Å (PAN), and 21.390 Å × 21.390 Å × 21.390 Å (BAN), which correspond to the experimental densities of 1.2109 g/cm^3 (EAN), 1.1620 g/cm^3 (PAN), and 1.1089 g/cm^3 (BAN), respectively, at 298.15 K from Ref [185]. Note that these values are in broad accordance with other reports.[200] In our simulations, periodic boundary conditions were employed. In the simulations of room temperature ionic liquids molecular diffusion is very slow,[182,205] which may cause sampling issues due to aggregation. To circumvent this potential problem, we prepared three sets of initial configurations. The first set of initial configurations was prepared using the package Packmol.[206,207] The second set of initial configurations was prepared after 1 ns of simulations using zero charges on atoms to make the atoms diffusive. The third set of configurations was obtained after another 1 ns of simulations using zero charges on atoms. As discussed below, our results are independent from the initial state. Starting from these initial configurations, we performed *NVT* simulations at 298.15 K using the thermostats of canonical sampling through velocity rescaling,[115] with the CP2K package.[42] After 1 ns of equilibration run, 2 ns of MD trajectories were obtained after each set of initial configurations (totally 6 ns of trajectories for EAN, PAN, and BAN), which were used for our analysis. As shown in the results, such trajectory lengths are sufficient to sample the local rotational dynamics. The time step for integration was set to 0.5 fs, and the trajectories were recorded every 2.5 fs (5 time steps).

5.3 RESULTS

5.3.1 Rotational dynamics of the two ends of the cationic chains

The rotational dynamics can be evaluated by calculating the rotational correlation function of a given chemical bond, which can be directly compared to the anisotropy decay in polarized pump-probe infrared spectroscopy experiments.[95,130,199] The rotational correlation function of a given bond is given by:[130]

$$C_2(t) = \frac{2}{5}\langle P_2\left(\frac{\boldsymbol{r}(t)\cdot\boldsymbol{r}(0)}{|\boldsymbol{r}(t)||\boldsymbol{r}(0)|}\right)\rangle, \quad (5.1)$$

where $\boldsymbol{r}(t)$ denotes the bond vector at time t, $P_2(x)=(1/2)(3x^2-1)$ is the second Legendre polynomial, and the brackets $\langle\ldots\rangle$ denote the thermal average. Here this function is multiplied by 2/5 to make it easy to compare the computational data with experimental anisotropy decays. We calculated the rotational correlation functions of the two ends of cationic chains, namely, for the N_{head}-H group (charged head group) and the C_{tail}-H group (hydrophobic tail group). The calculated rotational correlation functions are shown in Figure 5.1, and the inferred time constants for the decays are reported in Table 5.1. The time constants were obtained by fitting the data with a stretched exponential function, $C(t)=A\exp\{-(t/\tau)^{\beta}\}$, which is often used for analysis of systems exhibiting a distribution of relaxation times, i.e. heterogeneous systems. The fits are also displayed in Figure 1 and the corresponding parameters are listed in Table 5.1. Using the fitting parameters, we calculated the mean relaxation time $\langle\tau\rangle$, which is defined by $\langle\tau\rangle = (\tau/\beta)\Gamma(1/\beta)$ using the gamma function Γ. The mean relaxation times are also displayed in Table 1. These data show that the rotation of the N_{head}-H group is slower than the rotation of the C_{tail}-H groups for all the investigated RTIL, namely EAN, PAN, and BAN. Thus, the rotational dynamics of the two ends of the cations differ, evidencing heterogeneity in the rotational dynamics. By looking at the dependence of the dynamics on the cationic chain length, we see that the N_{head}-H dynamics slows down with increasing length of the cationic chain (from EAN, via PAN to BAN). Conversely, the rotational dynamics of C_{tail}-H (see Fig 5.2) hardly vary with alkyl chain length. The heterogeneity of the rotational dynamics is enhanced with increasing the cationic chain length, in the sense that the ratio between the time constants ($\tau_{Nhead\text{-}H}/\tau_{Ctail\text{-}H}$) is increasing with increasing cationic chain length.

The observation that the computational data can be described well by a stretched exponential suggests that the dynamics of each end of the cationic chain could be associated with a distribution of rotational time scales, depending on the local environment of each

cation. Such structural heterogeneity is in line with previous studies[37,38] and has also been observed in super-cooled liquids.[186–188] Since the beta values reported here are somewhat similar for all studied RTILs and it is hard to deduce the origin for this heterogeneity, we will take a closer look at this dynamical heterogeneity below by virtue of MD simulations.

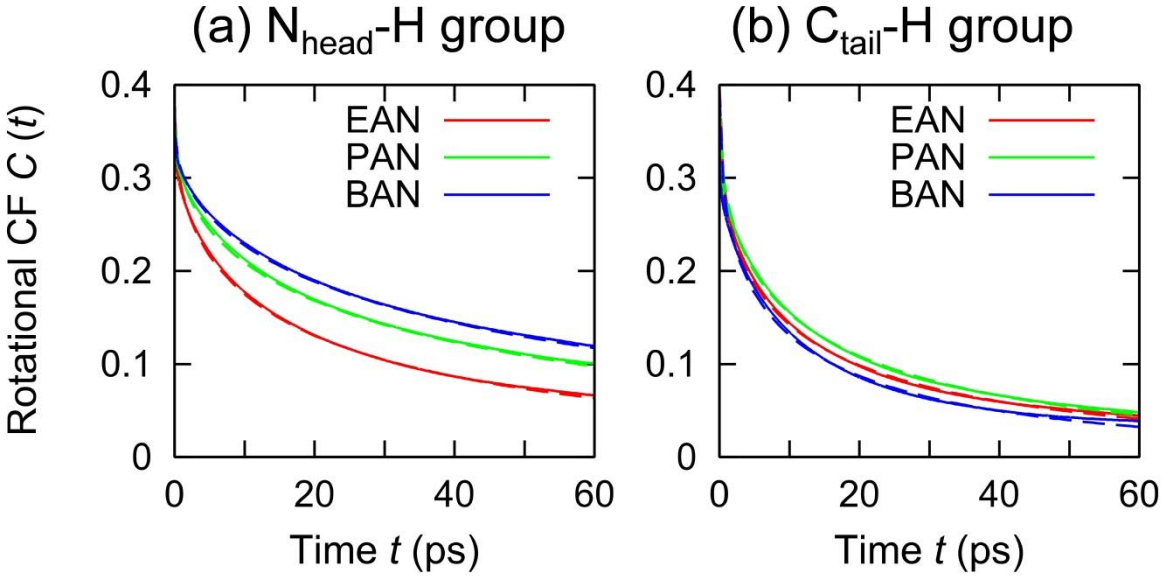

Figure 5.1. (a) N_{head}-H rotational correlation functions and (b) C_{tail}-H rotational correlation functions for ethylammonium nitrate (EAN; red), propylammonium nitrate (PAN; green), and butylammonium nitrate (BAN; blue) at 298.15 K. The dashed lines denote the fitting functions $C(t)=A\exp\{-(t/\tau)^{\beta}\}$ with the parameters shown in Table 5.1.

Table 5.1. Fitting parameters for the N_{head}-H rotational correlation functions and C_{tail}-H rotational correlation functions. The decays were fit with the stretched exponential decay $C(t) = A\exp\{-(t/\tau)^{\beta}\}$ at times ranging from 1 to 60 ps.

	N_{head}-H				C_{tail}-H			
	A	β	τ (ps)	$\langle\tau\rangle$ (ps)	A	β	τ (ps)	$\langle\tau\rangle$ (ps)
EAN	0.37	0.48	18.4	39.8	0.40	0.44	9.3	24.3
PAN	0.36	0.49	34.9	72.5	0.38	0.48	12.5	27.0
BAN	0.35	0.52	50.5	101.0	0.39	0.46	8.3	19.6

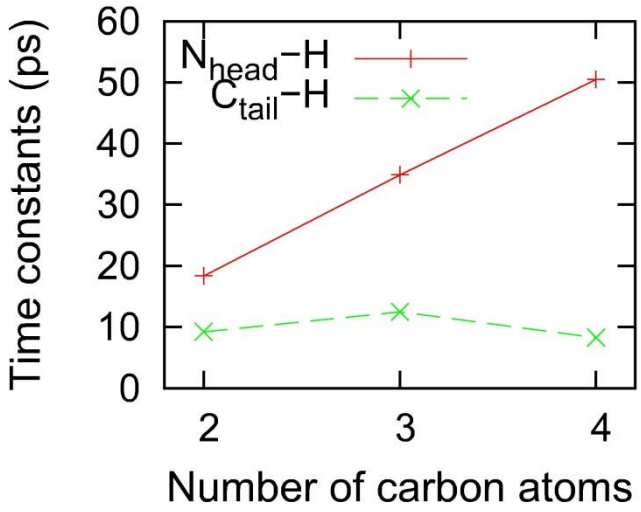

Figure 5.3. Time constants (ps) associated with the reorientation of the N_{head}-H group (red) and the C_{tail}-H group (green) as a function of the number of carbon atoms.

In order to explore the origin of the different time scales for the dynamics of the two terminal groups of the cations, we also studied the rotational dynamics of the adjacent bonds, namely, the N_{head}-C group and C_{tail}-C group. The calculated rotational correlation functions of these adjacent bonds are shown in Figure 5.2. The figure shows that the rotational correlation functions of the N_{head}-C groups and C_{tail}-C group are substantially slower than that of the C_{tail}-H and N_{head}-H groups. This can be rationalized by the fact that a full loss of the orientational correlation for the N_{head}-C and C_{tail}-C rotation requires the rotation of the whole molecule, which is not required for the N_{head}-H and C_{tail}-H groups, as a propeller-like rotation around the N_{head}-C (or C_{tail}-C) axis can largely scramble the orientational correlation for the N_{head}-H (C_{tail}-H) groups. Thus, we can conclude that the N_{head}-H (C_{tail}-H) rotations are predominantly governed by a local propeller-like motion, which is one contribution to the previously reported "rattling" of ions in a long-lived cage of the network of RTILs.[38] We can assume that the difference between the N_{head}-H and C_{tail}-H rotations stems from different intermolecular interactions, because the intramolecular interactions are similar by the force field, and especially the torsional parameters involving N_{head}-H and C_{tail}-H are identical.

An obvious origin of the difference between the N_{head}-H and C_{tail}-H groups is the charge asymmetry of the cations. The N_{head}-H groups are positively charged (0.57*e* by the force field models) and have strong Coulombic interaction with negatively charged nitrate anions, while the C_{tail}-H groups have zero charge (exactly zero by the force field models) and only weak van der Waals interactions with the surrounding atoms. Thus, strong Coulombic interaction naturally slows down the rotational dynamics of the N_{head}-H groups, while this kind of slow-

down effect is not present for the C_{tail}-H groups. In fact, this asymmetry of the cations is considered the factor of the aggregation of hydrophobic chains of RTILs or spatial heterogeneity.[37,38]

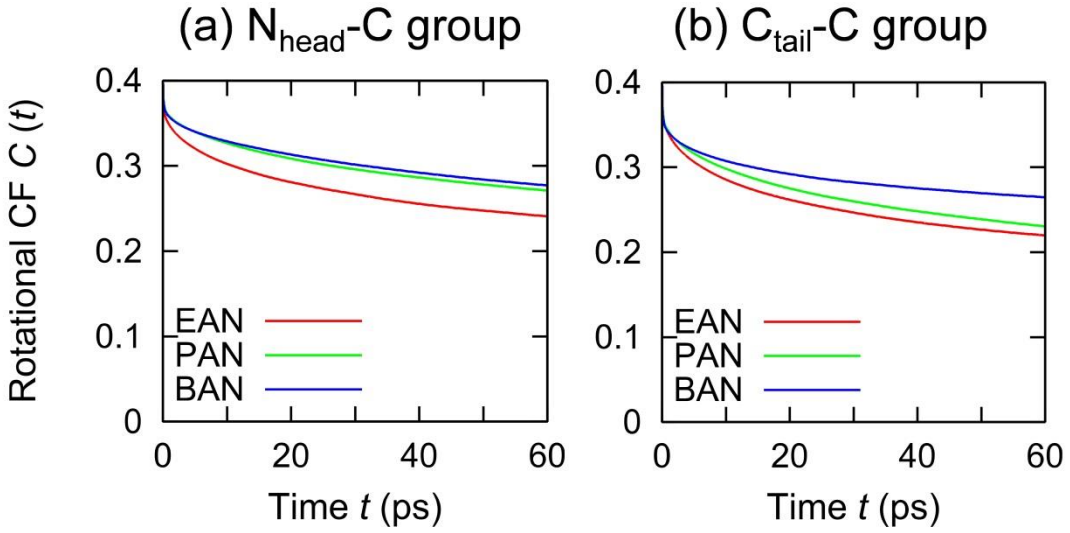

Figure 5.2. (a) N_{head}-C rotational correlation functions and (b) C_{tail}-C rotational correlation functions for ethylammonium nitrate (EAN; red), propylammonium nitrate (PAN; green), and butylammonium nitrate (BAN; blue) at 298.15 K.

5.3.2 Inter-ionic structure involving N_{head}-H

To obtain deeper insight into the effect of Coulombic interactions on the slow-down of the rotational dynamics of the N_{head}-H groups with increasing cation length, we investigate the structure of atoms around the cationic group, by calculating the radial distribution functions (RDFs) for relevant pairs of atoms, according to

$$g(r) = \frac{1}{4\pi r^2 \Delta r}\frac{V}{N}\langle \Delta N(r) \rangle, \tag{5.2}$$

where r is the distance between the pair of two given atoms. V is the volume of the simulation cell, and $\Delta N(r)$ is the number of atoms found in the region between r and $r + \Delta r$, from the reference atom. The brackets $\langle \ldots \rangle$ denote the thermal average. From the RDFs, the number of atoms within the distance of r_c, which is denoted n, can be obtained as:

$$n = 4\pi \int_0^{r_c} r^2 g(r) \times \left(\frac{N}{V}\right) dr, \tag{5.3}$$

where r_c is the cutoff value for integration of $g(r)$. Note that the cutoff value r_c can be defined as the first minimum for disordered systems generally when calculating the first coordination numbers, but due to the somewhat blurred first minima in the figures shown below, we will

set the cutoff r_c to the distance where the peak appears diminished (defined by visual inspection).

From the calculated RDFs for the pairs of N_{head}…N_{anion}, we extract the number of nitrate anions around the N_{head}-H group as a function of the cationic chain length. Therefore we report the RDFs $g(r)$ multiplied by the number densities N/V in Figure 5.4, or in other words the number density weighted RDFs, which vary for different cationic chain lengths. Integrating the functions in Figure 5.4 up to the cutoff distance, and multiplying the result by $4\pi r^2$, we directly obtain the number of relevant atoms within the cutoff distance. Here we calculated the number of nitrate anions up to the distance of 5.0 Å, where the peak in $g(r)$ is diminished. The calculated numbers are shown in Table 5.2.

The figure and the table show that the number of nitrate anions decreases with increasing the cationic chain length. This can be explained by the larger excluded volume of longer cationic chains, allowing fewer nitrate ions near the N_{head}-H group. The reduced number of nitrate anions in the vicinity of the cationic head group may lead to more directional hydrogen-bonds, which slows down the rotational dynamics of the N_{head}-H group, as we will demonstrate below.

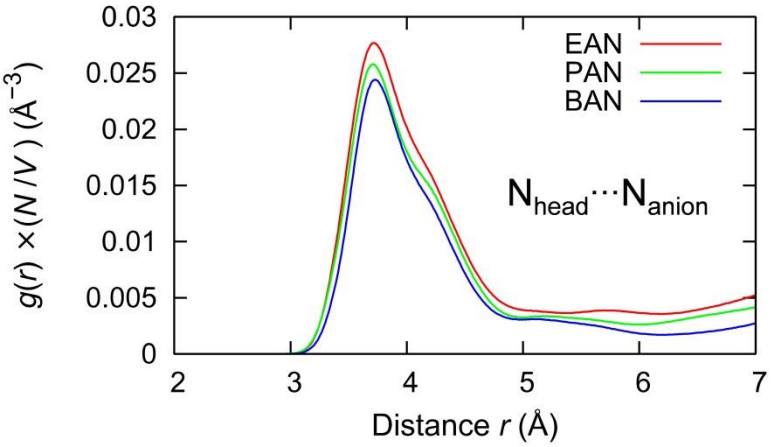

Figure 5.4. Number density weighted radial distribution functions ($g(r)$ multiplied by number densities N/V) for the pair of N_{head}···N_{anion} calculated for ethylammonium nitrate (EAN; red), propylammonium nitrate (PAN; green), and butylammonium nitrate (BAN; blue) at 298.15 K.

Table 5.2. The numbers of nitrate anions around the N_{head}-H groups, and the numbers of C_{tail} atoms around the reference C_{tail} atom for the series of alkylammonium nitrates.

	$N_{head}\cdots N_{anion}$	$C_{tail}\cdots C_{tail}$
	Number of nitrate anions N	Number of C_{tail} atoms N
EAN	4.94	2.81
PAN	4.43	2.58
BAN	4.05	2.66

The figure and the table show that the number of nitrate anions decreases with increasing the cationic chain length. This can be explained by the larger excluded volume of longer cationic chains, allowing fewer nitrate ions near the N_{head}-H group. The reduced number of nitrate anions in the vicinity of the cationic head group may lead to more directional hydrogen-bonds, which slows down the rotational dynamics of the N_{head}-H group, as we will demonstrate below.

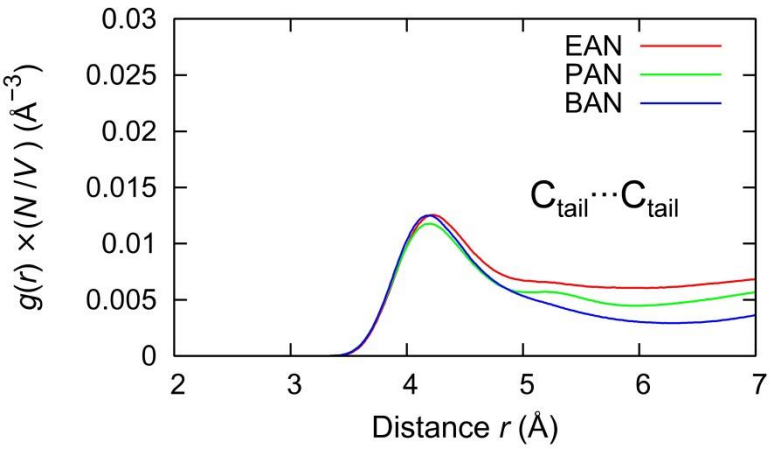

Figure 5.5. Number density weighted radial distribution functions ($g(r)$ multiplied by number densities N/V) for the pair of $C_{tail}\cdots C_{tail}$ calculated for ethylammonium nitrate (EAN; red), propylammonium nitrate (PAN; green), and butylammonium nitrate (BAN; blue) at 298.15 K.

5.3.3 Effect of the number of inter-ionic bonds on rotational dynamics

We now investigate the effect of the number of inter-ionic bonds on the rotational dynamics of the N_{head}-H groups. To this end, we calculated the rotational correlation functions (Eq. 5.1) for different number of inter-ionic $N_{head}\cdots N_{anion}$ bonds, which is denoted N_{IB}. Here the number of inter-ionic bonds is considered only at t = 0: we calculated the rotational correlation functions for the N_{head}-H groups such that the number of the inter-ionic $N_{head}\cdots N_{anion}$ bonds (N_{IB}) is 3, 4, 5, and 6 at time t = 0. The calculated rotational correlation

functions for N_{IB} = 3, 4, 5, and 6 are shown in Figure 5.6. The results show that a reduced number of the inter-ionic bonds yields slower dynamics for the N_{head}-H rotation for all the cases of EAN, PAN, and BAN. Hence, a reduced number of inter-ionic bonds can be clearly related to slowed-down rotational dynamics of the N_{head}-H group.

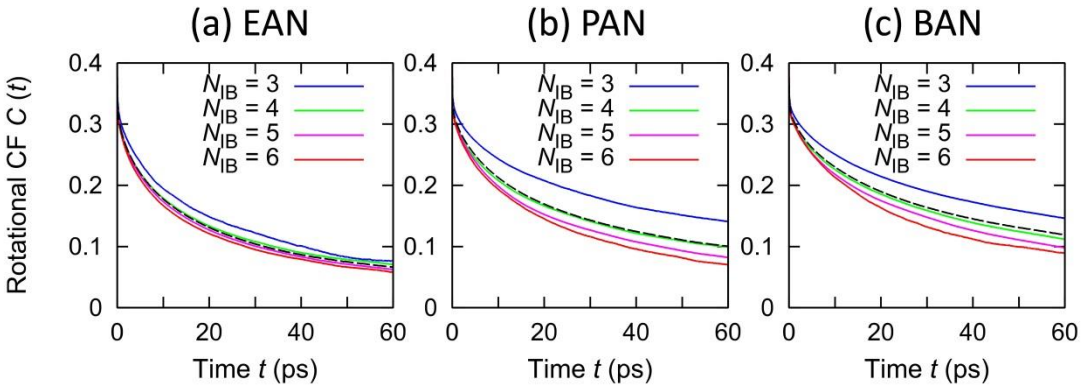

Figure 5.6. N_{head}-H rotational correlation functions for different number of the inter-ionic N_{head}···N_{anion} bonds (N_{IB} = 3 (blue), 4 (green), 5 (pink), and 6 (red)) for (a) ethylammonium nitrate (EAN), (b) propylammonium nitrate (PAN), and (c) butylammonium nitrate (BAN) at 298.15 K. The dashed black lines denote the original rotational correlation functions shown in Figure 1(a).

5.3.4 Mechanism behind slower dynamics for lower number of inter-ionic bonds

To explore the molecular-level origin of the correlation between the inter-ionic bond numbers and the N_{head}-H rotation, we calculated spatial distribution functions (SDFs)[208] for the pair of N_{head}···N_{anion}. The SDF for the pair of N_{head}···N_{anion} can be calculated through:

$$s(r,\theta,\phi) = \frac{1}{r^2 \sin\theta \cdot \Delta r \Delta\theta \Delta\phi} \frac{V}{N} \langle \Delta N(r,\theta,\phi) \rangle, \quad (5.4)$$

where r is the distance between the pair of N_{head}···N_{anion}, θ is the angle between the vectors C-N_{head} and N_{head}···N_{anion}, ϕ is the angle between the projected vectors N_{head}-H and N_{head}···N_{anion} onto the plane perpendicular to the C-N_{head} vector. For determining the angle ϕ, we chose one of the three N_{head}-H groups. The schematic pictures for defining these angles are provided in Figure 5.7. V is the volume of the simulation cell, and $\Delta N(r, \theta, \phi)$ is the number of the N_{anion} atoms found in the volume element $\Delta V = r^2 \sin\theta \Delta r \Delta\theta \Delta\phi$, from the reference atom N_{head}. The brackets $\langle \ldots \rangle$ denote the thermal average. To see the spatial distribution with respect to the angles, θ and ϕ, we focused on the following two types of radial distribution functions,

$$g_{\text{polar}}(r,\phi) = \frac{1}{2} \int_0^{\pi} s(r,\theta,\phi) \sin\theta \, d\theta, \quad (5.5)$$

$$g_{\text{azimuthal}}(r,\theta) = \frac{1}{2\pi}\int_0^{2\pi} s(r,\theta,\phi)d\phi, \quad (5.6)$$

by integrating the spatial distribution function with respect to ϕ and θ in order to obtain spatial distribution with respect to the azimuthal angle θ and polar angle ϕ, respectively. Note that the RDF can be obtained from:

$$g(r) = \frac{1}{4\pi}\int_0^{2\pi} d\phi \int_0^{\pi} s(r,\theta,\phi)\sin\theta\, d\theta\,. \quad (5.7)$$

We calculated these distributions for BAN with different number of the inter-ionic $N_{head}\cdots N_{anion}$ bonds, which are shown in Figure 5.8 and 5.9. Figure 5.8 shows that there are peaks around $\phi \approx 60°$, 180° for all the cases, consistent with C_{3v} symmetry. This means that nitrate anions are predominantly found at these angles, which are not in the direction of N_{head}-H group from the N_{head} atom. We suppose that this is because of the intrinsic nature of force field models that, in general, do not take the structural directionality into account. Indeed, an AIMD study of methylammonium nitrate reports that the centers of mass of the nitrate anions are located at $\phi \approx 0°$, 120°.[168] However, regardless of the directionality of the inter-ionic bonds, we can conclude that, when the inter-ionic bond number is increased, the distribution of nitrate anions widens, which reduces the energy barrier for the rotation of the N_{head}-H group.

The azimuthal distribution of nitrate anions in Figure 5.9 shows that there are peaks at around $\theta \approx 0°$, 90°, which are more pronounced for the cases of N_{IB} = 4, 5, and 6. This means that when more nitrate anions come close to the N_{head} atom, the average bond length of the inter-ionic $N_{head}\cdots N_{anion}$ bonds gets longer, resulting in less hindrance for the N_{head}-H group imposed by the surrounding nitrate anions.

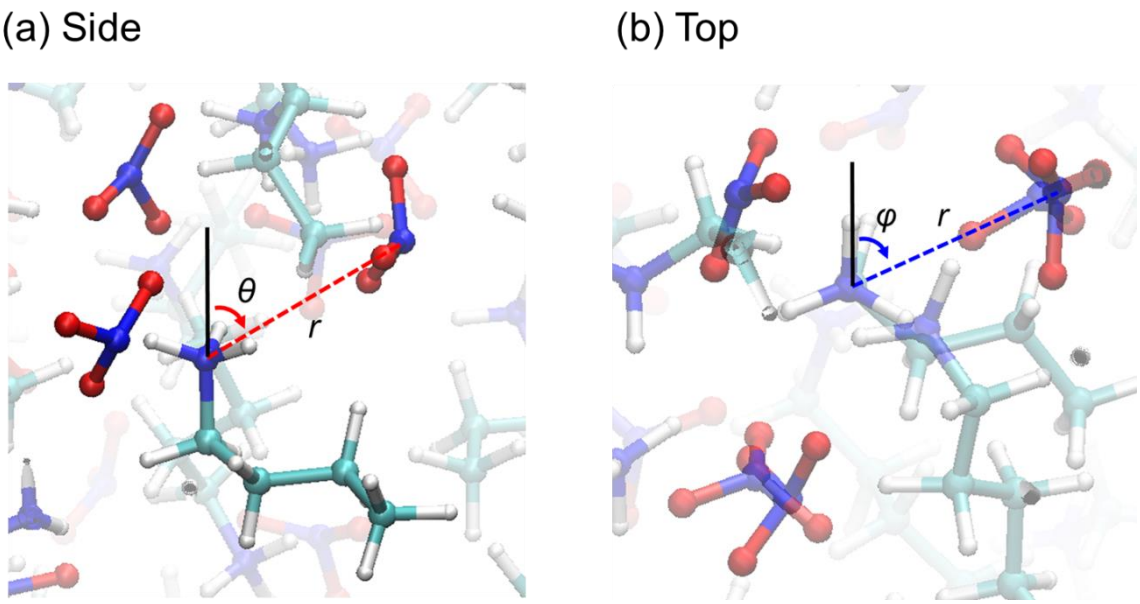

Figure 5.7. Schematic pictures for definitions of the angles θ and ϕ. (a) Side view showing the definition of the angle θ. (b) Top view showing the definition of the angle ϕ.

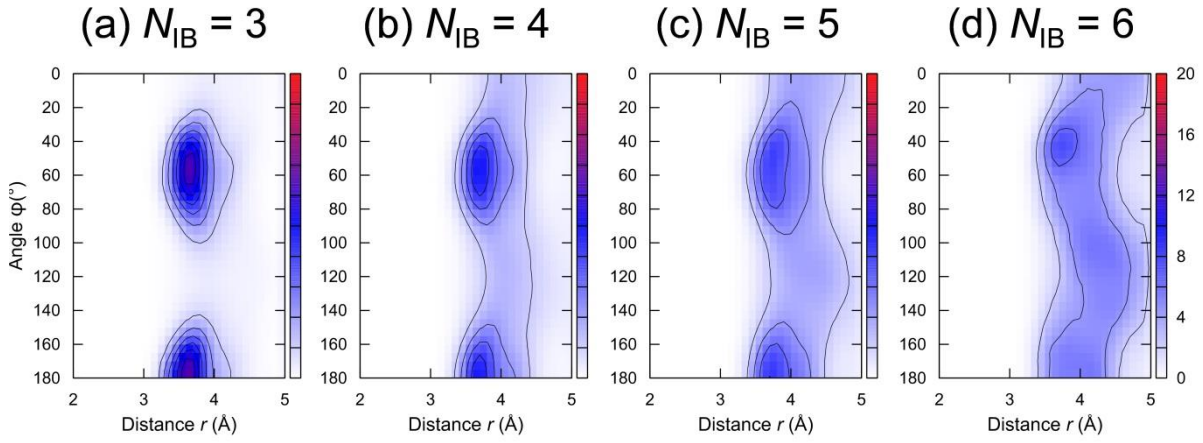

Figure 5.8. Polar distribution function $g_{polar}(r, \phi)$ for butylammonium nitrate (BAN) at 298.15 K for different number of the inter-ionic $N_{head}\cdots N_{anion}$ bonds (N_{IB} = 3, 4, 5, and 6).

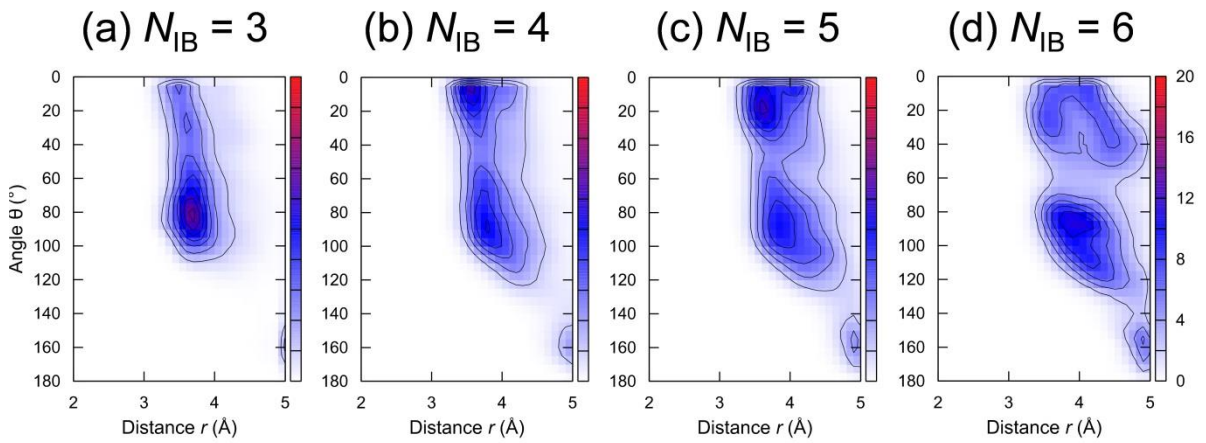

Figure 5.9. Azimuthal distribution function $g_{azimuthal}(r, \theta)$ for butylammonium nitrate (BAN) at 298.15 K for different number of the inter-ionic $N_{head}\cdots N_{anion}$ bonds (N_{IB} = 3, 4, 5, and 6).

We would like to comment here that such correlation between higher number of inter-ionic $N_{head}\cdots N_{anion}$ bonds and faster rotational dynamics of N_{head}-H groups is analogous to what has been concluded for water reorientation. For water reorientation, it has been suggested that over-coordinated water molecules can rotate more easily due to the decreased energy barrier for rotation as a result of the extra molecule.[209] This kind of over-coordinated state triggers water reorientation, which, as a result, is characterized by a series of discrete jumps, rather than continuous, diffusive motion .[103,104]

5.3.5 Comparison with RTIL literature

Finally, we would like to compare our simulation data with experimental data[191,210–212] and *ab initio* MD simulation data.[168] In Ref. [199], some of us investigated the rotational dynamics of the N_{head}-H group using femtosecond-infrared spectroscopy. As detailed in Ref 40, deconvolution of contributions of molecular rotation and thermal diffusion to the anisotropy decay yielded a (single exponential) molecular rotation time of ~80 ps for the N_{head}-D rotation at 25 C° (298 K). This time scale is slower than the time constant from our simulation (18.4 ps). While the isotope difference between the N_{head}-D rotation in the experiment and the N_{head}-H rotation in the simulation may account for a minor part of this discrepancy, the difference presumably stems from the fact that the experimental anisotropy decays are dominated by thermal effects at early times and the experiments have little sensitivity to fast rotational dynamics. In view of the pronounced stretched exponential rotational correlation function of the present study, the difference between experiment and simulation can therefore be rationalized by the experimental sensitivity towards slow

dynamics, that are contained in the broad distribution of relaxation times within the stretched exponentials of the present study.

Finally, we would like to compare our data with an AIMD simulation study of methylammonium nitrate.[168] Although the rotational dynamics was not addressed in Ref. [168] - presumably due to limited sampling time available in AIMD – we will compare other available data. In particular, in Ref. [168], the lifetime for the ion-paring of cations and anions was investigated, showing that about 85 % of the ion pairs remain connected after 14.5 ps. The lifetime for the ion-paring obtained with AIMD seems shorter than that obtained by our force field MD simulations by visual inspection. Since the inter-ionic interaction is found to play an important role in the dynamical heterogeneities and their dependence on the cationic chain length it may be not surprising that AIMD provides somewhat different results also for the rotational dynamics. Additional investigations using AIMD is thus certainly desirable.

5.4 Conclusion

We have reported molecular dynamics simulations of a series of RTILs including ethylammonium nitrate (EAN), propylammonium nitrate (PAN), and butylammonium nitrate (BAN) to investigate the dynamical heterogeneity and its relationship with the aggregation of tail C_{tail} carbon atoms, or structural heterogeneity.[37] The rotational dynamics of the two ends of the cations, namely the N_{head}-H group and the C_{tail}-H group of the alkylammonium ions, were investigated by their rotational correlation functions. These data show that the two ends have different timescales for rotational dynamics, governed by a local propeller-like motion where the dynamical heterogeneity originates from the asymmetry of the cationic chain. The charged N_{head}-H group strongly interacts with the negatively charged anions, resulting in slower N_{head}-H dynamics, while the hydrophobic C_{tail}-H group lacks strong Coulombic interaction, and is therefore able to reorient relatively quickly.

We also observed that the dynamics of the charged N_{head}-H group slow down with increasing cationic chain length, in other words, the dynamical heterogeneity is enhanced by longer cationic chain. We found that the slower dynamics for the longer chains is the result of a smaller number of inter-ionic bonds exhibiting higher directionality. A closer investigation of the local structure of the $N_{head}\cdots N_{anion}$ bonds revealed that three nitrate anions hinder the rotation of the rotation of the N_{head}-H groups while an increased number of nitrates allows for a faster rotation of the N_{head}-H groups. Accordingly, the rotational dynamics of the N_{head}-H

groups exhibits a distribution of rotational time scales as a result of varying numbers of surrounding nitrate anions.

Our study shows that, in addition to spatial heterogeneity, there are dynamical heterogeneities involving rotational dynamics. Since the dynamics of solvent molecules affect the reaction rates of solutes, our results imply that the size of hydrophobic chain of RTILs may not only affect the location (i.e. solvation) of solutes within spatially heterogeneous RTILs, but also their reactivity due to the RTILs heterogeneous dynamics.

Chapter 6
Conclusions

In my PhD research, I have investigated two types of systems, i.e., aqueous trimethylamine *N*-oxide (TMAO) solution and room temperature ionic liquids (RTILs) using molecular dynamics (MD) simulations, to reveal molecular-level mechanisms for experimentally observed phenomena.

My first project was dedicated to investigate the rotational dynamics of water molecules in aqueous TMAO solutions, and mechanisms behind the experimentally observed slow-down of the rotational dynamics of water. Using *ab initio* MD (AIMD) simulations, which is a reliable MD method based on electronic structure theory, I have revealed that water rotation is strongly slowed down near the hydrophilic oxygen atom (O_{TMAO}) of TMAO, while water rotation is found to be only moderately slowed down near the hydrophobic methyl groups of TMAO molecules. Further analyses of hydrogen-bond dynamics and spatial distribution of the hydrogen bonds between TMAO and water molecules, revealed that the strongly slowed-down dynamics for water rotation near O_{TMAO} is the result of the hydrogen bonds between TMAO and water, which are long-lived and highly-directional. Furthermore, I have suggested two mechanisms behind the water rotation near the O_{TMAO} atom, which corroborated the mechanism that the long-lived and highly-directional hydrogen bond significantly affects the dynamics of water molecules hydrogen-bonded to the TMAO molecule. This AIMD project has provided a reference data set by reliable AIMD simulations on the water dynamics around amphiphilic molecules, which have been discussed controversially both in experimental and theoretical studies. Additionally, my findings here imply that the action of TMAO as osmolyte is enhanced by the strong hydrogen bond between TMAO and water, which enlarges the “net” volume of TMAO.

My second project was aimed at developing a reliable force field model for TMAO, which is indispensable for running inexpensive simulations of biologically interesting systems. This was done by modifying an existing force field model for TMAO: Dummy sites were added around the hydrophilic O_{TMAO} atom to include the charge directionality, which was observed by the AIMD simulations. The modified force field model was found to better describe the hydrogen bonds between TMAO and water, in the sense that the data more

closely resemble data obtained from AIMD simulations. It was found that this modified force field model yields overestimated density for aqueous TMAO solutions, but this shortcoming can likely be lifted by tuning the force field parameters. This project showed that introducing dummy sites to reproduce directional hydrogen bonds, which are widely found in biologically interesting molecules, is an efficient approach to reproduce such directional interactions. Therefore, the developed force-field for TMAO is expected to improve MD simulations of large biomolecules such as proteins or drugs.

My third project focused on room temperature ionic liquids (RTILs), which have the potential to be used as new and green solvents. One important aspect of RTILs is that they have heterogeneous structure, characterized by formation of ionic and hydrophobic domains. However, the dynamics of the constituent ions in RTILs, which is a fundamental property that determines macroscopic properties, was not well understood. To investigate the dynamics in RTILs, I have performed force field MD simulations of a series of alkylammonium nitrates, which revealed that the two ends of cationic chain rotate on different timescales: The charged N_{head}-H group rotates slowly as a result of strong Coulombic interaction with counter-ions, while the hydrophobic C_{tail}-H groups rotate faster as strong interactions are absent. In this sense, the dynamics in RTILs are heterogeneous, resembling the structural heterogeneity. The difference between the rotational timescales of the two ends was found to increase when the cationic chain length is increased, which originates from the decreased number of counter-ions around the N_{head}-H group. This project also revealed that the rotational timescales of N_{head}-H groups are widely distributed as a result of the structural heterogeneity. This microscopic investigation of RTILs provided new insight into the dynamics of RTILs, which will be useful to understand reactivity and solubility in ionic liquids and thus help choosing RTILs for specific applications.

The main purpose of the projects, which I have presented in my thesis, has been to investigate the structure and dynamics of complex molecular systems, where strong, specific intermolecular interactions are responsible for structural and dynamical heterogeneity. My worked has contributed, on one side, to unravel the molecular mechanism behind the experimental observations, in particular time resolved vibrational spectroscopy, on the other side to develop new, accurate force fields. These new developments will permit to accurately investigate larger size systems and longer time scales, extending the predictive power of molecular dynamics simulations.

Acknowledgment

Bibliography

(1) Alder, B. J.; Wainbright, T. E. Phase Transition for a Hard Sphere System. *J. Chem. Phys.* **1957**, *27*, 1208.

(2) Okazaki, S.; Yoshii, N. *The Basis of Computer Simulation*; Kagaku-dojin: Kyoto, Japan, 2011.

(3) Bergsma, J.; Gertner, B. J.; Wilson, K. R.; Hynes, J. T. Molecular Dynamics of a Model SN2 Reaction in Water. *J. Chem. Phys.* **1987**, *86*, 1356–1376.

(4) Lagos, M. J.; Trügler, A.; Hohenester, U.; Batson, P. E. Mapping Vibrational Surface and Bulk Modes in a Single Nanocube. *Nature* **2017**, *543*, 529–532.

(5) Jeon, M. Y.; Al., E. Ultra-Selective High-Flux Membranes from Directly Synthesized Zeolite Nanosheets. *Nature* **2017**, *543*, 690–694.

(6) Pulido, A.; Chen, L.; Kaczorowski, T.; Holden, D.; Little, M. A.; Chong, S. Y.; Slater, B. J.; McMahon, D. P.; Bonillo, B.; Stackhouse, C. J.; et al. Functional Materials Discovery Using Energy–structure–function Maps. *Nature* **2017**, *543*, 657–664.

(7) Yeom, B.; Sain, T.; Lacevic, N.; Bukharina, D.; Cha, S.-H.; Waas, A. M.; Arruda, E. M.; Kotov, N. A. Abiotic Tooth Enamel. *Nature* **2017**, *543*, 95–98.

(8) Kuntz, I. D. Structure-Based Strategies for Drug Design and Discovery. *Science* **1992**, *257*, 1078–1082.

(9) Rajan, K. Materials Informatics. *Mater. Today* **2005**, *8*, 38–45.

(10) Dodd, M. S.; Papineau, D.; Grenne, T.; Slack, J. F.; Rittner, M.; Pirajno, F.; O'Neil, J.; Little, C. T. S. Evidence for Early Life in Earth's Oldest Hydrothermal Vent Precipitates. *Nature* **2017**, *543*, 60–64.

(11) Yancey, P. H. Organic Osmolytes as Compatible, Metabolic and Counteracting Cytoprotectants in High Osmolarity and Other Stresses. *J. Exp. Biol.* **2005**, *208*, 2819–2830.

(12) Tang, W. H. W.; Wang, Z.; Kennedy, D. J.; Wu, Y.; Buffa, J. A.; Agatisa-Boyle, B.; Li, X. S.; Levison, B. S.; Hazen, S. L. Gut Microbiota-Dependent Trimethylamine N-Oxide (TMAO) Pathway Contributes to Both Development of Renal Insufficiency and Mortality Risk in Chronic Kidney Disease. *Circ. Res.* **2015**, *116*, 448–455.

(13) Johri, A. M.; Heyland, D. K.; Hétu, M.-F.; Crawford, B.; Spence, J. D. Carnitine Therapy for the Treatment of Metabolic Syndrome and Cardiovascular Disease:

Evidence and Controversies. *Nutr. Metab. Cardiovasc. Dis.* **2014**, *24*, 808–814.

(14) Zou, Q.; Bennion, B. J.; Daggett, V.; Murphy, K. P. The Molecular Mechanism of Stabilization of Proteins by TMAO and Its Ability to Counteract the Effects of Urea. *J. Am. Chem. Soc.* **2002**, *124*, 1192–1202.

(15) Hess, B.; van der Vegt, N. F. A.; Vegt, N. F. A. Van Der. Hydration Thermodynamic Properties of Amino Acid Analogues: A Systematic Comparison of Biomolecular Force Fields and Water Models. *J. Phys. Chem. B* **2006**, *110*, 17616–17626.

(16) Bagchi, B. Water Dynamics in the Hydration Layer around Proteins and Micelles. *Chem. Rev.* **2005**, *105*, 3197–3219.

(17) Bernal, J. D.; Fowler, R. H. A Theory of Water and Ionic Solution, with Particular Reference to Hydrogen and Hydroxyl Ions. *J Chem Phys F. Full J. TitleJournal Chem. Phys.* **1933**, *1*, 515–548.

(18) Berendsen, H. J. C.; Postma, J. P. M.; Gunsteren, W. F. van; Hermans, J. *Intermolecular Forces*; Pullman, B., Ed.; The Jerusalem Symposia on Quantum Chemistry and Biochemistry: Jerusalem, Israel, 1981.

(19) Berendsen, H. J. C.; Grigera, J. R.; Straatsma, T. P. The Missing Term in Effective Pair Potentials. *J. Phys. Chem.* **1987**, *91*, 6269–6271.

(20) Jorgensen, W. L.; Chandrasekhar, J.; Madura, J. D.; Impey, R. W.; Klein, M. L. Comparison of Simple Potential Functions for Simulating Liquid Water. *J. Chem. Phys.* **1983**, *79*, 926–935.

(21) Mao, Y.; Zhang, Y. Thermal Conductivity, Shear Viscosity and Specific Heat of Rigid Water Models. *Chem. Phys. Lett.* **2012**, *542*, 37–41.

(22) Weiner, S. J.; Kollman, P. A.; Nguyen, D. T.; Case, D. A. An All Atom Force Field for Simulations of Proteins and Nucleic Acids. *J. Comput. Chem.* **1986**, *7*, 230–252.

(23) Freddolino, P. L.; Harrison, C. B.; Liu, Y.; Schulten, K. Challenges in Protein-Folding Simulations. *Nat. Phys.* **2010**, *6*, 751–758.

(24) Best, R. B.; Buchete, N.-V.; Hummer, G. Are Current Molecular Dynamics Force Fields Too Helical? *Biophys. J.* **2008**, *95*, L07–L09.

(25) Best, R. B.; Hummer, G. Optimized Molecular Dynamics Force Fields Applied to the Helix-Coil Transition of Polypeptides. *J. Phys. Chem. B* **2009**, *113*, 9004–9015.

(26) Cieplak, P.; Caldwell, J.; Kollman, P. Molecular Mechanical Models for Organic and Biological Systems Going beyond the Atom Centered Two Body Additive Approximation: Aqueous Solution Free Energies of Methanol and N-Methyl Acetamide, Nucleic Acid Base, and Amide Hydrogen Bonding and Chloroform/. *J.*

Comput. Chem. **2001**, *22*, 1048–1057.

(27) Kortemme, T.; Morozov, A. V.; Baker, D. An Orientation-Dependent Hydrogen Bonding Potential Improves Prediction of Specificity and Structure for Proteins and Protein-Protein Complexes. *J. Mol. Biol.* **2003**, *326*, 1239–1259.

(28) Morozov, A. V; Kortemme, T.; Tsemekhman, K.; Baker, D. Close Agreement between the Orientation Dependence of Hydrogen Bonds Observed in Protein Structures and Quantum Mechanical Calculations. *Proc. Natl. Acad. Sci.* **2004**, *101*, 6946–6951.

(29) Morozov, A. V.; Tsemekhman, K.; Baker, D. Electron Density Redistribution Accounts for Half the Cooperativity of α Helix Formation. *J. Phys. Chem. B* **2006**, *110*, 4503–4505.

(30) Yu, H.; Van Gunsteren, W. F. Charge-on-Spring Polarizable Water Models Revisited: From Water Clusters to Liquid Water to Ice. *J. Chem. Phys.* **2004**, *121*, 9549–9564.

(31) Lamoureux, G.; Roux, B. Modeling Induced Polarization with Classical Drude Oscillators: Theory and Molecular Dynamics Simulation Algorithm. *J. Chem. Phys.* **2003**, *119*, 3025–3039.

(32) Mahoney, M. W.; Jorgensen, W. L. Quantum, Intramolecular Flexibility, and Polarizability Effects on the Reproduction of the Density Anomaly of Liquid Water by Simple Potential Functions. *J. Chem. Phys.* **2000**, *112*, 8910–8922.

(33) Majewski, P.; Pernak, A.; Grzymisławski, M.; Iwanik, K.; Pernak, J. Ionic Liquids in Embalming and Tissue Preservation: Can Traditional Formalin-Fixation Be Replaced Safely? *Acta Histochem.* **2003**, *105*, 135–142.

(34) Bösmann, A.; Datsevich, L.; Jess, A.; Lauter, A.; Schmitz, C.; Wasserscheid, P. Deep Desulfurization of Diesel Fuel by Extraction with Ionic Liquids. *Chem. Commun. (Camb).* **2001**, 2494–2495.

(35) Liu, W.; Ye, C.; Gong, Q.; Wang, H.; Wang, P. Tribological Performance of Room-Temperature Ionic Liquids as Lubricant. *Tribol. Lett.* **2002**, *13*, 81–85.

(36) Rogers, R. D.; Seddon, K. R. Ionic Liquids — Solvents of the Future? *Science* **2003**, *302*, 792–793.

(37) Wang, Y.; Voth, G. A. Unique Spatial Heterogeneity in Ionic Liquids. *J. Am. Chem. Soc.* **2005**, *127*, 12192–12193.

(38) Po, M. G. Del; Voth, G. A. On the Structure and Dynamics of Ionic Liquids. *J. Phys. Chem. B* **2004**, *108*, 1744–1752.

(39) Fruchey, K.; Fayer, M. D. Dynamics in Organic Ionic Liquids in Distinct Regions Using Charged and Uncharged Orientational Relaxation Probes. *J. Phys. Chem. B*

2010, *114*, 2840–2845.

(40) Pavese, M.; Jang, S.; Voth, G. A. Centroid Molecular Dynamics: A Quantum Dynamics Method Suitable for the Parallel Computer. *Parallel Comput.* **2000**, *26*, 1025–1041.

(41) Cao, J.; Voth, G. A. The Formulation of Quantum Statistical Mechanics Based on the Feynman Path Centroid Density. I. Equilibrium Properties. *J. Chem. Phys.* **1994**, *100*, 5093–5105.

(42) CP2K developers group http://www.cp2k.org/ (accessed May 30, 2016).

(43) Marx, D.; Hutter, J. *Ab Initio Molecular Dynamics: Basic Theory and Advanced Methods*; Cambridge University Press: Cambridge, England, 2009.

(44) Ewald, P. P. Die Berechnung Optischer Und Elektrostatischer Gitterpotentiale. *Ann. Phys.* **1921**, *369*, 253–287.

(45) Nosé, S. A Unified Formulation of the Constant Temperature Molecular Dynamics Methods. *J. Chem. Phys.* **1984**, *81*, 511–519.

(46) Hoover, W. G. Canonical Dynamics: Equilibrium Phase-Space Distributions. *Phys. Rev. A* **1985**, *31*, 1695–1697.

(47) Koopmans, T. UEBER DIE ZUORDNUNG VON WELLENFUNKTIONEN UND EIGENWERTEN ZU DEN EINZELNEN ELEKTRONEN EINES ATOMS. *Physica* **1934**, *1*, 104–113.

(48) Becke, A. D. Density-Functional Exchange-Energy Approximation with Correct Asymptotic Behavior. *Phys. Rev. A* **1988**, *38*, 3098–3100.

(49) Perdew, J. P.; Burke, K.; Ernzerhof, M. Generalized Gradient Approximation Made Simple. *Phys. Rev. Lett.* **1996**, *77*, 3865–3868.

(50) Zhang, Y.; Yang, W. Comment on “Generalized Gradient Approximation Made Simple.” *Phys. Rev. Lett.* **1998**, *80*, 890–890.

(51) Lee, C.; Yang, W.; Parr, R. G. Development of the Colle-Salvetti Correlation-Energy Formula into a Functional of the Electron Density. *Phys. Rev. B* **1988**, *37*, 785–789.

(52) Roothaan, C. C. J. New Developments in Molecular Orbital Theory. *Rev. Mod. Phys.* **1951**, *23*, 69–89.

(53) Vandevondele, J.; Krack, M.; Mohamed, F.; Parrinello, M.; Chassaing, T.; Hutter, J. Quickstep: Fast and Accurate Density Functional Calculations Using a Mixed Gaussian and Plane Waves Approach. *Comput. Phys. Commun.* **2005**, *167*, 103–128.

(54) Stillinger, F. H. Water Revisited. *Science* **1980**, *209*, 451–457.

(55) Canchi, D. R.; García, A. E. Cosolvent Effects on Protein Stability. *Annu. Rev. Phys. Chem.* **2013**, *64*, 273–293.

(56) Rajan, R. S.; Tsumoto, K.; Tokunaga, M.; Tokunaga, H.; Kita, Y.; Arakawa, T. Chemical and Pharmacological Chaperones: Application for Recombinant Protein Production and Protein Folding Diseases. *Curr. Med. Chem.* **2011**, *18*, 1–15.

(57) Levine, Z. A.; Larini, L.; LaPointe, N. E.; Feinstein, S. C.; Shea, J.-E. Regulation and Aggregation of Intrinsically Disordered Peptides. *Proc. Natl. Acad. Sci.* **2015**, *112*, 2758–2763.

(58) Denning, E. J.; Thirumalai, D.; Mackerell Jr., A. D. Protonation of Trimethylamine N-Oxide (TMAO) Is Required for Stabilization of RNA Tertiary Structure. *Biophys. Chem.* **2013**, *184*, 8–16.

(59) Ganguly, P.; Hajari, T.; Shea, J.-E.; van der Vegt, N. F. A. Mutual Exclusion of Urea and Trimethylamine N-Oxide from Amino Acids in Mixed Solvent Environment. *J. Phys. Chem. Lett.* **2015**, *6*, 581–585.

(60) Yancey, P. H. Water Stress, Osmolytes and Proteins. *Am. Zool.* **2001**, *41*, 699–709.

(61) Yancey, P. H.; Blake, W. R.; Conley, J. Unusual Organic Osmolytes in Deep-Sea Animals: Adaptations to Hydrostatic Pressure and Other Perturbants. *Comp. Biochem. Physiol. - A Mol. Integr. Physiol.* **2002**, *133*, 667–676.

(62) Gillett, M. B.; Suko, J. R.; Santoso, F. O.; Yancey, P. H. Elevated Levels of Trimethylamine Oxide in Muscles of Deep-Sea Gadiform Teleosts: A High-Pressure Adaptation? *J. Exp. Zool.* **1997**, *279*, 386–391.

(63) Bennion, B. J.; Daggett, V. Counteraction of Urea-Induced Protein Denaturation by Trimethylamine N-Oxide: A Chemical Chaperone at Atomic Resolution. *Proc. Natl. Acad. Sci.* **2004**, *101*, 6433–6438.

(64) Auton, M.; Bolen, D. W. Predicting the Energetics of Osmolyte-Induced Protein Folding/unfolding. *Proc. Natl. Acad. Sci.* **2005**, *102*, 15065–15068.

(65) Auton, M.; Bolen, D. W.; Rösgen, J. Structural Thermodynamics of Protein Preferential Solvation: Osmolyte Solvation of Proteins, Aminoacids, and Peptides. *Proteins Struct. Funct. Genet.* **2008**, *73*, 802–813.

(66) Courtenay, E. S.; Capp, M. W.; Anderson, C. F.; Record Jr., M. T. Vapor Pressure Osmometry Studies of Osmolyte-Protein Interactions: Implications for the Action of Osmoprotectants in Vivo and for the Interpretation of "Osmotic Stress" Experiments in Vitro. *Biochemistry* **2000**, *39*, 4455–4471.

(67) Bolen, D. W.; Baskakov, I. V. The Osmophobic Effect: Natural Selection of a Thermodynamic Force in Protein Folding. *J. Mol. Biol.* **2001**, *310*, 955–963.

(68) Canchi, D. R.; Jayasimha, P.; Rau, D. C.; Makhatadze, G. I.; Garcia, A. E. Molecular

Mechanism for the Preferential Exclusion of TMAO from Protein Surfaces. *J. Phys. Chem. B* **2012**, *116*, 12095–12104.

(69) Hunger, J.; Ottosson, N.; Mazur, K.; Bonn, M.; Bakker, H. J. Water-Mediated Interactions between Trimethylamine-*N*-Oxide and Urea. *Phys. Chem. Chem. Phys.* **2015**, *17*, 298–306.

(70) Comez, L.; Lupi, L.; Morresi, A.; Paolantoni, M.; Sassi, P.; Fioretto, D. More Is Different: Experimental Results on the Effect of Biomolecules on the Dynamics of Hydration Water. *J. Phys. Chem. Lett.* **2013**, *4*, 1188–1192.

(71) Mondal, J.; Stirnemann, G.; Berne, B. J. When Does Trimethylamine *N*-Oxide Fold a Polymer Chain and Urea Unfold It? *J. Phys. Chem. B* **2013**, *117*, 8723–8732.

(72) Panuszko, A.; Bruździak, P.; Zielkiewicz, J.; Wyrzykowski, D.; Stangret, J. Effects of Urea and Trimethylamine-*N*-Oxide on the Properties of Water and the Secondary Structure of Hen Egg White Lysozyme. *J. Phys. Chem. B* **2009**, *113*, 14797–14809.

(73) Gluick, T. C.; Yadav, S. Trimethylamine *N*-Oxide Stabilizes RNA Tertiary Structure and Attenuates the Denaturating Effects of Urea. *J. Am. Chem. Soc.* **2003**, *125*, 4418–4419.

(74) Kokubo, H.; Hu, C. Y.; Pettitt, B. M. Peptide Conformational Preferences in Osmolyte Solutions: Transfer Free Energies of Decaalanine. *J. Am. Chem. Soc.* **2011**, *133*, 1849–1858.

(75) O'Brien, E. P.; Ziv, G.; Haran, G.; Brooks, B. R.; Thirumalai, D. Effects of Denaturants and Osmolytes on Proteins Are Accurately Predicted by the Molecular Transfer Model. *Proc. Natl. Acad. Sci.* **2008**, *105*, 13403–13408.

(76) Rösgen, J.; Jackson-Atogi, R. Volume Exclusion and H-Bonding Dominate the Thermodynamics and Solvation of Trimethylamine-*N*-Oxide in Aqueous Urea. *J. Am. Chem. Soc.* **2012**, *134*, 3590–3597.

(77) Mondal, J. A.; Nihonyanagi, S.; Yamaguchi, S.; Tahara, T. Three Distinct Water Structures at a Zwitterionic Lipid/water Interface Revealed by Heterodyne-Detected Vibrational Sum Frequency Generation. *J. Am. Chem. Soc.* **2012**, *134*, 7842–7850.

(78) Stirnemann, G.; Sterpone, F.; Laage, D. Dynamics of Water in Concentrated Solutions of Amphiphiles: Key Roles of Local Structure and Aggregation. *J. Phys. Chem. B* **2011**, *115*, 3254–3262.

(79) Kuffel, A.; Zielkiewicz, J. The Hydrogen Bond Network Structure within the Hydration Shell around Simple Osmolytes: Urea, Tetramethylurea, and Trimethylamine-*N*-Oxide, Investigated Using Both a Fixed Charge and a Polarizable Water Model. *J. Chem. Phys.*

2010, *133*, 035102.

(80) Doi, H.; Watanabe, Y.; Aida, M. Influence of Trimethylamine N-Oxide (TMAO) on the Three-Dimensional Distribution and Alignment of Solvent Molecules in Aqueous Solution. *Chem. Lett.* **2014**, *43*, 865–867.

(81) Stirnemann, G.; Hynes, J. T.; Laage, D. Water Hydrogen Bond Dynamics in Aqueous Solutions of Amphiphiles. *J. Phys. Chem. B* **2010**, *114*, 3052–3059.

(82) Laage, D.; Stirnemann, G.; Hynes, J. T. Why Water Reorientation Slows without Iceberg Formation around Hydrophobic Solutes. *J. Phys. Chem. B* **2009**, *113*, 2428–2435.

(83) Duboué-Dijon, E.; Fogarty, A. C.; Laage, D. Temperature Dependence of Hydrophobic Hydration Dynamics: From Retardation to Acceleration. *J. Phys. Chem. B* **2014**, *118*, 1574–1583.

(84) Paul, S.; Patey, G. N. The Influence of Urea and Trimethylamine-*N*-Oxide on Hydrophobic Interactions. *J. Phys. Chem. B* **2007**, *111*, 7932–7933.

(85) Paul, S.; Patey, G. N. Structure and Interaction in Aqueous Urea-Trimethylamine-*N*-Oxide Solutions. *J. Am. Chem. Soc.* **2007**, *129*, 4476–4482.

(86) Paul, S.; Patey, G. N. Why Tert-Butyl Alcohol Associates in Aqueous Solution but Trimethylamine-*N*-Oxide Does Not. *J. Phys. Chem. B* **2006**, *110*, 10514–10518.

(87) Biyani, N.; Paul, S. Hydrophobic Interactions in Water-Trimethylamine-*N*-Oxide Solutions: The Effects of Pressure. *J. Phys. Chem. B* **2009**, *113*, 9644–9645.

(88) Sharp, K. A.; Madan, B.; Manas, E.; Vanderkooi, J. M. Water Structure Changes Induced by Hydrophobic and Polar Solutes Revealed by Simulations and Infrared Spectroscopy. *J. Chem. Phys.* **2001**, *114*, 1791–1796.

(89) Sinibaldi, R.; Casieri, C.; Melchionna, S.; Onori, G.; Segre, A. L.; Viel, S.; Mannina, L.; De Luca, F. The Role of Water Coordination in Binary Mixtures. a Study of Two Model Amphiphilic Molecules in Aqueous Solutions by Molecular Dynamics and NMR. *J. Phys. Chem. B* **2006**, *110*, 8885–8892.

(90) Schneck, E.; Horinek, D.; Netz, R. R. Insight into the Molecular Mechanisms of Protein Stabilizing Osmolytes from Global Force-Field Variations. *J. Phys. Chem. B* **2013**, *117*, 8310–8321.

(91) Freda, M.; Onori, H.; Santucci, A. Infrared and Dielectric Spectroscopy Study of the Water Perturbation Induced by Two Small Organic Solutes. *J. Mol. Struct.* **2001**, *565-566*, 153–157.

(92) Freda, M.; Onori, G.; Santucci, A. Infrared Study of the Hydrophobic Hydration and

Hydrophobic Interactions in Aqueous Solutions of *Tert*-Butyl Alcohol and Trimethylamine-*N*-Oxide. *J. Phys. Chem. B* **2001**, *105*, 12714–12718.

(93) Rezus, Y. L. A.; Bakker, H. J. Observation of Immobilized Water Molecules around Hydrophobic Groups. *Phys. Rev. Lett.* **2007**, *99*, 148301.

(94) Rezus, Y. L. A.; Bakker, H. J. Destabilization of the Hydrogen-Bond Structure of Water by the Osmolyte Trimethylamine *N*-Oxide. *J. Phys. Chem. B* **2009**, *113*, 4038–4044.

(95) Hunger, J.; Tielrooij, K. J.; Buchner, R.; Bonn, M.; Bakker, H. J. Complex Formation in Aqueous Trimethylamine-*N*-Oxide (TMAO) Solutions. *J. Phys. Chem. B* **2012**, *116*, 4783–4795.

(96) Bakulin, A. A.; Pshenichnikov, M. S.; Bakker, H. J.; Petersen, C. Hydrophobic Molecules Slow down the Hydrogen-Bond Dynamics of Water. *J. Phys. Chem. A* **2011**, *115*, 1821–1829.

(97) Munroe, K. L.; Magers, D. H.; Hammer, N. I. Raman Spectroscopic Signatures of Noncovalent Interactions between Trimethylamine N-Oxide (TMAO) and Water. *J. Phys. Chem. B* **2011**, *115*, 7699–7707.

(98) Mazur, K.; Heisler, I. A.; Meech, S. R. THz Spectra and Dynamics of Aqueous Solutions Studied by the Ultrafast Optical Kerr Effect. *J. Phys. Chem. B* **2011**, *115*, 2563–2573.

(99) Qvist, J.; Halle, B. Thermal Signature of Hydrophobic Hydration Dynamics. *J. Am. Chem. Soc.* **2008**, *130*, 10345–10353.

(100) Shikata, T.; Itatani, S. Dielectric Relaxation of Aqueous Trimethylamineoxide Solutions. *J. Solution Chem.* **2002**, *31*, 823–844.

(101) Silvestrelli, P. L. Are There Immobilized Water Molecules around Hydrophobic Groups? Aqueous Solvation of Methanol from First Principles. *J. Phys. Chem. B* **2009**, *113*, 10728–10731.

(102) Sterpone, F.; Stirnemann, G.; Hynes, J. T.; Laage, D. Water Hydrogen-Bond Dynamics around Amino Acids: The Key Role of Hydrophilic Hydrogen-Bond Acceptor Groups. *J. Phys. Chem. B* **2010**, *114*, 2083–2089.

(103) Laage, D.; Hynes, J. T. A Molecular Jump Mechanism of Water Reorientation. *Science* **2006**, *311*, 832–835.

(104) Laage, D.; Hynes, J. T. On the Molecular Mechanism of Water Reorientation. *J. Phys. Chem. B* **2008**, *112*, 14230–14242.

(105) Fogarty, A. C.; Duboué-Dijon, E.; Sterpone, F.; Hynes, J. T.; Laage, D. Biomolecular Hydration Dynamics: A Jump Model Perspective. *Chem. Soc. Rev.* **2013**, *42*, 5672–

5683.

(106) Laage, D.; Hynes, J. T. Reorientional Dynamics of Water Molecules in Anionic Hydration Shells. *Proc. Natl. Acad. Sci.* **2007**, *104*, 11167–11172.

(107) Fogarty, A. C.; Coudert, F. X.; Boutin, A.; Laage, D. Reorientational Dynamics of Water Confined in Zeolites. *ChemPhysChem* **2014**, *15*, 521–529.

(108) Laage, D.; Hynes, J. T. Do More Strongly Hydrogen-Bonded Water Molecules Reorient More Slowly? *Chem. Phys. Lett.* **2006**, *433*, 80–85.

(109) Fogarty, A. C.; Duboué-Dijon, E.; Laage, D.; Thompson, W. H. Origins of the Non-Exponential Reorientation Dynamics of Nanoconfined Water. *J. Chem. Phys.* **2014**, *141*, 18C523.

(110) Kast, K. M.; Brickmann, J.; Kast, S. M.; Berry, R. S. Binary Phases of Aliphatic *N*-Oxides and Water: Force Field Development and Molecular Dynamics Simulation. *J. Phys. Chem. A* **2003**, *107*, 5342–5351.

(111) Kocherbitov, V.; Veryazov, V.; Söderman, O. Hydration of Trimethylamine-*N*-Oxide and of Dimethyldodecylamine-*N*-Oxide: An *Ab Initio* Study. *J. Mol. Struct. THEOCHEM* **2007**, *808*, 111–118.

(112) Lee, H.-S.; Tuckerman, M. E. Dynamical Properties of Liquid Water from *Ab Initio* Molecular Dynamics Performed in the Complete Basis Set Limit. *J. Chem. Phys.* **2007**, *126*, 164501.

(113) Chandra, A.; Tuckerman, M. E.; Marx, D. Connecting Solvation Shell Structure to Proton Transport Kinetics in Hydrogen-Bonded Networks via Population Correlation Functions. *Phys. Rev. Lett.* **2007**, *99*, 145901.

(114) Makarov, D. M.; Egorov, G. I.; Kolker, A. M. Density and Volumetric Properties of Aqueous Solutions of Trimethylamine *N*-Oxide in the Temperature Range from (278.15 to 323.15) K and at Pressures up to 100 MPa. *J. Chem. Eng. Data* **2015**, *60*, 1291–1299.

(115) Bussi, G.; Donadio, D.; Parrinello, M. Canonical Sampling through Velocity Rescaling. *J. Chem. Phys.* **2007**, *126*, 014101.

(116) Lee, C.; Yang, W.; Parr, R. G. Development of the Colle-Salvetti Correlation-Energy Formula into a Functional of the Electron Density. *Phys. Rev. B* **1988**, *37*, 785–789.

(117) Grimme, S.; Antony, J.; Ehrlich, S.; Krieg, H. A Consistent and Accurate Ab Initio Parametrization of Density Functional Dispersion Correction (DFT-D) for the 94 Elements H-Pu. *J. Chem. Phys.* **2010**, *132*, 154104.

(118) Lin, I.-C.; Seitsonen, A. P.; Tavernelli, I.; Rothlisberger, U. Structure and Dynamics of

Liquid Water from Ab Initio Molecular Dynamics-Comparison of BLYP, PBE, and revPBE Density Functionals with and without van Der Waals Corrections. *J. Chem. Theory Comput.* **2012**, *8*, 3902–3910.

(119) Lin, I.-C.; Seitsonen, A. P.; Coutinho-Neto, M. D.; Tavernelli, I.; Rothlisberger, U. Importance of van Der Waals Interactions in Liquid Water. *J. Phys. Chem. B* **2009**, *113*, 1127–1131.

(120) Kühne, T. D.; Pascal, T. A.; Kaxiras, E.; Jung, Y. New Insights into the Structure of the Vapor/water Interface from Large-Scale First-Principles Simulations. *J. Phys. Chem. Lett.* **2011**, *2*, 105–113.

(121) Goedecker, S.; Teter, M.; Hutter, J. Separable Dual-Space Gaussian Pseudopotentials. *Phys. Rev. B* **1996**, *54*, 1703–1710.

(122) Jonchiere, R.; Seitsonen, A. P.; Ferlat, G.; Saitta, A. M.; Vuilleumier, R. Van Der Waals Effects in *Ab Initio* Water at Ambient and Supercritical Conditions. *J. Chem. Phys.* **2011**, *135*, 154503.

(123) Wu, Y.; Tepper, H. L.; Voth, G. A. Flexible Simple Point-Charge Water Model with Improved Liquid-State Properties. *J. Chem. Phys.* **2006**, *124*, 024503.

(124) Kuo, I.-F. W.; Mundy, C. J. An Ab Initio Molecular Dynamics Study of the Aqueous Liquid-Vapor Interface. *Science* **2004**, *303*, 658–660.

(125) Kumar, R.; Schmidt, J. R.; Skinner, J. L. Hydrogen Bonding Definitions and Dynamics in Liquid Water. *J. Chem. Phys.* **2007**, *126*, 204107.

(126) Titantah, J. T.; Karttunen, M. Long-Time Correlations and Hydrophobe-Modified Hydrogen-Bonding Dynamics in Hydrophobic Hydration. *J. Am. Chem. Soc.* **2012**, *134*, 9362–9368.

(127) Titantah, J. T.; Karttunen, M. Water Dynamics: Relation between Hydrogen Bond Bifurcations, Molecular Jumps, Local Density & Hydrophobicity. *Sci. Rep.* **2013**, *3*, 2991.

(128) Hovagimyan, K. G.; Gerig, J. T. Interactions of Trimethylamine *N*-Oxide and Water with Cyclo-Alanylglycine. *J. Phys. Chem. B* **2005**, *109*, 24142–24151.

(129) Corcelli, S. A.; Lawrence, C. P.; Skinner, J. L. Combined Electronic Structure/molecular Dynamics Approach for Ultrafast Infrared Spectroscopy of Dilute HOD in Liquid H_2O and D_2O. *J. Chem. Phys.* **2004**, *120*, 8107–8117.

(130) Bakker, H. J.; Skinner, J. L. Vibrational Spectroscopy as a Probe of Structure and Dynamics in Liquid Water. *Chem. Rev.* **2010**, *110*, 1498–1517.

(131) Luzar, A.; Chandler, D. Hydrogen-Bond Kinetics in Liquid Water. *Nature* **1996**, *379*,

55–57.

(132) Sulpizi, M.; Salanne, M.; Sprik, M.; Gaigeot, M.-P. Vibrational Sum Frequency Generation Spectroscopy of the Water Liquid–Vapor Interface from Density Functional Theory-Based Molecular Dynamics Simulations. *J. Phys. Chem. Lett.* **2013**, *4*, 83–87.

(133) Nagata, Y.; Yoshimune, S.; Hsieh, C.-S.; Hunger, J.; Bonn, M. Ultrafast Vibrational Dynamics of Water Disentangled by Reverse Nonequilibrium Ab Initio Molecular Dynamics Simulations. *Phys. Rev. X* **2015**, *021002*, 1–11.

(134) Petersen, C.; Tielrooij, K.-J.; Bakker, H. J. Strong Temperature Dependence of Water Reorientation in Hydrophobic Hydration Shells. *J. Chem. Phys.* **2009**, *130*, 214511.

(135) Moilanen, D. E.; Fenn, E. E.; Lin, Y.-S.; Skinner, J. L.; Bagchi, B.; Fayer, M. D. Water Inertial Reorientation: Hydrogen Bond Strength and the Angular Potential. *Proc. Natl. Acad. Sci.* **2008**, *105*, 5295–5300.

(136) Larini, L.; Shea, J.-E. Double Resolution Model for Studying TMAO/water Effective Interactions. *J. Phys. Chem. B* **2013**, *117*, 13268–13277.

(137) Abascal, J. L.; Vega, C. A General Purpose Model for the Condensed Phases of Water: TIP4P/2005. *J. Chem. Phys.* **2005**, *123*, 234505.

(138) Mahoney, M. W.; Jorgensen, W. L. A Five-Site Model for Liquid Water and the Reproduction of the Density Anomaly by Rigid, Nonpolarizable Potential Functions. *J. Chem. Phys.* **2000**, *112*, 8910.

(139) Schmidt, J.; Vandevondele, J.; Kuo, I. F. W.; Sebastiani, D.; Siepmann, J. I.; Hutter, J.; Mundy, C. J. Isobaric-Isothermal Molecular Dynamics Simulations Utilizing Density Functional Theory: An Assessment of the Structure and Density of Water at near-Ambient Conditions. *J. Phys. Chem. B* **2009**, *113*, 11959–11964.

(140) Kühne, T. D.; Krack, M.; Parrinello, M. Static and Dynamical Properties of Liquid Water from First Principles by a Novel Car-Parrinello-like Approach. *J. Chem. Theory Comput.* **2009**, *5*, 235–241.

(141) Del Ben, M.; Schönherr, M.; Hutter, J.; Vandevondele, J. Bulk Liquid Water at Ambient Temperature and Pressure from MP2 Theory. *J. Phys. Chem. Lett.* **2013**, *4*, 3753–3759.

(142) VandeVondele, J.; Mohamed, F.; Krack, M.; Hutter, J.; Sprik, M.; Parrinello, M. The Influence of Temperature and Density Functional Models in *Ab Initio* Molecular Dynamics Simulation of Liquid Water. *J. Chem. Phys.* **2005**, *122*, 014515.

(143) Leandro, P.; Gomes, C. M. Protein Misfolding in Conformational Disorders: Rescue of Folding Defects and Chemical Chaperoning. *Mini Rev. Med. Chem.* **2008**, *8*, 901–911.

(144) Knake, L.; Schwaab, G.; Kartaschew, K.; Havenith, M. Solvation Dynamics of

Trimethylamine *N*-Oxide in Aqueous Solution Probed by Terahertz Spectroscopy. *J. Phys. Chem. B* **2015**, *119*, 13842–13851.

(145) Brotzakis, Z. F.; Groot, C. C. M.; Homsi Brandeburgo, W.; Bakker, H. J.; Bolhuis, P. G. Dynamics of Hydration Water Around Native and Misfolded α-Lactalbumin. *J. Phys. Chem. B* **2016**, *120*, 4756–4766.

(146) Usui, K.; Hunger, J.; Sulpizi, M.; Ohto, T.; Bonn, M.; Nagata, Y. Ab Initio Liquid Water Dynamics in Aqueous TMAO Solution. *J. Phys. Chem. B* **2015**, *119*, 10597–10606.

(147) Imoto, S.; Forbert, H.; Marx, D. Water Structure and Solvation of Osmolytes at High Hydrostatic Pressure: Pure Water and Tmao Solutions at 10 Kbar Versus 1 Bar. *Phys. Chem. Chem. Phys.* **2015**, *17*, 24224–24237.

(148) Hölzl, C.; Kibies, P.; Imoto, S.; Frach, R.; Suladze, S.; Winter, R.; Marx, D.; Horinek, D.; Kast, S. M. Design Principles for High–pressure Force Fields: Aqueous TMAO Solutions from Ambient to Kilobar Pressures. *J. Chem. Phys.* **2016**, *144*, 144104.

(149) Cho, S. S.; Reddy, G.; Straub, J. E.; Thirumalai, D. Entropic Stabilization of Proteins by TMAO. *J. Phys. Chem. B* **2011**, *115*, 13401–13407.

(150) Chand, A.; Chettiyankandy, P.; Pattanayak, S. K.; Chowdhuri, S. Effects of Trimethylamine-N-Oxide (TMAO) on Aqueous N-Methylacetamide Solution: A Comparison of Different Force Fields of TMAO. *J. Mol. Liq.* **2016**.

(151) Kuo, I.-F. W.; Mundy, C. J.; McGrath, M. J.; Siepmann, J. I.; VandeVondele, J.; Sprik, M.; Hutter, J.; Chen, B.; Klein, M. L.; Mohamed, F.; et al. Liquid Water from First Principles: Investigation of Different Sampling Approaches. *J. Phys. Chem. B* **2004**, *108*, 12990–12998.

(152) Kell, G. S. Density, Thermal Expansivity, and Compressibility of Liquid Water from 0" to 150°C: Correlations and Tables for Atmospheric Pressure and Saturation Reviewed and Expressed on 1968 Temperature Scale. *J. Chem. Eng. Data* **1975**, *20*, 97–105.

(153) Hansen, J.-P.; McDonald, I. R. *Theory of Simple Liquids*; Fourth Edi.; Academic Press: Cambridge, the United States of America, 2013.

(154) Auer, B.; Kumar, R.; Schmidt, J. R.; Skinner, J. L. Hydrogen Bonding and Raman, IR, and 2D-IR Spectroscopy of Dilute HOD in Liquid D2O. *Proc. Natl. Acad. Sci.* **2007**, *104*, 14215–14220.

(155) Brandeburgo, W. H.; van der Post, S. T.; Meijer, E. J.; Ensing, B. On the Slowdown Mechanism of Water Dynamics around Small Amphiphiles. *Phys. Chem. Chem. Phys.* **2015**, *17*, 24968–24977.

(156) Graziano, G. How Does Trimethylamine *N*-Oxide Counteract the Denaturing Activity

of Urea? *Phys. Chem. Chem. Phys.* **2011**, *13*, 17689–17695.

(157) Welton, T. Room-Temperature Ionic Liquids . Solvents for Synthesis and Catalysis. *Chem. Rev.* **1999**, *99*, 2071–2083.

(158) Seddon, K. R. Review Ionic Liquids for Clean Technology. *J. Chem. Tech. Biotechnol.* **1997**, *68*, 351–356.

(159) Plechkova, N. V; Seddon, K. R. Applications of Ionic Liquids in the Chemical Industry. *Chem. Soc. Rev.* **2008**, *37*, 123–150.

(160) Carmichael, A. J.; Seddon, K. R. Polarity Study of Some 1-Alkyl-3-Methylimidazolium Ambient-Temperature Ionic Liquids with the Solvatochromic. *J. Phys. Org. Chem.* **2000**, *13*, 591–595.

(161) Cull, S. G.; Holbrey, J. D.; Vargas-Mora, V.; Seddon, K. R.; Lye, G. J. Room-Temperature Ionic Liquids as Multiphase Bioprocess Operations. *Biotechnol. Bioeng.* **2000**, *69*, 227–233.

(162) Armand, M.; Endres, F.; Macfarlane, D. R.; Ohno, H.; Scrosati, B. Ionic-Liquid Materials for the Electrochemical Challenges of the Future. *Nat. Mater.* **2009**, *8*, 621–629.

(163) Zhang, S.; Sun, N.; He, X.; Lu, X.; Zhang, X.; Zhang, S.; Sun, N.; He, X.; Lu, X.; Zhang, X. Physical Properties of Ionic Liquids : Database and Evaluation Physical Properties of Ionic Liquids : Database and Evaluation. *J. Phys. Chem. Ref. Data* **2006**, *35*, 1475–1517.

(164) Baaden, M.; Burgard, M.; Wipff, G. TBP at the Water-Oil Interface: The Effect of TBP Concentration and Water Acidity Investigated by Molecular Dynamics Simulations. *J. Phys. Chem. B* **2001**, *105*, 11131–11141.

(165) Mcdaniel, J. G.; Choi, E.; Son, C. Y.; Schmidt, J. R.; Yethiraj, A. Ab Initio Force Fields for Imidazolium-Based Ionic Liquids. *J. Phys. Chem. B* **2016**, *120*, 7024–7036.

(166) Kramer, P. L.; Giammanco, C. H.; Fayer, M. D. Dynamics of Water, Methanol, and Ethanol in a Room Temperature Ionic Liquid. *J. Chem. Phys.* **2015**, *142*, 212408.

(167) Giammanco, C. H.; Kramer, P. L.; Wong, D. B.; Fayer, M. D. Water Dynamics in 1-Alkyl-3-Methylimidazolium Tetrafl Uoroborate Ionic Liquids. *J. Phys. Chem. B* **2016**, *120*, 11523–11538.

(168) Zahn, S.; Thar, J.; Kirchner, B. Structure and Dynamics of the Protic Ionic Liquid Monomethylammonium Nitrate ([CH_3NH3][NO3]) from Ab Initio Molecular Dynamics Simulations. *J. Chem. Phys.* **2010**, *132*, 124506.

(169) Tokuda, H.; Hayamizu, K.; Ishii, K.; Bin, A.; Susan, H.; Watanabe, M.

Physicochemical Properties and Structures of Room Temperature Ionic Liquids . 2 . Variation of Alkyl Chain Length in Imidazolium Cation. *J. Phys. Chem. B* **2005**, *109*, 6103–6110.

(170) Van-Oanh, N.-T.; Houriez, C.; Rousseau, B. Viscosity of the 1-Ethyl-3-Methylimidazolium Bis(Trifluoromethylsulfonyl)imide Ionic Liquid from Equilibrium and Nonequilibrium Molecular Dynamics. *Phys. Chem. Chem. Phys.* **2010**, *12*, 930–936.

(171) Brehm, M.; Weber, H.; Thomas, M.; Hollóczki, O.; Kirchner, B. Domain Analysis in Nanostructured Liquids: A Post-Molecular Dynamics Study at the Example of Ionic Liquids. *ChemPhysChem* **2015**, *16*, 3271–3277.

(172) Castner, E. W.; Margulis, C. J.; Maroncelli, M.; Wishart, J. F. Ionic Liquids: Structure and Photochemical Reactions. *Annu. Rev. Phys. Chem.* **2011**, *62*, 85–105.

(173) Maginn, E. J. Molecular Simulation of Ionic Liquids: Current Status and Future Opportunities. *J. Phys. Condens. Matter* **2009**, *21*, 373101.

(174) Fumino, K.; Wulf, A.; Ludwig, R. Strong, Localized, and Directional Hydrogen Bonds Fluidize Ionic Liquids. *Angew. Chemie - Int. Ed.* **2008**, *47*, 8731–8734.

(175) Greaves, T. L.; Weerawardena, A.; Fong, C.; Krodkiewska, I.; Drummond, C. J. Protic Ionic Liquids : Solvents with Tunable Phase Behavior and Physicochemical Properties. *J. Phys. Chem. B* **2006**, *110*, 22479–22487.

(176) Schröder, C. Comparing Reduced Partial Charge Models with Polarizable Simulations of Ionic Liquids. *Phys. Chem. Chem. Phys.* **2012**, *14*, 3089–3102.

(177) Schröder, C.; Steinhauser, O. Simulating Polarizable Molecular Ionic Liquids with Drude Oscillators. *J. Chem. Phys.* **2010**, *133*, 154511.

(178) Wang, Y.; Voth, G. A. Tail Aggregation and Domain Diffusion in Ionic Liquids. *J. Phys. Chem. B* **2006**, *110*, 18601–18608.

(179) Wang, Y.; Jiang, W. E. I.; Yan, T.; Voth, G. a. Understanding Ionic Liquids through Atomistic and Coarse-Grained Molecular Dynamics Simulations. *Acc. Chem. Res.* **2007**, *40*, 1193–1199.

(180) Lopes, J. N. A. C.; Pádua, A. A. H. Nanostructural Organization in Ionic Liquids. *J. Phys. Chem. B* **2006**, *110*, 3330–3335.

(181) Triolo, A.; Russina, O.; Bleif, H.-J.; Di Cola, E. Nanoscale Segregation in Room Temperature Ionic Liquids. *J. Phys. Chem. B* **2007**, *111*, 4641–4644.

(182) Salanne, M. Simulations of Room Temperature Ionic Liquids: From Polarizable to Coarse-Grained Force Fields. *Phys. Chem. Chem. Phys.* **2015**, *17*, 14270–14279.

(183) Russina, O.; Triolo, A.; Gontrani, L.; Caminiti, R. Mesoscopic Structural Heterogeneities in Room Temperature Ionic Liquids. *J. Phys. Chem. Lett.* **2012**, *3*, 27.

(184) Hayes, R.; Warr, G. G.; Atkin, R. Structure and Nanostructure in Ionic Liquids. *Chem. Rev.* **2015**, *115*, 6357–6426.

(185) Song, X.; Hamano, H.; Minofar, B.; Kanzaki, R.; Fujii, K.; Kameda, Y.; Kohara, S.; Watanabe, M.; Ishiguro, S.; Umebayashi, Y. Structural Heterogeneity and Unique Distorted Hydrogen Bonding in Primary Ammonium Nitrate Ionic Liquids Studied by High-Energy X-Ray Diffraction Experiments and MD Simulations. *J. Phys. Chem. B* **2012**, *116*, 2801–2813.

(186) Gebremichael, Y.; Schrøder, T. B.; Starr, F. W.; Glotzer, S. C. Spatially Correlated Dynamics in a Simulated Glass-Forming Polymer Melt: Analysis of Clustering Phenomena. *Phys. Rev. E* **2001**, *64*, 051503.

(187) Kob, W.; Donati, C.; Plimpton, S.; Poole, P.; Glotzer, S. Dynamical Heterogeneities in a Supercooled Lennard-Jones Liquid. *Phys. Rev. Lett.* **1997**, *79*, 2827–2830.

(188) Qian, J.; Hentsche, R.; Heuer, A. Dynamic Heterogeneities of Translational and Rotational Motion of a Molecular Glass Former from Computer Simulations. *J. Chem. Phys.* **1999**, *110*, 4514–4522.

(189) Kim, J.; Li, W.-X.; Keyes, T. Probes of Heterogeneity in Rotational Dynamics: Application to Supercooled Liquid CS_2. *Phys. Rev. E* **2003**, *67*, 021506.

(190) van Hove, L. Correlations in Space and Time and Born Approximation Scattering in Systems of Interacting Particles. *Phys. Rev.* **1954**, *95*, 249–262.

(191) Zheng, Z.; Fan, W.; Roy, S.; Mazur, K.; Nazet, A.; Buchner, R.; Bonn, M.; Hunger, J. Ionic Liquids: Not Only Structurally but Also Dynamically Heterogeneous. *Angew. Chemie - Int. Ed.* **2015**, *54*, 687–690.

(192) Verma, S. D.; Corcelli, S. A.; Berg, M. A. Rate and Amplitude Heterogeneity in the Solvation Response of an Ionic Liquid. *J. Phys. Chem. Lett.* **2016**, *7*, 504–508.

(193) Zhang, X.; Breffke, J.; Ernsting, P.; Maroncelli, M. Observations of Probe Dependence of the Solvation Dynamics in Ionic Liquids. *Phys. Chem. Chem. Phys.* **2015**, *17*, 12949–12956.

(194) Ito, N.; Arzhantsev, S.; Maroncelli, M. The Probe Dependence of Solvation Dynamics and Rotation in the Ionic Liquid 1-Butyl-3-Methyl-Imidazolium Hexafluorophosphate. *Chem. Phys. Lett.* **2004**, *396*, 83–91.

(195) Jin, H.; Li, X. A.; Maroncelli, M. Heterogeneous Solute Dynamics in Room-Temperature Ionic Liquids. *J. Phys. Chem. B* **2010**, *114*, 11370.

(196) Arzhantsev, S.; Jin, H.; Baker, G. A.; Maroncelli, M. Measurements of the Complete Solvation Response in Ionic Liquids. *J. Phys. Chem. B* **2007**, *111*, 4978–4989.

(197) Wu, E. C.-K.; Kim, H. J.; Peteanu, L. A. Structural and Dynamical Heterogeneities in Ionic Liquids Revealed by MD Simulations and Single-Molecule Fluorescence. *J. Phys. Chem. B* **2017**, *121*, 1100–1107.

(198) Hu, Z.; Margulis, C. J. Heterogeneity in a Room-Temperature Ionic Liquid: Persistent Local Environments and the Red-Edge Effect. *Proc. Natl. Acad. Sci.* **2006**, *103*, 831–836.

(199) Hunger, J.; Sonnleitner, T.; Liu, L.; Buchner, R.; Bonn, M.; Bakker, H. J. Hydrogen-Bond Dynamics in a Protic Ionic Liquid: Evidence of Large-Angle Jumps. *J. Phys. Chem. Lett.* **2012**, *3*, 3034–3038.

(200) Canongia Lopes, J. N.; Esperança, J. M. S. S.; Mão de Ferro, A.; Pereiro, A. B.; Plechkova, N. V.; Rebelo, L. P. N.; Seddon, K. R.; Vázquez-Fernández, I. Protonic Ammonium Nitrate Ionic Liquids and Their Mixtures: Insights into Their Thermophysical Behavior. *J. Phys. Chem. B* **2016**, *120*, 2397–2406.

(201) Capelo, S. B.; Méndez-Morales, T.; Carrete, J.; López Lago, E.; Vila, J.; Cabeza, O.; Rodríguez, J. R.; Turmine, M.; Varela, L. M. Effect of Temperature and Cationic Chain Length on the Physical Properties of Ammonium Nitrate-Based Protic Ionic Liquids. *J. Phys. Chem. B* **2012**, *116*, 11302–11312.

(202) Hayes, R.; Imberti, S.; Warr, G. G.; Atkin, R. Amphiphilicity Determines Nanostructure in Protic Ionic Liquids. *Phys. Chem. Chem. Phys.* **2011**, *13*, 3237–3247.

(203) Walden, P. Molecular Weights and Electrical Conductivity of Several Fused Salts. *Bull. Russ. Acad. Sci.* **1914**, 405–422.

(204) Umebayashi, Y.; Chung, W.; Mitsugi, T.; Fukuda, S.; Takeuchi, M.; Fujii, K.; Takamuku, T.; Kanzaki, R.; Ishiguro, S. Liquid Structure and the Ion-Ion Interactions of Ethylammonium Nitrate Ionic Liquid Studied by Large Angle X-Ray Scattering and Molecular Dynamics Simulations. *J. Comput. Chem. Jpn.* **2008**, *7*, 125–134.

(205) Tsuzuki, S.; Shinoda, W.; Saito, H.; Mikami, M.; Tokuda, H.; Watanabe, M. Molecular Dynamics Simulations of Ionic Liquids: Cation and Anion Dependence of Self-Diffusion Coefficients of Ions. *J. Phys. Chem. B* **2009**, *113*, 10641–10649.

(206) Martínez, L.; Andrade, R.; Birgin, E. G.; Martínez, J. M. PACKMOL: A Package for Building Initial Configurations for Molecular Dynamics Simulations. *J. Comput. Chem.* **2009**, *30*, 2157–2164.

(207) Martínez, J. M.; Martínez, L. Packing Optimization for Automated Generation of

Complex System's Initial Configurations for Molecular Dynamics and Docking. *J. Comput. Chem.* **2003**, *24*, 819–825.

(208) Kusalik, P. G.; Svishchev, I. M. Structure in Liquid Water: A Study of Spatial Distribution Functions. *J. Chem. Phys.* **1993**, *99*, 3049.

(209) Sciortino, F.; Geiger, A.; Stanley, H. E. Effect of Defects on Molecular Mobility in Liquid Water. *Nature* **1991**, *354*, 218–221.

(210) Knocks, A. Dielectric Spectroscopy of the Room Temperature Molten Salt Ethylammonium Nitrate. *J. Phys. Chem. A* **2001**, *105*, 8646–8650.

(211) Turton, D. A.; Sonnleitner, T.; Ortner, A.; Walther, M.; Hefter, G.; Seddon, K. R.; Stana, S.; Plechkova, N. V.; Buchner, R.; Wynne, K. Structure and Dynamics in Protic Ionic Liquids: A Combined Optical Kerr-Effect and Dielectric Relaxation Spectroscopy Study. *Faraday Discuss.* **2012**, *154*, 145.

(212) Weingärtner, H.; Krüger, M.; Bründermann, E.; Funkner, S.; Havenith, M. Communications: Polarity Fluctuations of the Protic Ionic Liquid Ethylammonium Nitrate in the Terahertz Regime. *J. Chem. Phys.* **2010**, *132*.